

**EXPERIMENTAL INVESTIGATION OF NITROGEN OXIDE
PRODUCTION IN PREMIXED REACTING JETS IN A VITIATED
CROSSFLOW**

A Dissertation
Presented to
The Academic Faculty

by

Matthew Davis Sirignano

In Partial Fulfillment
of the Requirements for the Degree
Doctor of Philosophy in the
School of Aerospace Engineering

Georgia Institute of Technology
December 2019

COPYRIGHT © 2019 BY MATTHEW D. SIRIGNANO

**EXPERIMENTAL INVESTIGATION OF NITROGEN OXIDE
PRODUCTION IN PREMIXED REACTING JETS IN A VITIATED
CROSSFLOW**

Approved by:

Dr. Timothy C. Lieuwen, Advisor
School of Aerospace Engineering
Georgia Institute of Technology

Dr. Jerry M. Seitzman
School of Aerospace Engineering
Georgia Institute of Technology

Dr. Wenting Sun
School of Aerospace Engineering
Georgia Institute of Technology

Dr. Adam Steinberg
School of Aerospace Engineering
Georgia Institute of Technology

Dr. Ray Laster
Large Gas Turbines Group
Siemens Energy, Inc

Date Approved: August 23, 2019

To the light of my life, shade of my heart, and my guiding star:
my incredible wife Rachel and to our family.

ACKNOWLEDGEMENTS

I would like to start my acknowledgments by recognizing my advisor, Professor Timothy Lieuwen. Without his steadfast support and guidance the work presented in this thesis would not have been possible. I will always be grateful for his understanding and support of my work and my family. I would also like to acknowledge the contributions and guidance of Prof. Jerry Seitzman. His constant involvement in this effort on a weekly basis greatly heightened the quality of the investigation. I would also like to thank my committee members Profs. Adam Steinberg and Wenting Sun as well as Dr. Raymond Laster. I greatly appreciated Prof. Steinberg's eagerness to collaborate and for his patient instruction in all matters related to laser diagnostics. I thank Prof. Sun for lending his expertise in chemical kinetics to this effort, and for Dr. Laster's guidance and support of the work especially during its inception.

In addition to my committee members I would like to acknowledge and thank my colleagues and collaborators at Georgia Tech. Special mention is needed for Vedanth Nair, an intelligent and dependable partner in the investigation of RJICF physics. Without his contributions this work would not have been successful. I would also like to thank my office mate Hanna Ek, whose encouragement was invaluable throughout my PhD studies. I would like to acknowledge the constant guidance and support by Dr. Benjamin Emerson, David Wu, and the rest of the Ben T. Zinn Combustion Lab. I would like to acknowledge the hard work of the undergraduates who assisted with this work, especially Timothy Hardis for his excellent design work on the test section used in this study and Divya Sunkara for her hard work and assistance with data collection. In addition I would like to

acknowledge and thank Ianko Chterev as well my collaborators at Spectral Energies: Dr. Chris Fugger, Dr. Joseph Felver, Dr. Naibo Jiang, Dr. Paul Hsu, Dr. Tony Yi, and Dr. Sukesh Roy. I owe the vast majority of my training and ability with laser diagnostics to these individuals and I am grateful for the opportunity to work with such experts in the field. I would also like to recognize Profs. William Sirignano and Ann Karagozian whose mentorship, advice, and encouragement has shaped my professional life from undergraduate studies at UCLA to the completion of these doctoral studies.

Finally I would like to acknowledge and thank my family. My wife Rachel and our children Tabitha, Abigail, and Anthony have been the safe harbor and source of joy that gave me the endurance and determination to complete this work. My parents David and Rita Sirignano gave me limitless opportunities for which I will be eternally grateful. I am thankful for the support of my sister, Emma, my grandmother, Mary, my Aunt Judith and my entire extended family.

I have the deepest gratitude for all those who have supported me in this endeavor.

This research was partially supported by the University Turbine Systems Research (contract #DE-FE0025344), contract monitor Dr. Mark Freeman.

TABLE OF CONTENTS

ACKNOWLEDGEMENTS	iv
LIST OF TABLES	viii
LIST OF FIGURES	ix
LIST OF SYMBOLS AND ABBREVIATIONS	xiii
SUMMARY	xvii
CHAPTER 1. Background and Motivation	1
1.1 Nitrogen Oxide Production in Gas Turbines	2
1.2 Axial Staging	5
1.3 Reacting Jet in Crossflow	7
1.3.1 Non-reacting Jet in Crossflow Behaviour	8
1.3.2 Flame Stabilization in a Reacting Jet in Crossflow	12
1.3.3 NO _x Production in a Reacting Jet in Crossflow	15
1.4 Research Questions and Thesis Outline	16
CHAPTER 2. Experimental Methodology	19
2.1 Reacting Jet in Crossflow Test Facility	19
2.1.1 Test Facility Configuration for Preliminary Investigation	19
2.1.2 Test Facility Configuration for Primary Emissions Investigation	22
2.1.3 Test Facility Configuration for Primary Pre-flame Mixing Investigation	25
2.2 Design of Experiments	26
2.2.1 Parameter Space for Preliminary Investigation	26
2.2.2 Parameter Space for Primary Investigation	27
2.3 Diagnostics and Measurement Techniques	29
2.3.1 Gas Sampling and Emissions Measurement	29
2.3.2 Flame Chemiluminescence Imaging	30
2.3.3 Laser Doppler Velocimetry	31
2.3.4 Mie Scattering	32
2.4 Image Processing	33
2.4.1 Chemiluminescence Images	33
2.4.2 Mie Scattering Images	36
2.4.3 Flame Edge NO Production Rates	41
2.5 Uncertainty Characterization	43
2.5.1 Uncertainty in Fluid Flow Rates	43
2.5.2 Uncertainty in NO _x Emissions	44
2.5.3 Uncertainty in Particle Tracing of the Flow	44
CHAPTER 3. Nitrogen Oxide Sensitivites of Rich Premixed Reacting Jets with Low Momentum Flux	47
3.1 Liftoff Analysis of Rich Premixed Methane Jets	47

3.2	Emissions of Rich Premixed Methane Jets	49
3.3	Summary of Chapter Findings	53
CHAPTER 4.	Nitrogen Oxide Sensitivites of Premixed Reacting Jets	55
4.1	Lifting Behavior of Premixed Ethane Jets	56
4.2	NOx Emissions Behavior in Premixed Ethane Jets	58
4.2.1	Raw NOx Emissions of Premixed Jets	58
4.2.2	Sensitivity of Emissions to Jet Equivalence Ratio	60
4.2.3	Sensitivity of Emissions to Flame Lift-Off Distance	61
4.2.4	Impact of Exit Velocity Profile on Emissions	66
4.3	Equivalence Ratio of Combustion Considerations	69
4.4	Summary of Chapter Findings	74
CHAPTER 5.	Impact of preflame mixing on equivalence ratio of combustion	77
5.1	Mixture Fraction Fields and Flame Position of Premixed Jets	78
5.2	Pre-flame Mixing Length Scales of Premixed Jets	82
5.3	Comparison of NO Production Rates to NOx Emissions for Premixed Jets	86
5.3.1	Impact of Forced Liftoff on NO Production Rates for Premixed Jets	86
5.3.2	Impact of Exit Velocity Profile on NO Production Rates of Premixed Jets	88
5.3.3	Correlation of NOx Emissions to NO Production Rates for Premixed Jets	90
5.4	Summary of Chapter Findings	92
CHAPTER 6.	Conclusions and recommendations	94
6.1	Summary of Findings	94
6.2	Recommendations for Future Work	97
6.2.1	Investigation of Jet Parameter Impact on Post-Flame Mixing Rates	97
6.2.2	Investigation of Flame Stabilization Physics	98
APPENDIX A.	Supplemental figures	101
A.1	Supplemental Figures for CHAPTER 2	101
A.2	Supplemental Figures for CHAPTER 4	102
REFERENCES		104

LIST OF TABLES

Table 1	– Equipment details for chemiluminescence imaging	31
Table 2	– Interrogation locations for laser Doppler velocimetry of crossflow	32
Table 3	– Symbol legend for CHAPTER 4 figures	55
Table 4	– Symbol legend for CHAPTER 5 figures.	78

LIST OF FIGURES

Figure 1	– Plot of flame temperature and emissions of current gas turbine technologies as well as standard emissions regulations reproduced from Klein [3].	2
Figure 2	– NO as a function of residence time at different flame temperatures. Based on laminar flame calculations at gas turbine conditions reproduced from Lieuwen <i>et al</i> [2].	4
Figure 3	– CO as a function of residence time at different flame temperatures. Based on laminar flame calculations at gas turbine conditions reproduced from Lieuwen <i>et al</i> [2].	5
Figure 4	– Schematic of flow structure of a jet in crossflow reproduced from New <i>et al</i> [18].	9
Figure 5	– Illustration of jet in crossflow shear layer vortex rings being distorted as they advect downstream reproduced from Kelso <i>et al</i> [8].	10
Figure 6	– Illustrations of center-plane section views for fully attached (a), windward lifted / leeward attached (b), lee-stabilized (c), and fully lifted flames (d) in premixed reacting jets in crossflow.	14
Figure 7	– Schematic of experimental as used for preliminary investigation.	20
Figure 8	– Schematic of experimental facility as used in primary investigation.	22
Figure 9	– Schematic of experimental facility as used in pre-flame mixing investigation.	26
Figure 10	– Mie scattering illumination beam path through test section.	33
Figure 11	– Raw (left), binarized (center) flame images, and probability density field of flame position (right) with 0.3 contour corresponding to LO highlighted in red. Images from test case with $\phi_{XF} = 0.60$, $\phi_{Jet} = 1.40$, and $J = 1.56$.	34
Figure 12	– Illustration of flame edge extraction methodology. The solid region denotes the binary flame chemiluminescence, and the solid line denotes the front edge of the flame.	35

Figure 13	– Sequence of mie scattering image processing; shown is raw image (a), sliding minimum subtracted (b), thresholded (c), binarized (d), binned to generate normalized particle illuminated area field (e), and transformed to mixture fraction field (f).	37
Figure 14	– NO production rates as a function of mixture fraction for select jet equivalence ratios.	43
Figure 15	– Characteristic time averaged flame images. Images from test cases with constant crossflow conditions of $\phi_{XF} = 0.6$.	47
Figure 16	– Dependence of lift-off distance at constant exhaust temperature of 1956K upon the jet equivalence ratio. Contours of constant crossflow equivalence ratio (solid) and momentum flux ratio (dotted) are indicated.	49
Figure 17	– Dependence of reacting jet NOx contribution at constant crossflow conditions of $\phi_{XF} = 0.525$ upon the jet equivalence ratio. Contours of constant temperature rise (solid), momentum flux ratio (dotted), and lift-off distance (dashed) are indicated.	50
Figure 18	– Dependence of reacting jet NOx contribution at constant crossflow conditions of $\phi_{XF} = 0.625$ upon the jet equivalence ratio. Contours of constant temperature rise (solid), momentum flux ratio (dotted), and lift-off distance (dashed) are indicated.	51
Figure 19	– Lift-off distance for jets with $J \leq 20$ as a function of reduced equivalence ratio for pipe exit geometry at constant crossflow conditions of $\phi_{XF} = 0.45$ and $\phi_{XF} = 0.50$.	57
Figure 20	– RJICF NOx production as a function of ΔT at constant crossflow conditions of $\phi_{XF} = 0.45$ and $\phi_{XF} = 0.50$.	59
Figure 21	– Normalized NOx production as a function of reduced equivalence ratio for reacting jets with a pipe jet geometry and $J \leq 20$ at constant crossflow conditions of $\phi_{XF} = 0.45$ and $\phi_{XF} = 0.50$.	60
Figure 22	– Normalized NOx production as a function of LO for reacting jets with a pipe jet geometry and $J \leq 20$ at constant crossflow conditions of $\phi_{XF} = 0.45$ and $\phi_{XF} = 0.50$.	62
Figure 23	– Normalized NOx production as a function of reduced equivalence ratio for reacting jets (including high J and methane doped) with a pipe jet geometry at constant crossflow conditions of $\phi_{XF} = 0.45$ and $\phi_{XF} = 0.50$.	64

Figure 24	– Fraction of NO _x production from ethane/methane/air reacting jets compared to ethane/air reacting jets (all with pipe exit geometry) as a function of the associated change in LO . For each point all other test parameters remain constant between the two different compositions.	65
Figure 25	– Mie scattering images of reacting jets in crossflow with a pipe (left) and nozzle (right) exit velocity profiles. Both jets have identical composition, $\phi_{jet} = 4.73$, and $J = 15$.	66
Figure 26	– Fraction of NO _x production from reacting jets with nozzle geometry compared to reacting jets with pipe geometry as a function of the associated change in ϕ_{jet} .	68
Figure 27	– Plot of selected RJICF data using analytical form suggested by Eq. 20.	73
Figure 28	– Sequence of three successive instantaneous mixture fraction fields (left to right) for three reacting jets (top to bottom). The jets have the following parameters: $J = 8$ with nozzle geometry (top), $J = 15$ with nozzle geometry (middle), and $J = 15$ with pipe geometry (bottom). Axis are coordinates normalize by d_j .	79
Figure 29	– Time average mixture fraction fields for three reacting jets. The jets have the following parameters: $J = 15$ with nozzle geometry (left), $J = 8$ with nozzle geometry (middle), and $J = 15$ with pipe geometry (right).	80
Figure 30	– Instantaneous flame position superimposed onto expected mixture fraction fields for a “lean lifted” (left), lee-stabilized (center), and “rich lifted” (right) flame.	81
Figure 31	– Mixture fraction values as a function of distance along jet scalar trajectory for three reacting jets: $J = 15$ with nozzle geometry (blue), $J = 8$ with nozzle geometry (red), and $J = 15$ with pipe geometry (green).	83
Figure 32	– Potential core (left) and decay rate (right) length scales as a function of J for reacting jets with nozzle geometries at constant crossflow conditions of $\phi_{XF} = 0.45$ and $\phi_{XF} = 0.50$.	84
Figure 33	– Pre-flame mixing length scales as a function of J for reacting jets with both nozzle and pipe exit geometries at constant crossflow conditions of $\phi_{XF} = 0.45$ and $\phi_{XF} = 0.50$.	85

Figure 34	- Change in NO _x with change in thermal NO production rates for doped data pairs for reacting jets with nozzle and pipe geometries at constant crossflow conditions of $\phi_{XF} = 0.45$ and $\phi_{XF} = 0.50$.	87
Figure 35	- Fraction of NO _x production from reacting jets with pipe geometry compared to reacting jets with nozzle geometry as a function of the associated percentage change in NO production rate.	89
Figure 36	- Normalized RJICF NO _x production as a function of estimated thermal NO production rates for all nozzle geometry data at constant crossflow conditions of $\phi_{XF} = 0.45$ and $\phi_{XF} = 0.50$.	91
Figure 37	- Velocity profiles for vitiated crossflow with $\phi_{XF} = 0.45$ (left) and $\phi_{XF} = 0.50$ (right). Error bars indicate 99% confidence intervals and data counts for each point are displayed to the right of the error bars.	101
Figure 38	- Lift-off distance for all jets with pipe exit geometry (including $J = 40$ and methane doped) as a function of reduced equivalence ratio at constant crossflow conditions of $\phi_{XF} = 0.45$ and $\phi_{XF} = 0.50$.	102
Figure 39	- Lift-off distance for jets with $J \leq 20$ as a function of reduced equivalence ratio for both pipe and nozzle jet geometries at constant crossflow conditions of $\phi_{XF} = 0.45$ and $\phi_{XF} = 0.50$.	103

LIST OF SYMBOLS AND ABBREVIATIONS

A	Empirical constant for jet trajectory
A_i	Area of investigation
A_{rea}	Area
B	Empirical constant for jet trajectory
C	Local scalar concentration
\bar{C}	Spatial average of scalar concentration
C_m	Centerline scalar concentration
C_o	Reference scalar concentration (from jet potential core)
CVP	Counter-rotating vortex pair
Da_{ign}	Damkohler number based on ignition delay
d_j	Jet diameter
d_p	Particle diameter
DLN	Dry Low NOx
f	Mixture fraction
FSA	Frequency size analyzer
h	Channel height
J	Jet momentum flux ratio
JICF	Jet in crossflow
Ka_{mix}	Karlovitz number based on flow mixture
LDV	Laser Doppler velocimetry
LES	Large eddy simulation
LHV	Lower heating value

$LHV_{C_2H_6}$	Lower heating value of ethane
LHV_{CH_4}	Lower heating value of methane
LO	Lift-off distance
LO_H	Lift-off height
ℓ_{core}	Mixing length scale associated with scalar jet potential core
ℓ_{decay}	Mixing length scale associated with scalar centerline decay post jet core
ℓ_m	Mixing length scale
\dot{m}	Mass flowrate
$\dot{m}_{C_2H_6}$	Mass flowrate of ethane in jet
\dot{m}_{CH_4}	Mass flowrate of methane in jet
\dot{m}_{ef}	Effective mass flowrate of fuel in jet
m_j	Mass of jet fluid
m_{tot}	Total mass
\overline{MW}	Molecular weight of local mixture
MW_j	Molecular weight of jet fluid
MW_{XF}	Molecular weight of crossflow
N_j	Number of moles of jet fluid
N_{tot}	Total number of moles
NOx	Nitrogen oxides
p	Empirical constant for centerline scalar decay
PIV	Particle image velocimetry
PLIF	Planar laser induced fluorescence
PDM	Photodetector module
Re	Reynolds number

Re_p	Particle Reynolds number
RJICF	Reacting jet in crossflow
r	Spatial coordinate
s_c	Distance along scalar concentration centerline
SLV	Shear layer vortices
Stk	Stokes number
Stk _j	Small scale Stokes number
Stk _∞	Large scale Stokes number
T	Temperature
T_{Flame}	Flame temperature
T_j	Jet fluid temperature
T_{XF}	Crossflow temperature
t	Time
t_j	Small jet flow time scale
t_o	Particle response time
$t_∞$	Large jet flow time scale
U	Unmixedness
u_j	Bulk jet velocity
u_p	Velocity of flow relative to seed particle
$u_∞$	Bulk crossflow velocity
x	Streamwise coordinate jet trajectory
z	Height coordinate of jet trajectory
ΔNO_x	Rise in flow NO _x concentration due to jet injection
ΔT	Rise in bulk flow temperature due to jet injection
$\Delta \phi$	Rise in equivalence ratio due to jet injection

Θ	Normalized illuminated area
λ	Wavelength of incident light
μ_g	Dynamic viscosity of gas
ν_g	Kinematic viscosity of gas
ρ_j	Jet density
ρ_p	Particle density
ρ_∞	Crossflow density
τ_{res}	Residence time
$\tau_{pre-flame}$	Time scale for pre-flame mixing duration
ϕ	Equivalence ratio
ϕ_{Flame}	Equivalence ratio of combustion
ϕ_{Global}	System equivalence ratio
ϕ_{jet}	Jet equivalence ratio
ϕ_{XF}	Crossflow equivalence ratio
$[N_2]$	Nitrogen concentration
$[NO]$	Nitric oxide concentration
$[O]$	Atomic oxygen concentration
$[O_2]$	Oxygen concentraion

SUMMARY

This dissertation describes the experimental investigation of nitrogen oxide (NO_x) emissions from a reacting jet in a vitiated crossflow (RJICF). This work is motivated by interest in axial staging of combustion as a means of reducing NO_x emissions from gas turbine combustors operating at high flame temperatures (>1900K). At these temperatures, thermal NO_x production rates are high, and conventional lean-premixed combustor architectures are unable to simultaneously deliver low NO_x and part-load operability. In an axially staged combustor, the majority of the fuel is burned in a conventional lean-premixed flame, but additional fuel is injected from the combustor walls into the vitiated flow further downstream. A RJICF is a natural implementation of this approach. Therefore, a fuller understanding of the governing processes and parameters regarding pollutant formation within this complex flow field is critical to the next generation of gas turbine technology advancement.

From a chemical kinetics standpoint, the three fundamental sensitivities of thermal NO_x production (the dominant mechanism in lean high-temperature flows) are: temperature, time, and oxygen availability. In a RJICF these three parameters are controlled by jet stoichiometry, crossflow temperature and composition, as well as the mixing rates between the fluid streams. Jet/crossflow mixing is critical to the realization of NO_x reduction with axial staging. Within the RJICF, jet/crossflow mixing, occurs both pre- and post-flame. Pre-flame mixing refers to mixing between the reactant jet and the vitiated crossflow prior to combustion, which determines the stoichiometry of burning; it is controlled by degree of flame lift-off (*LO*), and the near-field mixing induced by the

shear layer vortices. The conditions created by the pre-flame mixing region for combustion set the initial conditions for NO_x production of temperature and oxygen availability. Post-flame mixing refers to dilution of the secondary combustion products produced by the reacting jet with the remainder of the crossflow; it is controlled by the counter-rotating vortex pair (CVP). This region of the flow controls the time available for the production of NO_x at elevated temperatures.

It is clear that the NO_x production from a RJICF is a highly coupled process influenced by a myriad of physical parameters. Research in both reacting and non-reacting jets in crossflow (JICF) has pointed towards bulk averaged temperature rise due to the jet injection (ΔT), jet-to-crossflow momentum flux ratio (J), jet stoichiometry (ϕ_{jet}), flame position/stabilization, and crossflow conditions as important factors governing the flow field and/or NO_x production.

The primary purpose of this thesis is to establish the significance of these parameters' influence on RJICF NO_x production. A key challenge was decoupling the interdependent jet parameters in order to observe the dependency of NO_x production on individual parameters. Results are presented that show strong correlations between RJICF NO_x production and ΔT as well as between NO_x and LO . However, these parameters themselves are functions of other fundamental JICF parameters such as J , ϕ_{jet} , and several others. As such, great care was taken in the design of the experimental parameters space and methodology to isolate each parameter and determine the underlying sensitivities of RJICF NO_x production.

NOx emissions data are presented for premixed jets of varying composition, both in terms of fuel selection (methane or ethane or a combination) and equivalence ratio, injected into a vitiated crossflow of lean combustion products. Data were obtained at ΔT values ranging from 75K – 350K, crossflow temperatures from 1350K – 1810K, J values from 2 – 40, ϕ_{jet} from 0.8 – 9.0, and two jet geometries. In addition, several data series were replicated with varied ethane/methane ratios at constant ϕ_{jet} to influence flame lifting independent of other parameters. Similarly, the jet geometry was varied to influence shear layer vortex growth rates and, hence, pre-flame mixing rates.

Overall, these data indicate that NOx emissions are largely determined by the temperature rise induced by the reacting jet (ΔT). However, significant variation in NOx emissions was observed at constant ΔT . The data is consistent with the idea that this variation in NOx is controlled by the stoichiometry at which combustion actually occurs, referred to as ϕ_{Flame} . ϕ_{Flame} is influenced by ϕ_{jet} and pre-flame mixing of the jet and crossflow that, in turn, is a function of LO , jet exit geometry, and crossflow temperature. While this result is expected, it manifests itself in complex manners. For example, NOx levels were observed to be nearly independent of ϕ_{jet} for a range of conditions, due to the coupled dependence of ϕ_{jet} and LO . Similarly, NOx emissions are shown to vary significantly based on jet exit geometry. The reduction in NOx emissions associated with the nozzle jet geometry relative to the fully developed exit flow reached values of over 50%.

The significance of ϕ_{Flame} in relation to RJICF NOx production was tested by comparing NOx emissions levels to time averaged pre-flame mixing levels, in the form of mixture fraction. Images of Mie scattering from ceramic particles seeded in the jet were

utilized to assess pre-flame mixing, and were compared to high speed chemiluminescence images of the flame. These results confirmed ϕ_{Flame} as a 1st order governing parameter on RJICF NO_x production. For example, the data clearly shows negligible NO_x production at very lean flame stoichiometries induced by high levels of pre-flame mixing, as well as NO_x increasing to high levels as flame stoichiometry trended toward unity. However, the data also shows that pre-flame mixing levels alone are insufficient to describe the 3x variation in NO_x within the high NO_x region. Sensitivity of NO_x to post-flame dilution rates, intermittency in flame stoichiometry, variable fuel consumption rates along flame edge, and inherent limitations of the measurement technique could all cause this variation.

The presented work reveals that the key to ensuring minimal NO_x production for a given ΔT is to promote flame liftoff and enhance shear layer vortex growth rates. Flame liftoff is a complex multi-faceted problem whose governing physics are not directly addressed in this work. Similarly, the controlling sensitivities of the post-flame mixing efficacy, via strength and structure of the CVP, are most likely diverse in nature and are not addressed herein. Both of these areas require further work to deepen understanding of the relevant phenomena.

CHAPTER 1. BACKGROUND AND MOTIVATION

The generation of electricity from the consumption of natural gas is a major world energy source, accounting for 35% of electricity in the US for 2018 [1]. The plurality of natural gas as an energy source is projected to continue to grow as it supplants petroleum and coal due to environmental and economic concerns. The vast majority of the energy produced by natural gas fired systems is from gas turbines, either as standalone combustion turbines or in tandem with a steam turbines as part of combined-cycle power plants. Due to the critical position they possess in the world energy market, it is critical to continue to stimulate the development of these systems in order to increase their efficiency and mitigate their environmental impact.

Over the past several decades, the gas turbine industry has experienced significant increases in combined cycle efficiency, while simultaneously reducing undesirable emissions such as nitrogen oxides (NO_x). Improvements in turbine materials and cooling methods have enabled ever higher turbine inlet temperatures. Higher turbine inlet temperatures lead to higher work/thrust in simple cycle systems and higher thermal efficiencies in combined cycle systems. In parallel, advances in fuel injector and post-flame mixing technologies have reduced NO_x emissions through the elimination of locally high-temperature regions of the lean, premixed combustion. These advances have led to the current state of the art in gas turbine Dry Low NO_x (DLN) combustor architectures [2]. In order to achieve further improvements in combined cycle efficiency, however, higher turbine inlet temperatures are required. Figure 1 plots the flame temperature and NO emissions of several historical classes of gas turbines as well as several regulatory standards with regards to NO_x

emissions. Figure 1 clearly indicates that DLN combustors will be unable to meet current emission regulations while simultaneously delivering the necessary elevated combustor exit temperatures required for further increases in cycle efficiency due to the nature of NO production.

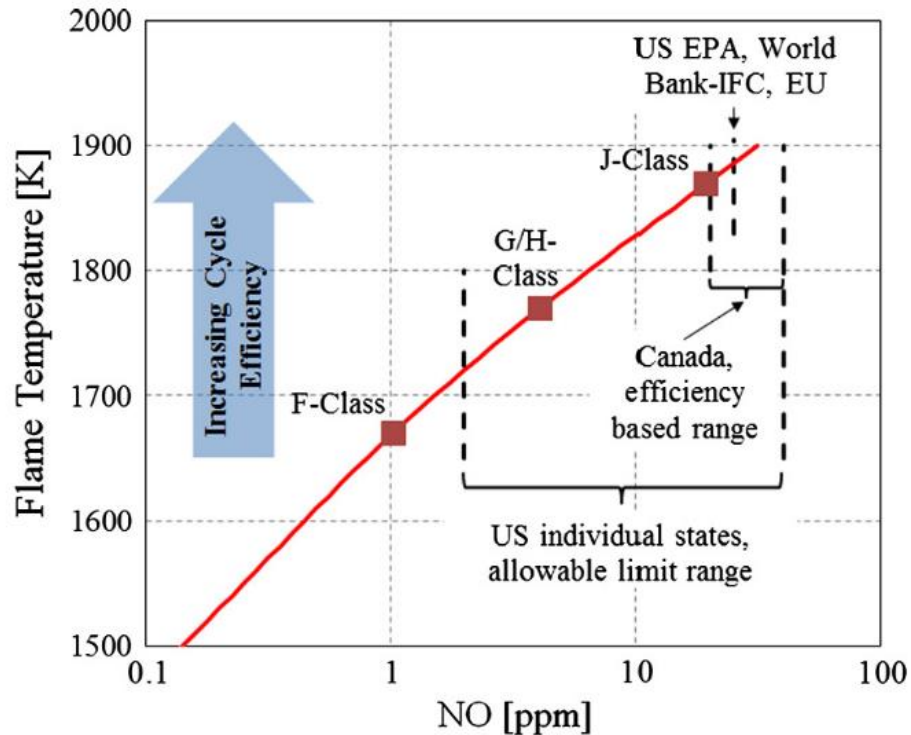


Figure 1 – Plot of flame temperature and emissions of current gas turbine technologies as well as standard emissions regulations reproduced from Klein [3].

1.1 Nitrogen Oxide Production in Gas Turbines

The historical approach of reducing NO_x emissions from gas turbines by focusing on rapid fuel/air mixing works best in cases where the perfectly mixed flame temperature of the combustor is below the threshold where NO_x production rates become significant. A general rule of thumb in the gas turbine industry is to restrict flame temperatures to below

1800K (already exceeded in state-of-the-art gas turbines). This is due to the kinetic sensitivities of the major pathways from NO_x formation in a DLN gas turbine combustor.

NO_x is produced by a number of mechanisms both within the flame (referred to as prompt NO) as well as post-flame [4]. At flame conditions proposed for future gas turbines (lean, temperature > 1975 K), thermal NO formation is the dominant source of NO_x [5]. In premixed laminar flames at similar conditions, thermal NO is shown to become the majority source for NO_x with as little as 5 ms of residence time (τ_{res}) [2, 6]. Thermal NO formation occurs via the Zeldovich NO mechanism in post-flame regions of the combustor. The Zeldovich mechanism is relatively simple, contained in its entirety by Equations 1 – 3, and well understood, with the rate constants well characterized over a wide range of conditions [7].



The rate of NO production from the Zeldovich mechanism is linear with both τ_{res} and atomic oxygen concentration, [O], as well as an exponential function of temperature (T) as indicated by Equation 4 derived from Bowman [6] and illustrated by Figure 2. Figure 2 plots calculated NO levels as a function τ_{res} at gas turbine conditions and various flame temperatures. Visible in Figure 2 is the prompt contribution to NO as well as the thermal contribution. At flame temperature as low as 1900K, prompt NO is shown to be rapidly exceeded by thermal NO; reinforcing the dominance of thermal NO at relevant conditions.

$$[NO] \propto [O][N_2]e^{-38,379/T}\tau_{res} \quad (4)$$

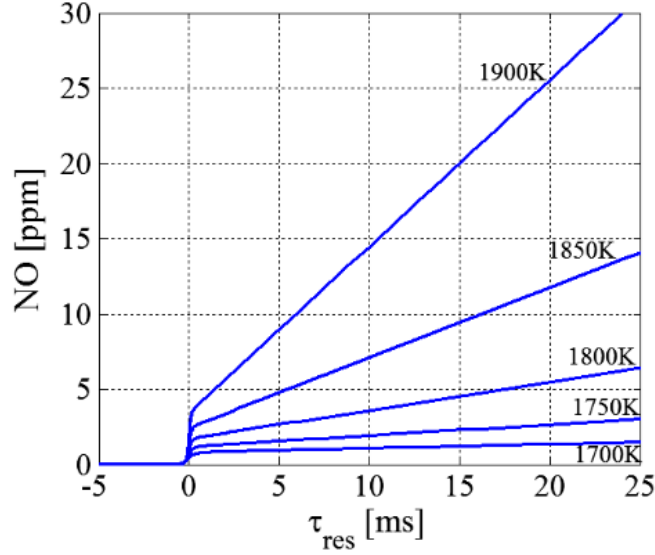


Figure 2 – NO as a function of residence time at different flame temperatures. Based on laminar flame calculations at gas turbine conditions reproduced from Lieuwen *et al* [2].

These sensitivities of thermal NO formation have significant consequences on potential approaches for gas turbine combustor emissions mitigation. The linear dependence on τ_{res} immediately suggests that combustors designed with reduced τ_{res} would be successful in reducing NOx. There is, however, a limit to the extent this strategy can be used. It is limited, in practice, by operability needs with regards to turndown. Gas turbine combustors, in the field, need to operate over a range of loads each of which is associated with a different flame temperature. Lower loads, with lower flame temperatures, require longer residence times to enable complete conversion of super-equilibrium CO into CO₂. The dependency of CO on τ_{res} and flame temperature is highlighted in Figure 3, which plots calculated CO levels as a function τ_{res} at gas turbine conditions and various flame temperatures. Therefore, τ_{res} , is generally set by the requirement to achieve low CO emissions at some specified load

point. As such, and alternate method to NO_x reduction that preserves part load operability is needed.

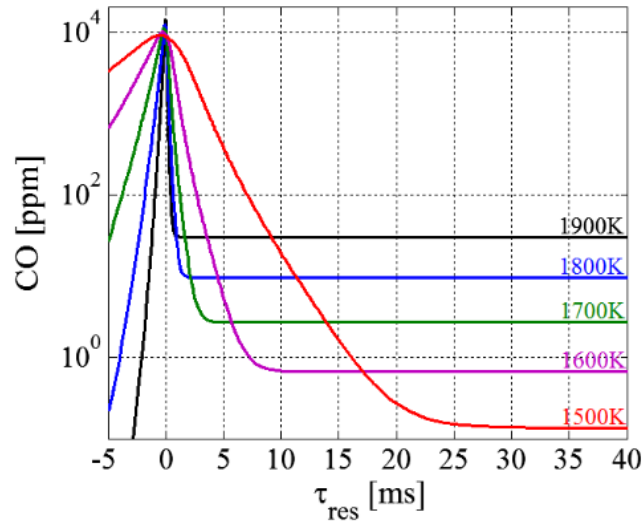


Figure 3 – CO as a function of residence time at different flame temperatures. Based on laminar flame calculations at gas turbine conditions reproduced from Lieuwen *et al* [2].

1.2 Axial Staging

Axial staging has been proposed as a NO_x mitigation approach that can address the highlighted thermal NO sensitivities while also allowing for successful operation of the gas turbine at part load [8-10]. Axial staging is accomplished by combusting the majority of the fuel in a manner similar to traditional DLN architectures, i.e. lean and premixed. Subsequent to the primary combustion zone, the remainder of the fuel is injected into the flow in the vicinity of the combustor exit. This downstream injection creates a secondary region of combustion that raises the combustor temperature to its final value. The primary advantage of this approach is that it drastically reduces τ_{res} for the final, high-temperature, portion of the flow, and thereby minimizes the time available for elevated NO production

rates. In addition, axial staging also address the [O] dependence of NO formation by placing the secondary combustion region in a reduced oxygen environment, in the form of the high-temperature combustion products of the primary combustion zone. Combustion in such an environment has been demonstrated to significantly reduce NO production [11]. Finally, axial staging also enables load turndown without negative impact on CO emissions as the combustor can simply be operated without the secondary injection when required.

The theoretical benefits of axial staging are substantial, and the extent to which it can reduce NO_x emissions while preserving turndown potential has been demonstrated by Goh *et al* [12], who utilized a chemical reactor network model in conjunction with a design optimization framework to assess the minimum theoretical NO_x level achievable (under infinite mixing-rate assumptions) in a high-pressure staged combustor subject to CO emissions constraints and turndown considerations. With these restrictions, achievable NO_x levels were calculated to be less than 2 ppm with a flame temperature of 1975K, which corresponds to less than 5% of the NO_x level produced by an ideal DLN architecture.

Due to this potential, axial staging concepts have become a focus of research [13, 14]. This collective work supports the potential benefit of axial staging, but has also stressed how critical the rapid and thorough mixing of the primary combustion products and the secondary fuel injection prior to ignition is to the realization of the NO_x benefit. If mixing rates are not sufficiently high, an axially staged combustor could emit significantly higher NO_x levels than predicted, and in the worst cases, at levels higher than those of DLN architectures.

1.3 Reacting Jet in Crossflow

A reacting jet in a vitiated crossflow (RJICF) presents a natural means by which to implement axial staging as its utilization does not require the insertion of hardware into the high-temperature crossflow. RJICFs are present in other applications such as in Rich-Quench-Lean combustors [15] and various fuel injection systems. The numerous industrial applications paired with the complex coupling of interesting physics have made the RJICF and the non-reacting jet in crossflow (JICF) topics of extensive research.

As mentioned in Section 1.2, the mixing between the crossflow and the axially staged fuel is crucial to achieving reductions in NO_x emissions. Within the context of a RJICF, the relevant mixing can be divided into two regions: pre-flame and post-flame mixing. Pre-flame mixing refers to the mixing of the secondary jet and the crossflow prior to combustion. Since the composition of the jet and crossflow are not equal, pre-flame mixing controls whether reaction occurs in a premixed or non-premixed mode; in the former case, it also determines the stoichiometry of burning. Post-flame mixing refers to mixing of the secondary combustion products with the vitiated crossflow generated by the primary flame. Post-flame mixing determines the time history of the temperature of the final combustion products, controlling the extent to which elevated flow temperatures, in comparison to the combustor exit temperature, persist.

The reacting flowfield that dictates the mixing behavior of these regions is complex and incorporates flame propagation of inhomogeneous mixtures in highly strained flows, edge flame propagation, flame auto-ignition, and hydrodynamic stability effects. As a pathway to understanding the NO_x production of such a complex reacting flow it is

necessary to understand the mechanics of flame stabilization as well as the underlying behavior of the non-reacting flowfield. To set this context, the following sections of this chapter discuss RJICF dynamics in more detail.

1.3.1 *Non-reacting Jet in Crossflow Behaviour*

Due to numerous industrial applications and its importance as a canonical fluid mechanics problem, the JICF has been the subject of extensive research [16]. As a result, the fundamental form of time averaged velocity and scalar fields for subsonic, non-reacting, momentum driven JICF is well established [16], and has been shown to be primarily governed by the jet-to-crossflow momentum flux ratio given by:

$$J = \frac{\rho_j u_j^2}{\rho_\infty u_\infty^2} \quad (5)$$

with ρ and u denoting the density and velocity of the jet and crossflow with subscripts j and ∞ respectively. A common resultant jet trajectory correlation is given by:

$$\frac{z}{d_j \sqrt{J}} = A \left(\frac{x}{d_j \sqrt{J}} \right)^B \quad (6)$$

with x and z corresponding to the trajectory location in the direction of the crossflow and transverse to it, respectively. The jet diameter is denoted by d_j and the coefficients A and B are parameters that account for various effects, such as boundary layer thickness, jet exit velocity profile, and jet trajectory definition (i.e., maximum velocity, scalar concentration, or other important fluid-mechanic features).

The mixing of the jet fluid with the surrounding crossflow is determined by the dynamics of a complex topology of vortical structures [17]. The dominant coherent vortical structures are the horseshoe vortex system, the wake vortices, the shear layer vortices (both leading-edge and lee-side), and the counter-rotating vortex pair. The topology of a JICF with these coherent vortical structures indicated is shown by Figure 4.

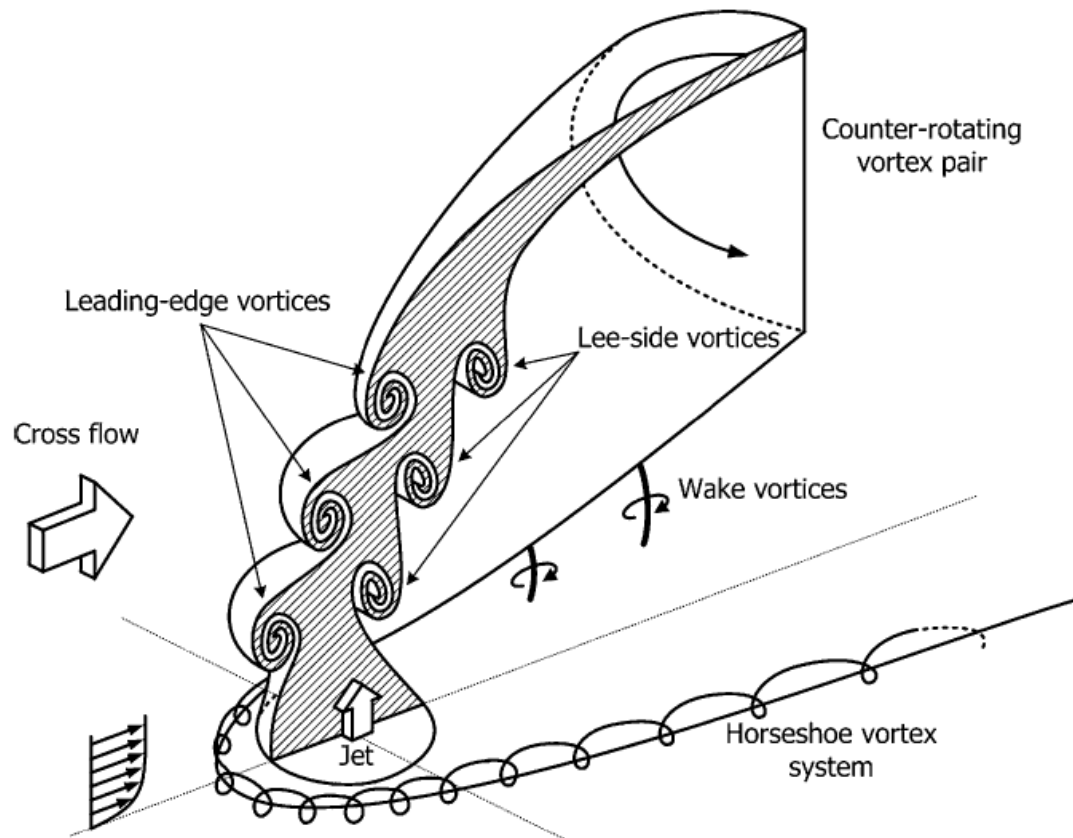


Figure 4 – Schematic of flow structure of a jet in crossflow reproduced from New *et al* [18].

The two coherent structures of particular interest to the pre-flame and post-flame mixing of a RJICF are the shear layer vortices (SLVs) and the counter rotating vortex pair (CVP). The SLVs are generated by the unstable shear layer of the exiting jet. The instability is via the Kelvin-Helmholtz mechanism, and creates rolled up regions of concentrated

vorticity. The growth rate and size of these structures have an important influence on near-field mixing of the jet fluid and the crossflow. In addition, the SLVs are distorted by interaction with the crossflow and each other. This distortion of the SLVs results, on a time averaged basis, in the CVP as described by Kelso *et al* [8] and illustrated in Figure 5. The CVP itself is a critical aspect of JICF topology as it is responsible for the far-field mixing behavior.

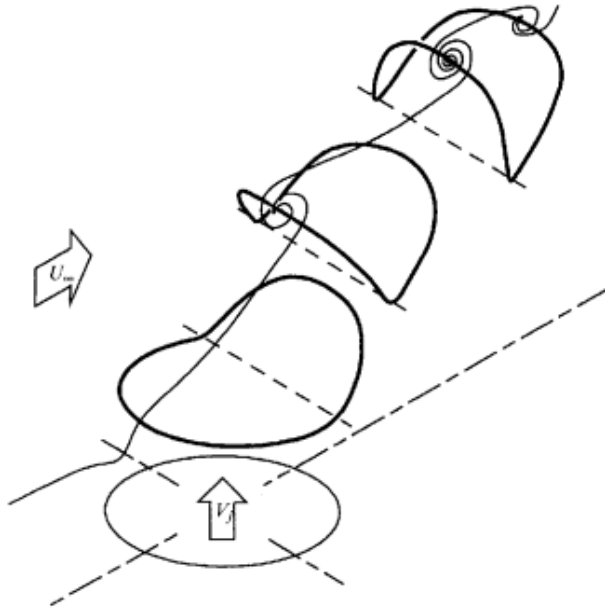


Figure 5 – Illustration of jet in crossflow shear layer vortex rings being distorted as they advect downstream reproduced from Kelso *et al* [8].

Extensive research has been aimed at characterizing JICF mixing, and it has been observed to be divided into near-field and far-field behavior, with the transition between the two being termed the ‘branch’ point. Smith & Mungal [19] observed the near-field behavior to be more ‘jet-like,’ with centerline maximum mean concentration (C_m/C_o) decay scaling as shown in Equation 7:

$$\frac{C_m}{C_o} \propto s_c^{-p} \quad (7)$$

with s_c corresponding to distance along the jet centerline trajectory, and p ranging from values of 1 to above 1.3 dependent on J and exit velocity profile [19-21]. The far-field was observed to be more ‘wake-like’ with C_m/C_o again scaling as in Equation 7 but with p values between 1 and $2/3$ [19, 20].

Another useful parameter for characterizing the mixing behavior of JICF is the unmixedness (U), defined by Equation 8:

$$U = \frac{1}{A_i} \iint_{A_i} \frac{(C/C_o - \bar{C}/C_o)^2}{(\bar{C}/C_o)(1 - \bar{C}/C_o)} dA_{rea} \quad (8)$$

with A_i corresponding to the area of investigation, and C/C_o and \bar{C}/C_o to the normalized local value and spatial average of jet fluid concentration respectively. Unmixedness can be applied to both cross-sectional and center-plane data to assess the degree of mixing of the JICF at a point along its trajectory, and Karagozian *et al* [20] observed both applications to follow similar trends. In addition, it was observed that cross-sectional and center-plane unmixedness follow similar trends to centerline maximum concentration decay. Both Smith & Mungal [19] and Karagozian *et al* [20] notice that, in certain instances, much more rapid decay of jet fluid concentration compared to other jets can be experienced, and this can be visualized by a ‘crossing’ of decay lines.

The rates at which JICF mixing occurs are dependent on the exit velocity profile of the jet [20]. This in turn can be tied back to the growth rates of the SLVs. New *et al* [22] observed, via flow visualization of JICF, that the growth rates of SLVs in jets with a top-

hat (minimal boundary layer) exit velocity profile are much greater than those found in jets with a parabolic (fully-developed boundary layer) exit velocity profile.

1.3.2 *Flame Stabilization in a Reacting Jet in Crossflow*

A second critical piece of the physical context as relates to RJICF NO_x production is the influence of combustion on the JICF, and in turn, the coupled influence of the flowfield on flame stabilization. The manner, and consequently the location, of flame stabilization is particularly important with regards to pre-flame mixing in the RJICF. This is commonly referred to as the manner of attachment and the degree of flame lifting. Broadly speaking, RJICF flames can be characterized as attached or lifted depending upon the flame leading edge being located at the jet exit or at some point downstream. In literature, two distinct attachment locations are often referred to; namely the windward (upstream) and leeward (downstream) sides of the jet exit. Steinberg *et al* [23], who investigated heated H₂/N₂ jets injected into a heated air crossflow, observed the leeward branch oscillated less in location than the windward branch due to the presence of a low speed region generated by the recirculation zone behind the jet. The more transiently located windward branch was observed to stabilize over a wide range of locations, from near the jet exit to the flame tip. In premixed ethylene/air jets injected into vitiated crossflow, Wagner *et al* [24-26] also observed the two flame branches, with the windward branch again more unsteady in its stabilization location. The windward branch exhibited full attachment, windward liftoff with unsteady location of stabilization, and full windward branch blowoff. This final conditions is referred to herein as lee-stabilization. Schmitt *et al* [27] observed fully attached behavior in premixed natural gas/air jets injected into vitiated crossflow. For equivalence ratios above 0.77, the flame was observed to originate inside

the injector tube due to the deposition of hot crossflow fluid upstream of the jet exit by the horseshoe vortex system located at the interface of the windward edge of the jet and the crossflow boundary layer.

The point of flame stabilization in lifted flames, whether a windward branch or the entire flame, is termed the ‘flamebase’ and is akin to an edge flame in some ways. Hasselbrink & Mungal [28] as well as Han & Mungal [29] investigated flame behavior of lifted RJICF flames of non-premixed methane jets injected into crossflowing air at ambient conditions. The flamebase exhibited premixed flame behavior and experienced strong flow/flame interaction, while the flame downstream was more diffusion based in nature with significantly less flow interaction. In the work presented by Steinberg *et al* [23] discussed earlier in this section, the windward branch flamebase exhibited premixed or tribrachial flame behavior, and its location was shown to be dependent on regions of high extensive principal strain-rate. Large Eddy Simulations (LES) conducted by Schulz & Noiray [30] of jets with parameters matching those investigated by Wagner *et al* [24-26] manifested the transient windward branch behavior, and described the transient windward branch stabilization location as a retreating edge flame that is intermittently “brought back” by auto-ignition. Figure 6 contains representative illustrations of the various flame attachment configurations discussed in this section.

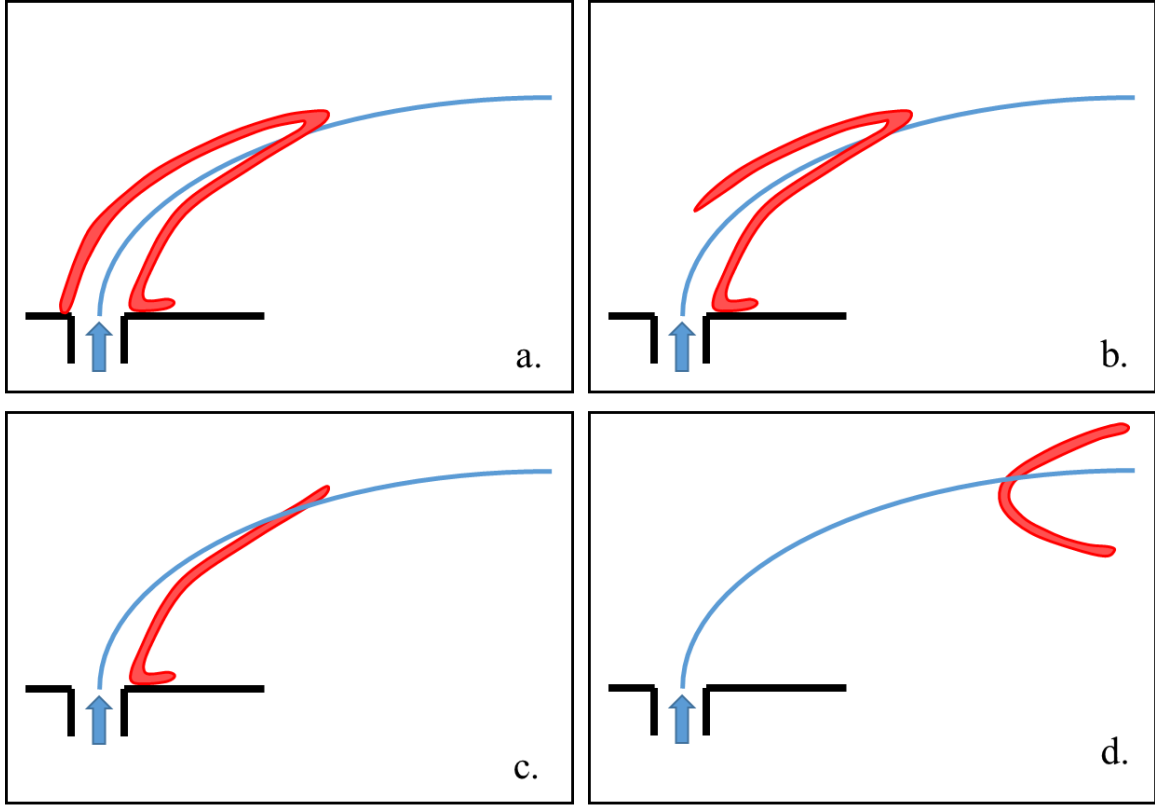


Figure 6 – Illustrations of center-plane section views for fully attached (a), windward lifted / leeward attached (b), lee-stabilized (c), and fully lifted flames (d) in premixed reacting jets in crossflow.

Attempts have been made to model the degree of lifting. Sullivan *et al* [31] showed that the flow times associated with the flame lift-off height of non-premixed jets of various compositions injected into high-pressure and -temperature vitiated crossflow correlated well to calculated auto-ignition times. Gautam [32] asserted, based on liftoff height in jets injected into quiescent air, that flamebase stabilization was propagation based and governed by turbulent flame speed. Kolb *et al* [33] correlated the lift-off height (LO_H) of lean premixed natural gas/air jets in high-temperature vitiated crossflow by incorporating both auto-ignition and turbulent flame speed considerations. The resultant correlation, Equation 9, indicates the ratio of a mixture Karlovitz number (Ka_{mix}) that represents the

flame speed contribution and an ignition delay Damkohler number (Da_{ign}) as the governing parameter in determining liftoff.

$$LO_H = 9.7 \left(Ka_{mix} / Da_{ign} \right)^{0.61} \quad (9)$$

The importance of liftoff in regards to pre-flame mixing is not strictly due to providing a temporal/spatial opportunity for the jet fluid and crossflow to mix. Nair *et al* [34] observed, via simultaneous stereographic high-speed particle image velocimetry (stereo-PIV) measurements and hydroxyl radical imaging with planar laser induced fluorescence (OH-PLIF), that the presence of the flame in the vicinity of the jet exit suppressed the growth rate of the SLVs in non-premixed jets composed of hydrogen and diluents injected into a vitiated crossflow. The suppression of these vortices would negatively impact the near-field mixing of a RJICF and impact the CVP structure. However, Nair *et al* [35] did confirm the presence of the CVP in a non-premixed methane RJICF using simultaneous tomographic PIV (tomo-PIV) and OH-PLIF.

1.3.3 *NO_x Production in a Reacting Jet in Crossflow*

Little work has been done to investigate how observed flame behavior impacts the NO_x production of these reacting jets. Bandaru and Turns [36] investigated NO_x emissions from a reacting jet in a crossflow of air over a range of jet compositions and crossflow velocities and observed a lack of sensitivity of the NO_x levels to these parameters, with the exception of fuels noted for high soot formation such as ethylene. The heat loss to the soot particles causes a reduction in product temperature and thus a noticeable decrease in thermal NO formation. Lyle *et al* [37] investigated the impact of partial premixing in jet flame emissions by injecting rich premixed methane/air jets with a co-flow of air into

quiescent air. No significant deviation from NO_x emissions produced by fully non-premixed jet flames was seen for jet equivalence ratios (ϕ_{jet}) greater than 5.0. For $5.0 \geq \phi_{jet} \geq 1.5$ reduced NO_x production was observed compared to the non-premixed case, with a maximum reduction of 25% at $\phi_{jet} \approx 1.5$. For values of ϕ_{jet} even closer to the stoichiometric condition a significant increase in NO_x emissions was observed. This trend is supported by equivalence ratio's impact on flame temperature and in turn by thermal NO_x production's exponential sensitivity to temperature as discussed in Section 1.3.3. It follows that the jets Lyle *et al* [37] observed evolved from high-temperature diffusion flames, to low-temperature rich premixed flames, and on to high-temperature near-stoichiometric premixed flames. Prathap *et al* [38] showed that, for a given bulk temperature rise of the flow due to the RJICF flame (ΔT), jet trajectory exhibited strong sensitivity to jet parameters such as momentum flux ratio and Reynolds number, but NO_x production experienced little variation. Roa *et al* [39] demonstrated that NO_x production from a RJICF was a strong function of ΔT . These results demonstrate that NO_x production by a RJICF is primarily driven by the associated ΔT , but did not explore NO sensitivities to parameters such as jet fuel/air ratio or J for a given ΔT . Ahrens *et al* [40] observed a strong correlation between NO_x production and local mixture fraction for lean premixed RJICF, indicating the degree of mixing between the jet and the crossflow prior to combustion as a critical element to NO_x reduction.

1.4 Research Questions and Thesis Outline

In summary, work to date has clearly demonstrated that ΔT or, restated, the jet fuel mass flow rate is a controlling parameters of NO_x emissions from a RJICF. However, there still remains the open question as to the most efficient way to deliver ΔT from a NO_x

perspective and if any other parameters can impact NO_x production to a similar magnitude. A better understanding of the dominant sensitivities of NO_x production in a RJICF and the governing phenomena is key to addressing current energy challenges. The work presented in this document seeks to assist in building this understanding by pursuing the following central research questions:

1. At constant values of ΔT , what is the impact on RJICF NO_x production of:
 - JICF parameters such as J and exit velocity profile?
 - Chemical parameters such as jet composition and stoichiometry as well as crossflow temperature?
 - Flame behavior such as flame lifting and the related lift-off distance?
2. Are any of these impacts on the same order as ΔT ?
3. What are the governing physics that are being impacted by these parameters to induce the influence on NO_x?

The remainder of this thesis presents the methods that were used to address these core research questions and the results of those investigations.

Chapter 2 describes the experimental facility that was developed to investigate premixed fuel/air jets injected into high-temperature vitiated crossflow of lean combustion products. The design of experiments is also presented, laying out the methodology for answering the aforementioned research questions as well as the test conditions and parameter space. Chapter 2 also details the diagnostic techniques used to collect data, the processing methods used to analyze it, and an assessment of the related uncertainty.

Chapter 3 describes the results of preliminary work conducted with rich premixed methane/air jets. This work was conducted over a wide range of crossflow temperatures and ΔT values. The NOx measurements are compared to the associated values of J , ϕ_{jet} , and lift-off distance (LO) for each jet. Chapter 3 seeks to address the scale of impact on NOx emissions by test parameters in relation to ΔT , and to highlight parameters of interest for further investigation.

Chapter 4 describes the results of the main body of NOx emissions measurements conducted on premixed ethane/air jets. This work is conducted over a wide range of J and ϕ_{jet} values and includes both fully developed pipe and top-hat nozzle jet exit velocity profiles. Data is presented where LO is varied independently from other parameters by doping the jet fuel with methane. The focus of the analysis presented in Chapter 4 is on the dependence of RJICF NOx emissions on ϕ_{jet} , LO , and exit velocity profile. Chapter 4 introduces the equivalence ratio of combustion (ϕ_{Flame}) as a governing NOx parameter and a function of ϕ_{jet} , LO , and mixing rate governed by exit velocity profile.

Chapter 5 presents time averaged pre-flame jet/crossflow mixing data, in the form of seeded jet mie scattering, of the same parameter space presented in Chapter 4. Chapter 5 focuses on more directly assessing ϕ_{Flame} values (via local mixture fractions) and its impact on NO production rates and correlating them to the measured NOx emissions.

Chapter 6 concludes this thesis with a summary of key findings and a discussion of recommendations for future work in this avenue of scientific investigation.

CHAPTER 2. EXPERIMENTAL METHODOLOGY

This chapter describes the experimental facility, the design of experiments, as well as the diagnostic methodology and equipment employed in the experimental investigation reported in this thesis.

2.1 Reacting Jet in Crossflow Test Facility

The experimental facility was designed to provide lean, high temperature products of natural gas/air combustion in order to auto-ignite premixed jets of methane and air at atmospheric pressure. The facility was heavily modified from that used by Wilde in his investigation of reacting jet dynamics [41]. The facility was used in multiple configurations over the course of the investigation described in this thesis. Each configuration is described separately in the subsequent sections.

2.1.1 *Test Facility Configuration for Preliminary Investigation*

The primary components of the facility include the main burner, flow conditioning section, test section with secondary injection, and chemical quench section. A schematic of the facility as it was used to investigate the parameter space described in Section 2.2.1 is provided by Figure 7.

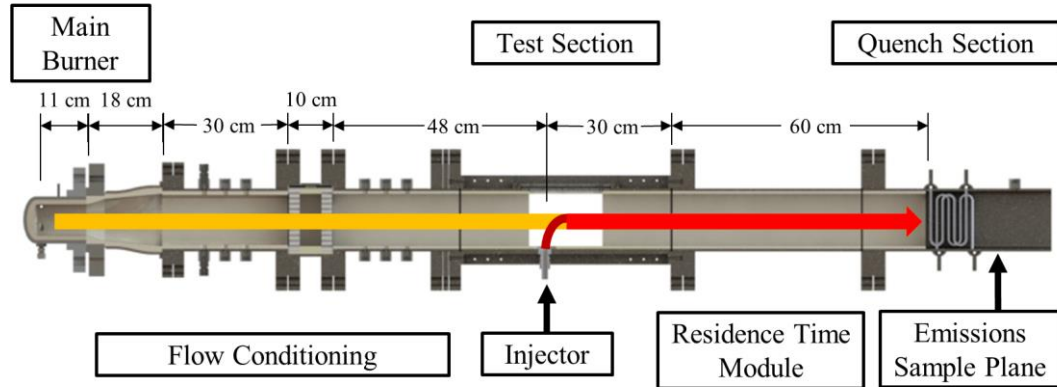


Figure 7 – Schematic of experimental as used for preliminary investigation.

A premixed natural gas/air mixture, preheated to 591K (± 5 K) to enable stable operation at lean equivalence ratios of approximately 0.5, is combusted in the main burner. The reactants are metered with sub-critical orifices and injected tangentially into a 76 mm diameter circular section via four ports with exit diameters of 11 mm. The main burner stoichiometry was adjusted in order to vary the approach flow temperature to the RJICF and demonstrated stable operation across the entire range of test conditions. The vitiated flow then passes through a flow conditioning section, which consists of a 18 cm long circular to rectangular cross-section transition piece followed by a 30 cm (3.7 channel hydraulic diameters) settling chamber, two ceramic honeycomb flow straighteners (separated by 10cm), and a second 30 cm settling chamber in sequence. The honeycomb flow straighteners are 25 mm thick Mullite Versagrid units comprised of 6.35 mm by 6.35 mm passages. The test section includes optical access (sides and top) and the secondary injection jet. The test section cross-section is 63.5 mm wide by 114 mm tall. This cross-section initiates immediately after the second flow straightener 48 cm upstream of the jet exit plane. The jet is injected via a 12 mm inner diameter stainless steel tube flush with the ceramic lining of the test section floor. The jet delivered preheated and premixed

methane/air mixtures metered using critical orifices. Jet preheat temperatures ranged from 420 – 460K, enabling autoignition of the jet in the vitiated crossflow. The injection tube is straight for 40 diameters prior to the jet exit to ensure fully developed exit flow profile [42], and mixing of the fuel and air flows occurring approximately 100 diameters prior to the jet exit. The jet Reynolds number ranged from 3900 – 7000, and the jet mass flow averaged less than 5% of total mass flow, with a maximum of 6.5%.

The facility delivered a vitiated crossflow of natural gas/air combustion products at equivalence ratios ranging from 0.50 to 0.65 at a fixed average velocity of 17.3 m/s, calculated from the measured temperature and mass flow rate. Corresponding test section temperatures ranged from 1650 – 1810K and cross flow Reynolds numbers from 4375 - 4800 based on a hydraulic diameter of 8.16 cm. The test section temperature was estimated via spectroscopic measurement of the irradiance of a ceramic shielded type R thermocouple installed in place of the jet 3 cm above the jet exit.

After the remaining 30 cm of the test section post-injection and a 45 cm long residence time module, the hot gases enter the NO_x measurement section. Because of the highly non-uniform NO_x and flow velocity profiles (which implies that simply mapping out spatial NO_x values is insufficient, as NO_x fluxes can also vary spatially), the flow is cooled to freeze NO_x formation, then mixed, then measured. This quench section consists of a 15 cm ceramic lined entrance section followed by 15cm of pressurized water filled radiator tube banks. The tube banks are made up of two sets of six tubes shaped as indicated in Figure 7 and set opposite each other. Each of the two banks is fed by a manifold that is itself supplied at the sides and top. The waste water is expelled into a similar manifold. The quench section was verified to reduce the gas flow temperature to less than 700K. A

reference τ_{res} post jet injection can be calculated using a reference velocity and the 90 cm distance between the jet exit centerline and quench radiator banks. In designing the test matrix, two possible reference velocities were considered: the average velocity of the crossflow (~ 17.3 m/s), or one based upon the main and jet mass flow rates and the average gas temperature after combustion of the RJICF. The former was used, which leads to a reference τ_{res} of 51 – 53 ms for all tests reported here. The components and methodology used for NO_x sampling and measurement are described in more detail in Section 2.3.1.

2.1.2 Test Facility Configuration for Primary Emissions Investigation

A schematic of the facility as used to investigate the emissions of the parameter space described in Section 2.2.2 is provided by Figure 8. The experimental facility consists of a main burner to generate a high-temperature cross flow, a flow conditioning section, an optically accessible RJICF section, a residence time module, a quench section, and an emissions sampling system.

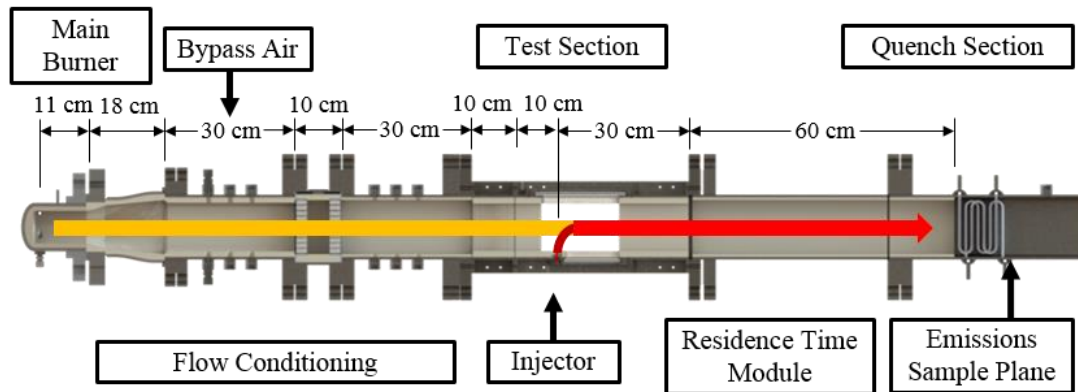


Figure 8 – Schematic of experimental facility as used in primary investigation.

As noted, the primary components of the facility were described previously in Section 2.1.1 and therefore attention will be given to any modifications made to the facility

described in Section 2.1.1. The swirling main burner was stably operated at either an equivalence ratio of 0.5 or 0.55. The combined uncertainty and temporal variation in this equivalence ratio was less than 3%. This main burner was supplied with preheated reactants at 590K (± 5 K). The crossflow then passes through the flow conditioning section as described in Section 2.1.1 to remove the swirl and produce a more uniform crossflow for the secondary injection. In the configuration presented in Figure 8, bypass air was injected into the crossflow as part of the flow conditioning section. The intent of this modification was to provide the means to seed the crossflow with ceramic particles for velocimetry if necessary. After dilution, the effective equivalence ratio of the vitiated crossflow (ϕ_{XF}) is equal to 0.45 or 0.5, with an uncertainty (including temporal variation) of less than 3%. These two crossflow conditions provided two distinct crossflow temperatures of 1350K and 1410K, in order to assess the impact of crossflow temperature on *LO* and NO_x emissions. The temperatures were calculated as follows. A bulk flow density was calculated from metered flow rates and measured bulk flow velocity of the crossflow within the test section (measurement method described subsequently in this section and detailed in Section 2.3.3). This bulk flow density was compared to results from an adiabatic flame calculation to determine the relationship of the bulk crossflow temperature relative to adiabatic flame temperature. The associated Reynolds numbers for each of these two crossflow conditions, based on a hydraulic diameter of 5.70 cm, are 6270 and 6750.

The test section itself is the most significant change to the facility from previous studies. It incorporates a transition section equipped with a contoured (fifth order

polynomial curves) ceramic lining to reduce the channel width from 63.5 mm to 38 mm¹. The reduced width results in a test section cross section of 38 mm x 114 mm and an average flow velocity of 25.8 m/s. The crossflow velocity through the test section was characterized using Laser Doppler Velocimetry (LDV). The system and its implementation is discussed in more detail in Section 2.3.3, and plots of the resulting measurements can be found in Appendix A.1. The test section also incorporates four sided optical access (side and top/bottom) as well as the secondary injection jet.

Two different jet configurations were used in order to explore the limiting cases of fully developed and top-hat jet exit velocity profiles. As will be seen, these two velocity profiles have quite different shear layer growth rates and NO_x emissions. The first configuration utilizes a 6mm inner diameter stainless steel tube set flush with the ceramic lining of the test section floor. The tube is straight for 80 diameters prior to the jet exit, sufficient to achieve a fully developed turbulent profile [42]. The second geometry utilizes a contoured ceramic nozzle with a 24 mm and 6 mm entrance and exit diameter respectively; i.e., a factor of 16 area reduction. This significantly reduces the boundary layer thickness at the jet exit. A significant body of work [20, 43-45] utilizing nozzles with similar area reduction and shaped with the same fifth order polynomial have characterized the momentum thickness of the configuration (assessed at a height of $0.1d_j$ above the jet exit) to be between $0.05d_j$ and $0.1d_j$ [46] for the J values investigated here.

In both cases, the jet fluid was premixed and consisted of preheated ethane/air or ethane/methane/air mixtures. The fuel and air are mixed approximately 200 diameters prior

¹ This width reduction is responsible for the change in hydraulic diameter compared to that reported in Section 2.1.1.

to the point of injection to ensure fully premixed jet fluid. The preheat temperature of the jet fluid ranged from 460 – 500K. The Reynolds number of the jet, based on jet diameter, ranged from 6.60×10^3 – 18.3×10^3 . The mass flow of jet never exceeded 8% of the total mass flow, averaging about 5%. The mass flows of all constituent species were metered using critical orifices.

After injection of the jet into the crossflow, the exhaust flow path is identical to that described in Section 2.1.1; no changes were made through the remainder of the test section, followed by the “residence time module”, and finally through the “quench section” (detailed in Section 2.1.1).

2.1.3 Test Facility Configuration for Primary Pre-flame Mixing Investigation

In order to conduct Mie scattering imaging of the pre-flame mixing as described in Section 2.3.4, the facility was further modified from the configuration presented in Section 2.1.2. A schematic of the facility as used in the Mie scattering investigation for the primary parameter space presented in Section 2.2.2 is shown in Figure 9.

The facility was operated identically as described in Section 2.1.2, with the exception of the removal of the quench section and NO_x measurement system. This was done so as to not contaminate this hardware and instrumentation with seed particles. After injection of the jet into the crossflow, the exhaust gases flow through the remainder of the test section as well as the residence time module. Following this section, the flow is vented to the laboratory exhaust system.

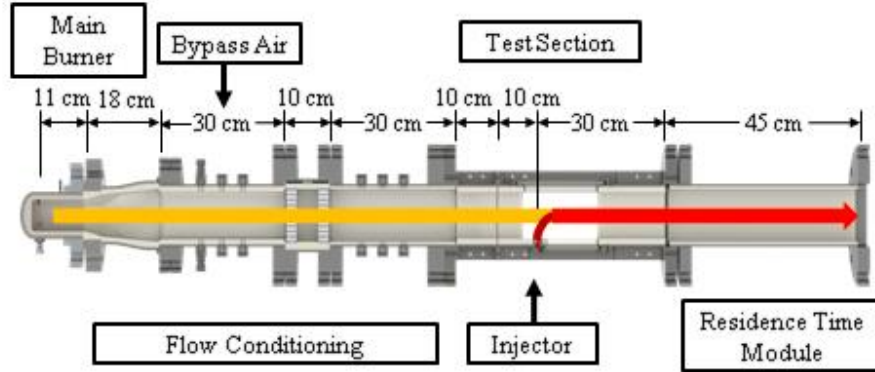


Figure 9 – Schematic of experimental facility as used in pre-flame mixing investigation.

2.2 Design of Experiments

This section describes the design of experiments and the test matrices utilized in conjunction with the various facility configurations described in Section 2.1. The pairings of test matrix and facility configuration are Section 2.2.1 with Section 2.1.1 and Section 2.2.2 with Section 2.1.2 as well as Section 2.1.3.

2.2.1 *Parameter Space for Preliminary Investigation*

The test matrix for the preliminary investigation was designed to look at the NO_x sensitivity to different fractions of heat release in the axial stage versus the main burner. It was also developed to investigate the differences in NO_x between achieving a given ΔT across the axial stage with jets of differing J and equivalence ratio in order to provide some insight into the most beneficial manner, from an emissions standpoint, in providing premixed fuel in an axial staged combustor. The rest of this section describes the test matrix development approach.

The equivalence ratio of the main burner was varied to create values of $\phi_{XF} = 0.5 - 0.65$ in increments of 0.025. The crossflow velocity was held nearly constant ($u_{\infty} = 17.1 - 17.7$ m/s) between all cases by reducing the mass flow rate with increasing equivalence ratio to account for higher flow temperatures, which allowed ϕ_{XF} to independently control crossflow temperature; the approach-flow temperature has significant effects on flame lift-off height, as described later. For each crossflow condition a range of final system equivalence ratios (ϕ_{Global}) were targeted. The test section temperature data was utilized to ensure that several of the ϕ_{Global} values resulted in equal exhaust temperatures across crossflow conditions.

Once the crossflow conditions were fixed and the target system equivalence ratio was chosen, the jet conditions were then iterated by changing J and the jet equivalence ratio (ϕ_{jet}). The target J ratios were chosen in the range of 2 to 5 to ensure that the jet stays within the confines of the viewable region of the test section. The associated value of ϕ_{jet} for each test point was derived based on ϕ_{Global} , ϕ_{XF} , and J constraints. This created an interdependent relationship between J and ϕ_{jet} , with ϕ_{jet} being driven down as J increases.

2.2.2 *Parameter Space for Primary Investigation*

The aim of the test matrix for this work was to include jets over a broad range of J and ϕ_{jet} values, at discrete levels of ΔT , and varying exit velocity profiles and crossflow temperatures. The test point selection methodology was as follows.

The test matrix targeted four intervals of ΔT : 75K, 150K, 225K, and 350K. Each of these ΔT values were obtained for six J values of 6, 8, 10, 15, 20, and 40. This J range sweeps the transition from globally to convectively unstable in nonreacting JICF [16]. This

matrix of 24 points was repeated at two crossflow conditions, where ϕ_{XF} is set to 0.45 or 0.5 respectively. The crossflow velocity was held nearly constant at 25.8 m/s ($\pm 3.5\%$) across both crossflow conditions by adjusting the mass flow to account for the different crossflow temperatures. Thus, the two crossflow conditions create two vitiated flows of equal velocity but differing temperature. Utilizing the measured crossflow conditions and adiabatic flame temperatures for the secondary combustion zone, a target final system equivalence ratio (ϕ_{Global}) was calculated for each ΔT . With ϕ_{XF} , ϕ_{Global} , and J now fixed, the necessary ϕ_{jet} value for each data point was calculated. This method, again, creates an interdependency on J and ϕ_{jet} , with ϕ_{jet} decreasing as J is increased for a given selection of ΔT and ϕ_{XF} . The entirety of the matrix was repeated for each of the two jet exit velocity profiles. The parameter space associated with these ethane-fueled tests consisted of 6 (J) x 4 (ΔT) x 2 (ϕ_{XF}) x 2 (jet velocity profiles) = 96 points.

Additional data points were taken to decouple LO from stoichiometry and J values, with mixtures of ethane and methane. Methane addition increases autoignition delays compared to ethane and was observed to increase LO values for these crossflow test conditions. Reactor modeling conducted with CHEMKIN indicated that mixing in methane into the jet fuel stream could increase autoignition delay with only a change in adiabatic flame temperature on the order of 20K or less. The resulting methane composition of these points ranged from 40 – 55% of the jet fuel mass. Again, each combination of ΔT and J for these replicated points was conducted at each crossflow condition and jet exit velocity profile. Two ΔT values were selected thereby adding an additional 48 test points to the matrix, bring the total interrogated conditions to 144.

2.3 Diagnostics and Measurement Techniques

2.3.1 Gas Sampling and Emissions Measurement

Emissions sampling was conducted using a slotted probe located 12.5 mm after the section of radiator tube banks. The slotted probe intakes gas through a 1.6 mm wide and 120 mm tall slot in order to simultaneously sample the entire vertical span. The spatial variation of NO was mapped out in a 4 by 3 grid with single point measurements taken at the center of each 30 mm wide by 35 mm tall box for a several jet configurations similar to those in the test matrix. The spatial variation of NO measurements in the direction transverse to the slotted probe was less than 1 ppm (corresponding to less than 15% of average for each vertical position). Gas collected by the probe is funneled into a 7.75 inner diameter tube which connects the probe to the gas analyzer. Gas samples were analyzed by a Horiba PG-350 gas analyzer which uses a cross-flow modulation chemiluminescence detection method to measure NO_x (NO and NO₂ in this instance) at a rate of 1 Hz. After a steady state was achieved for each reacting jet condition, emissions data was collected for two to three minutes.² All reported NO_x data is based on an average of the collected data for each test condition.

The total NO_x produced by the test rig is a function of that produced by the vitiated crossflow and the reacting jet. In order to assess the NO_x production of the jet, baseline NO_x levels were obtained. These measurements were obtained by emissions sampling of the crossflow conditions without any mass flow from the secondary injector. Consequently,

² Results from test matrix described in Section 2.2.1 used two minute average and results from test matrix described in Section 2.2.2 used three minute average.

the reacting jet NO_x contribution (Δ NO_x), calculated by subtracting the baseline NO_x from the test point NO_x level, serves as a measure for the complete impact of the jet on the NO_x level.

2.3.2 *Flame Chemiluminescence Imaging*

Images of flame chemiluminescence emissions were obtained from side-on imaging using an intensified high speed camera at either 2000 or 5000 frames per second (fps) dependent upon the test campaign. To capture CH* chemiluminescence (with contributions from CO₂*), a combination of a single-band bandpass filter and a long wave pass filter were used. The Semrock BrightLine bandpass filter had a center wavelength of 434 nm with a bandwidth of 17 nm and the Semrock EdgeBasic long wave pass filter had an edge wavelength of 364 nm.³ CH* is a commonly used heat release marker for hydrocarbon flames [24-26, 31]. For comparison with the CH* images, comparable high speed OH* chemiluminescence was simultaneously obtained for certain cases through a single-band bandpass filter with a center wavelength of 320 nm and a bandwidth of 40 nm. The equipment and acquisition rate details for each measurement campaign are presented in Table 1.

³ The bandpass filter had significant transmission levels in near infrared spectrum. This prompted the use of the long wave pass filter due to its reduced transmission profile in the near infrared.

Table 1 – Equipment details for chemiluminescence imaging

Test Matrix	Species / Subset	Camera	Intensifier	fps
Section 2.2.1	CH* / All	Photron Fastcam SA-1	Lambert HiCATT	2000
Section 2.2.2	CH* / Pipe Geometry: Emissions	Photron Fastcam SA-1	LaVision IRO	5000
Section 2.2.2	CH* / Pipe Geometry: Mie Scattering	Photron Fastcam SA-1	LaVision IRO	5000
Section 2.2.2	OH* / Nozzle Geometry: Emissions	Photron Fastcam SA-1	Lambert HiCATT	5000
Section 2.2.2	CH* / Nozzle Geometry: Emissions	Photron Fastcam SA-Z	Lambert HiCATT	5000
Section 2.2.2	CH* / Nozzle Geometry: Mie Scattering	Photron Fastcam SA-Z	Lambert HiCATT	5000

2.3.3 Laser Doppler Velocimetry

As mentioned in Section 2.1.2, the crossflow velocity through the test section was measured using LDV. The system consists of an Innova 90C-6 Argon Ion laser system to generate a multiline beam with a wavelength range from 457.9 to 514.5 nm. This multi-wavelength beam then passes through a Bragg cell operating at 40 MHz to create two beams, with the second frequency shifted compared to the first. A pair of prisms is used to separate two pairs of beams (with each pair including a frequency shifted component). The wavelength of the pairs were nominally 488nm and 514.5nm. The beam pairs are then coupled to optical fibers connected to a transceiver unit. The transceiver unit contains a lens with a focal length of 363mm to create a 3.74 μ m fringe spacing. Aluminum oxide (Al₂O₃) particles with a nominal diameter of 5 μ m were injected via the bypass air circuit into both the top and bottom of the flow conditioning channel in order to seed the crossflow.

The flow velocity was measured at six discrete intervals above the center of the jet exit at heights ranging from 6 – 50 % of the test section height. The location of each interrogation point is given in Table 2. The scattered light from the seeded flow is collected by the transceiver and focused onto a photomultiplier. A photodetector module (PDM) then reads the transduced light signal and controls the gain for the measurement to be analyzed by the frequency size analyzer (FSA) digital signal processor. The processed signal is passed through an 80 MHz low pass filter, after which it is downmixed by a specified frequency, and then finally passed through a bandpass to remove outlying frequencies and noise.

Table 2 – Interrogation locations for laser Doppler velocimetry of crossflow

Interrogation Point	Height (mm)	Normalized Height
1	7	0.06
2	12	0.105
3	17	0.15
4	27	0.23
5	37	0.32
6	57	0.5

2.3.4 *Mie Scattering*

The jet was seeded with 0.3 – 1 micron TiO_2 particles that were used for Mie scattering imaging. As discussed Section 2.4.2, the spatial density of these particles was used to assess local mixture fraction and to quantify pre-flame mixing levels. A frequency doubled ND:YLF laser was used to produce a 5 kHz pulse train of 527 nm pulses in order to illuminate the particles. The beam was formed into a sheet 63.5 mm wide and 2 mm

thick. The laser sheet was passed through the test section from above (shown in Figure 10), entering through the top window and impinging upon the test section floor, with a portion of it exiting through the bottom window. The center of the beam width was aligned with the center plane of the test section floor. The resultant field of interrogation was 60 mm x 60 mm, initiating 1 mm upstream of the jet exit.

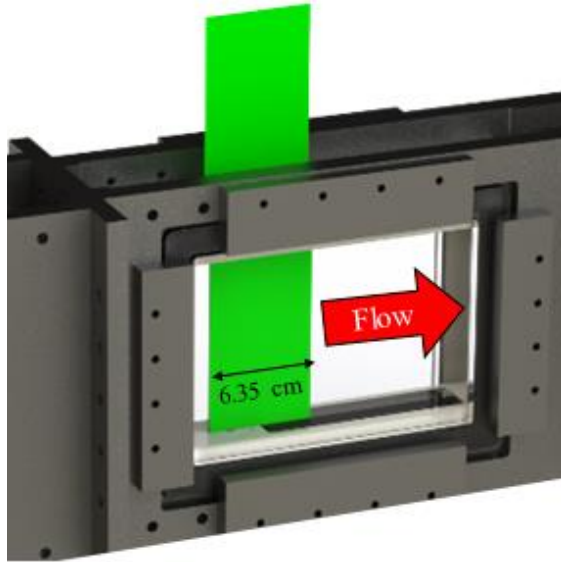


Figure 10 – Mie scattering illumination beam path through test section.

The illuminated particles were imaged with a high speed camera at 5000 fps, using bandpass filter with a center wavelength of 527 nm and a bandwidth of 20 nm

2.4 Image Processing

2.4.1 Chemiluminescence Images

The instantaneous and time averaged chemiluminescence images were analyzed to determine the spatial flame structure. Of particular interest was the degree of flame lifting, which strongly influences pre-flame mixing. Flame structure was assessed via analysis of

a time averaged flame probability density map developed from the instantaneous chemiluminescence images. The processes for creating the flame probability map is described here.

The raw images were normalized and filtered using a guided image filter [47] to remove most of the noise. An example instantaneous raw image for a given case is shown on the left of Figure 11. The filtered image is then binarized by using a threshold based on Otsu's method [48] (which does not require an arbitrary threshold), see center pane of Figure 11. The binarized instantaneous images were then averaged to create a probability field of the flame existing at that location, an example of which is shown in the right panel of Figure 11. The flame probability maps from the testing described in Section 2.2.1 were built from 909 images for each test condition, and the flame maps from the testing described in Section 2.2.2 were built from 2500 images.

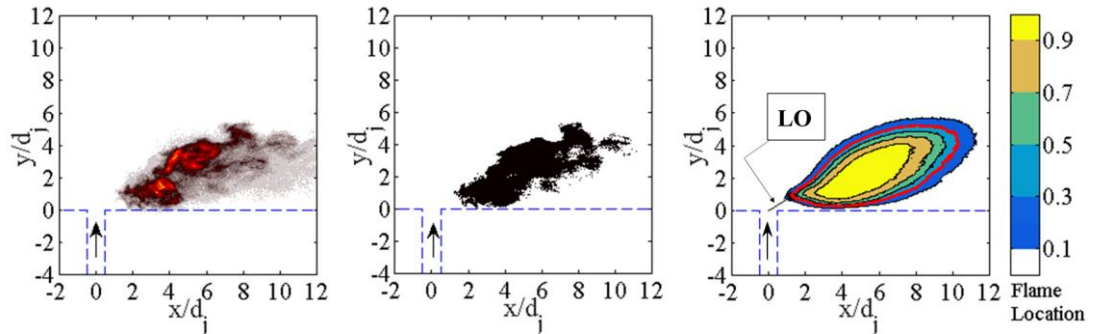


Figure 11 – Raw (left), binarized (center) flame images, and probability density field of flame position (right) with 0.3 contour corresponding to LO highlighted in red. Images from test case with $\phi_{XF} = 0.60$, $\phi_{Jet} = 1.40$, and $J = 1.56$.

LO was defined as the minimum distance between the center of the jet exit and the 0.3 contour (highlighted in red in right pane of Figure 11) of the flame probability map.

The CH^* results were used for the purpose of this analysis. No significant difference was observed for LO values obtained from CH^* and OH^* .

For the portion of the work associated with pre-flame mixing rates presented in CHAPTER 5, the position of the leading edge of the flame image was of particular interest; it was used to approximate the mixture fraction at the flame. The leading edge was extracted at each instant by identifying a boundary around the line of sight flame image. The maximum and minimum vertical position were identified and the front edge of the boundary between the top and bottom points was extracted as the flame leading edge. Figure 12 shows a sample binary flame image with top and bottom points identified and flame edge extracted.

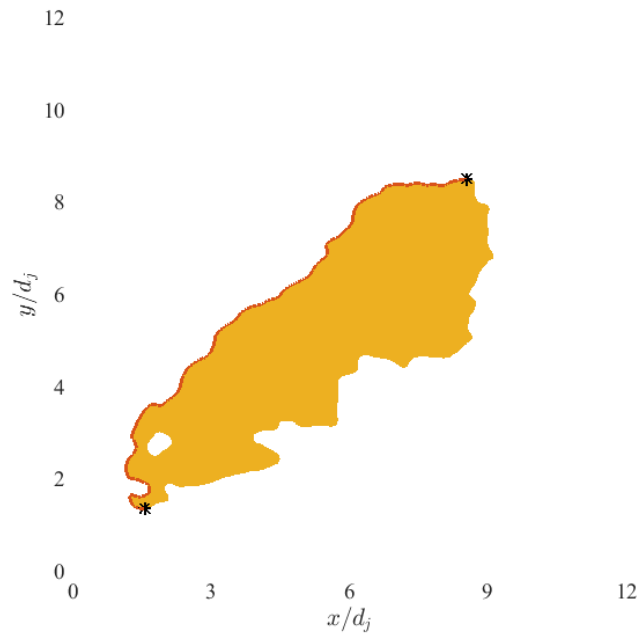


Figure 12 – Illustration of flame edge extraction methodology. The solid region denotes the binary flame chemiluminescence, and the solid line denotes the front edge of the flame.

2.4.2 *Mie Scattering Images*

The Mie scattering images were background subtracted with a 15 image sliding minimum to remove reflections from the test section floor and side windows. The image was then thresholded using a technique similar to the chemiluminescence images (Section 2.4.1) to remove contributions from out of focus/plane particles and trace amounts of other luminosity. The resultant image was binarized and passed through a 9x9 box filter. This reduces the field's spatial resolution but assigns a value proportional to the area (in pixels) that is illuminated inside the binned region, i.e. the illuminated area. Another consequence of using the box filter is the discretization of the measurement into 81 intervals. The illuminated area values are then normalized in reference to the jet core, immediately at the jet exit, where the mixture fraction is known; this normalized illuminated area value is defined as Θ . Figure 13 shows a sample Mie scattering image through this process.

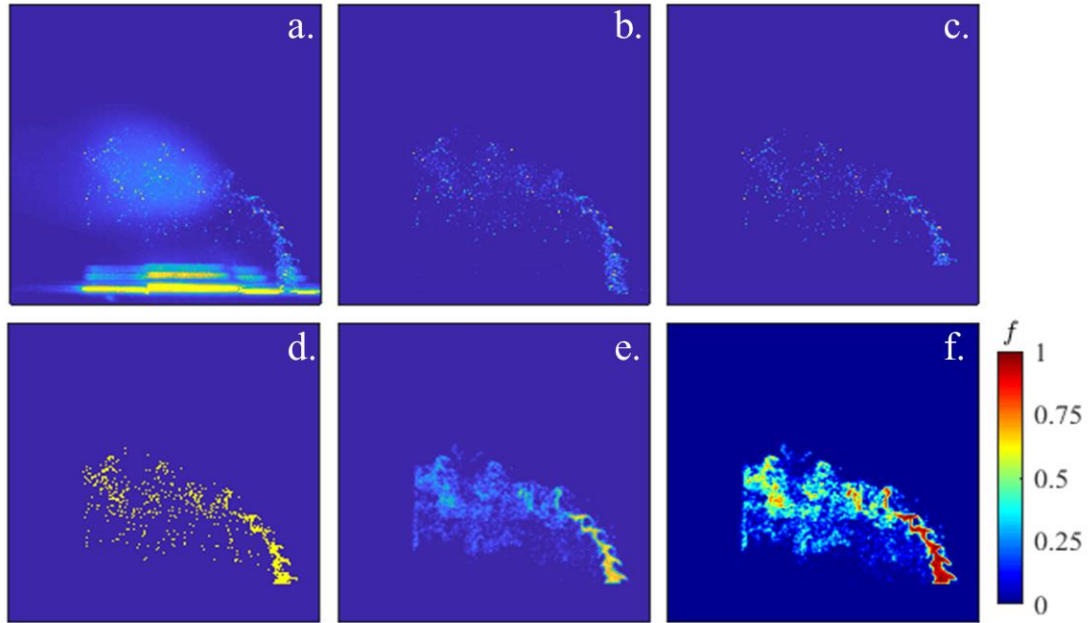


Figure 13 – Sequence of mie scattering image processing; shown is raw image (a), sliding minimum subtracted (b), thresholded (c), binarized (d), binned to generate normalized particle illuminated area field (e), and transformed to mixture fraction field (f).

The next step of the process is the conversion of the normalized illuminated area (Θ), shown in Figure 13e, to mixture fraction, shown in Figure 13f. Similar efforts to derive mixture fraction or other scalar concentrations from Mie scattering has been conducted previously [49, 50] and validated against the well understood behavior of a free jet. The approach described next is similar to Sautet & Stepowski [50], but generalizes their work to account for temperature differences between the fluid streams. Its key assumptions are that (i) particles follow the flow, and (ii) mixing of sensible enthalpy and mass occurs at the same rate. This procedure and these assumptions are discussed next.

First, the relationship between Θ and the seed particle number density will be discussed. Depending upon the scale comparison of the wavelength of incident light (λ) to

the diameter of the seed particle (d_p), the scattered light intensity varies from being proportional to the volume of the seed in the Rayleigh limit ($d_p/\lambda \ll 1$), or proportional to the cross-sectional area of the particle when $d_p/\lambda \gg 1$. In the case of the presented data, where 0.3 – 1 μm diameter particles and 532 nm incident light make $d_p/\lambda \approx 1$, the intensity of light is proportional to the Rayleigh cross-section, which accounts for the refractive properties of the material. It is critical to note that due to particles being identified in a binary fashion (Figure 13d), the data presented do not have a dependence on the intensity of the scattered light. The exception to this statement is the threshold level. Due to variations in seed particle size, laser sheet intensity, and shot-to-shot intensity, the threshold value does not represent a constant value of Θ across all images and test points. This impacts the lowest values of f that are identified in each image. However, low values of f are associated with low flame temperatures in these experiments. As discussed in Section 1.1, thermal NO production is exponentially dependent on temperature. Therefore, thermal NO production is insensitive to small changes in temperature, when that temperature is below a certain critical value. As the f values that are impacted by the varying threshold are associated with flame temperatures below this critical value, this effect is neglected.

The impact of variation in light intensity was minimized by using binary images to determine Θ , as discussed above. However, the size of each particle (in pixels) is of critical importance. For most optical applications, the size of an image is proportional to the size of the object through a magnification factor. However, below a certain limit the object size has no correlation on the image size. This is defined as diffraction limited. Using Equations 2.7 and 2.8 from Raffel *et al.* [51] it is clear that in the data reported here, the images size

is governed by the diffraction limited minimum image diameter. The implications of this is that the illuminated area discussed above is proportional to the number of particles in each 9x9 bin and not their projected areas. By extension it follows that Θ is therefore proportional to the local particle number density normalized by the jet core value.

It is important to note an additional source of uncertainty associated with this methodology. As described, the method for determining the mixture fraction is dependent on the diffraction limited nature of the imaging. This opens the possibility for multiple small particles in close proximity to appear identical to a single particle on the image. This effect will have the most impact on identification of the core region. If the core region is inaccurately identified the entire mixture fraction field is biased towards higher values of f . Depending on the magnitude of this bias it could have significant consequences such as indicating a flame is burning fuel rich when in fact it is fuel lean but near stoichiometric. These two conditions have significantly different thermal NO production rates due to [O]. It is critical, therefore, to compare the potential core lengths acquired from this method with literature to gain insight into the magnitude of any bias and the validity of the measurement.

The method for transforming Θ into f is now addressed. This section has established that, subject to several assumptions, Θ is proportional to seed number density. This number density can be impacted (prior to the flame) by two mechanisms: mass exchange and thermal expansion. Due to the temperature disparity between the jet and the crossflow, mixing of the jet with the crossflow will reduce Θ by both mechanisms, and their impact must be accounted for simultaneously. Therefore the following expression relates the local values of Θ to these mechanisms:

$$\Theta = \frac{T_j}{T} \frac{N_j}{N_{tot}} \quad (10)$$

where T is the local temperature, T_j is the temperature of the jet core, and N_j/N_{tot} is the local mole fraction of jet fluid. N_j/N_{tot} relates to the mixture fraction as:

$$f = \frac{m_j}{m_{tot}} = \frac{MW_j}{\overline{MW}} \frac{N_j}{N_{tot}} \xrightarrow{\text{yields}} \frac{N_j}{N_{tot}} = \frac{\overline{MW}}{MW_j} f \quad (11)$$

where m_j/m_{tot} is the local mass fraction of jet fluid, MW_j is the jet fluid molecular weight and \overline{MW} is the mixture molecular weight. Substituting Equation 11 into Equation 10 yields the following relation between f and Θ :

$$\Theta = \frac{T_j}{T} \frac{\overline{MW}}{MW_j} f \xrightarrow{\text{yields}} f = \frac{T}{T_j} \frac{MW_j}{\overline{MW}} \Theta \quad (12)$$

The local temperature (based on an assumption of uniform specific heat) and molecular weight are themselves functions of f given by Equations 13 and 14:

$$T = fT_j + (1 - f)T_{XF} \quad (13)$$

$$\overline{MW} = fMW_j + (1 - f)MW_{XF} \quad (14)$$

where T_{XF} and MW_{XF} are the temperature and molecular weight of the crossflow. Combining Equations 12 – 14 gives a quadratic formula in terms of the measured fluid properties and Θ which can be solved for f :

$$\left(1 + \frac{MW_{XF}}{MW_j}\right) f^2 + \left[\frac{MW_{XF}}{MW_j} + \Theta \left(\frac{T_{XF}}{T_j} - 1\right)\right] f - \frac{T_{XF}}{T_j} \Theta = 0 \quad (15)$$

The presented method is invalid in the near vicinity of the flame as another source of temperature increase/sensible enthalpy addition is present. The mixture fraction of the flame is thereby assessed by using an expected value that is compiled from instances when the flame is not present in this location. A time-averaged mixture fraction field is compiled from 2500 images for each data point. Only data that is at least 12 pixels (≈ 1 mm) upstream of the flame in each instantaneous mixture fraction field contributes to the average. This interval insures that no 9x9 bin in which the flame is present contributes to the time average. In addition, if the flame position is dependent on mixture fraction, then the used expected value does not capture this cross-correlation. Consequently, the flame is, in essence, being characterized by the mixture fraction of the flow preceding it. This is done out of necessity as, once again, this methodology is invalid at the flame. This effect reinforces the necessity of comparison between the pre-flame flow fields and JICF literature in order to establish confidence in the data.

2.4.3 *Flame Edge NO Production Rates*

The time averaged mixture fraction fields are in turn used to calculate NO production rates that are meant to simultaneously capture the multiple impacts that varying ϕ_{Flame} would have on NOx production; i.e. via T_{Flame} , [O] (or [O2]), and [N2]. For the presented data, NO production rates were calculated at each location along each flame edge. An average NO production rate for the test point was obtained for comparison to the

measured emissions by averaging over all valid locations of all instantaneous flame edges. The NO production rate for a specific location is a function of the data point ϕ_{jet} and the local mixture fraction. As f at the flame in each instance is not possible to determine with the method described in Section 2.4.2, the local mixture fraction is determined by superposition of the instantaneous flame edge on the expected mixture fraction field. Contributions from locations associated with a mixture fraction average that is comprised of less than 100 samples are discarded. The composition of the reacting mixture is a function of ϕ_{jet} and f and serve as parameters for a series of tabulated CHEMKIN equilibrium calculations. Values for T , $[O_2]$, and $[N_2]$ are extracted from the tabulated results for the specific mixture created from ϕ_{jet} and f . The local NO production rate is then calculated based on the following expression⁴ from Bowman [6], which is an extension of Equation 4 that also utilizes partial equilibrium assumptions to substitute $[O_2]$ for $[O]$:

$$\frac{d[NO]}{dt} = 1.45 \times 10^{17} T^{-1/2} [O_2]^{1/2} [N_2] e^{-69,460/T} \quad (16)$$

To highlight the sensitivity of NO production rate to the local mixture fraction, Figure 14 plots $d[NO]/dt$ as a function of f for three different values of ϕ_{jet} .

⁴ The units for $d[NO]/dt$ in this expression are in mol/cc*s. The data is presented in ppm/ms.

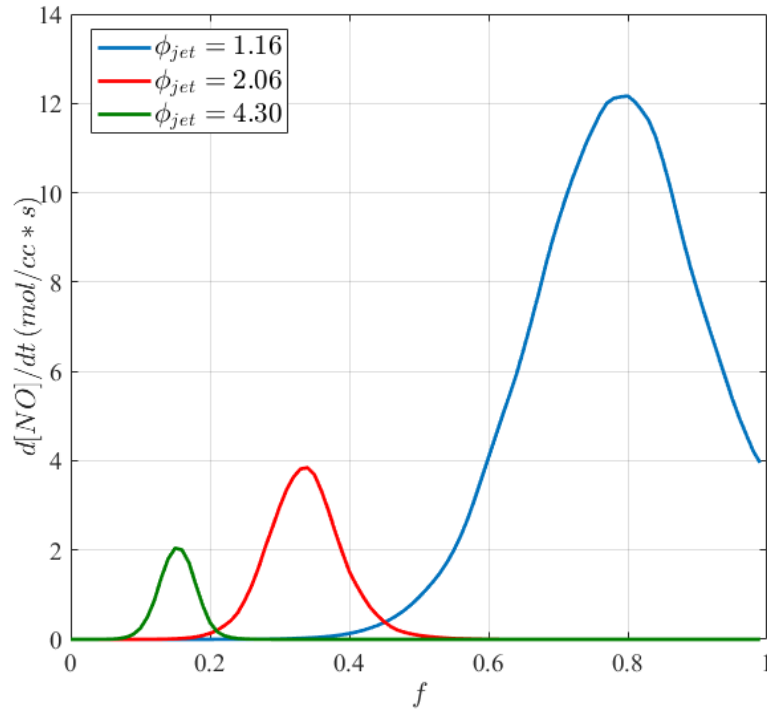


Figure 14 – NO production rates as a function of mixture fraction for select jet equivalence ratios.

2.5 Uncertainty Characterization

2.5.1 Uncertainty in Fluid Flow Rates

The metering system of the facility was very similar to that used for previous experimental investigations such as that conducted by Wilde [41]. In this work, Wilde extensively characterized the uncertainty of both the sub-critical orifice and critical orifice flow metering systems of the facility. The uncertainty in sub-critical flow systems, which include the main burner air and fuel flows, was evaluated as 1.79% of the flow measurement. The error in critical orifice flow metering, which include all jet fluid as well as the crossflow bypass air, was evaluated at 1.67% of the flow measurement.

2.5.2 *Uncertainty in NO_x Emissions*

The Horiba PG-350 gas analyser measures NO_x with a repeatability of $\pm 1.0\%$, linearity of $\pm 2.0\%$, and drift of $\pm 1.0\%$ per day referenced to the measurement range utilized. The majority of the data utilized a NO_x measurement range of 0 – 25 ppm. The Horiba was calibrated at the onset of every day of data collection with calibration points at 0 and approximately 22 ppm. As a result the drift was only taken to be $\pm 0.5\%$ and linearity is neglected for data in the vicinity of the calibration nodes.

All NO_x data reported in this thesis is corrected to 15% O₂. As such, the error in O₂ concentration measurement contributes to the uncertainty in reported NO_x. However, the resultant O₂ measurements from the tested system equivalence ratios were all in close proximity to the O₂ calibration node. Therefore, the linearity contribution from O₂ was neglected except for high ΔT test series, where O₂ levels were significantly different than the calibration node.

The uncertainty in the normalized NO_x metric introduced in Section 4.2.1, contains contributions from the uncertainty in the measurement of the two jet fuel stream mass flow rates in addition to the NO_x measurements. The uncertainty of the flow rates is addressed in Section 2.5.1. The resultant uncertainty is indicated on the relevant plots for each data point.

2.5.3 *Uncertainty in Particle Tracing of the Flow*

As noted in Section 2.4.2, a key assumption of the approach of using the Mie scattering images to determine mixture fraction is that the particle seed follow the fluid

flow. A key parameter in assessing the validity of this assumption is the Stokes number (Stk). Stk is a ratio of a particle response timescale (t_o) to a flow timescale (based on a flow scale of interest). High fidelity of flow tracing by the particle exists for $\text{Stk} \ll 1$, but in practice $\text{Stk} < 0.1$ provides tracing accuracy of less than 1% and is deemed negligible [52]. Two flow time scales will be used for comparison. As this analysis is focused on utilizing time average pre-flame mixing, a flow time scale associated with bulk fluid motion (t_∞) will first be considered. As the jet penetration is on the order of half the channel height, this will be the length scale used to calculate a bulk flow time scale. This yields $t_\infty = (1/2h)/u_j$. The highest J value in the investigated parameter space is 40, which combined with the fact that all of the jet density ratios were at 3 or slightly above gives a maximum potential bulk jet velocity of approximately 100 m/s. Combined with the 144 mm channel height yields $t_\infty = 570 \mu\text{s}$. The second flow time scale will be utilized to assess fluid motion related to the shear between the jet and crossflow and will use the jet radius as its length scale, yielding $t_j = (1/2d_j)/u_j$. The 6mm jet diameter combined with the maximum potential bulk velocity yields $t_j = 30 \mu\text{s}$.

Under Stokesian flow (i.e. creep flow), a particle response time (t_o) can be calculated with $t_o = \rho_p d_p^2 / 18\mu_g$, where ρ_p is the density of the particle ($\rho_p \approx 4 \text{ g/cm}^3$ for TiO_2), d_p is the particle diameter, and μ_g is the gas dynamic viscosity. In order to check the validity of the assumption that the particle is experiencing Stokesian flow, the Reynolds number of the fluid flow over the particle must be considered. Reynolds number of the particle (Re_p) is given by: $Re_p = u_p d_p / \nu_g$, where u_p is the magnitude of the velocity of the flow over the particle, in other words the relative velocity of the particle compared to the flow, and ν_g is the kinematic viscosity of the gas. The gas

kinematic viscosity will be lowest in the jet compared to the cross-section mainly due to the disparity in temperature. As even for the richest jets the jet fluid is still at least 70% air, the ν_g equal to that of air at 460K will be used in this analysis ($\approx 3 \times 10^{-5} \text{ m}^2/\text{s}$). Using the quoted value of ν_g , the upper limit of the particle diameter range (1 μm), and the maximum bulk jet velocity to create a very conservative estimate yields $Re_p = 3.33$. At this very conservative estimate, Re_p is still $O(1)$, and it is apparent for any realistic value of relative particle velocity that Re_p will be below unity, validating Stokesian assumptions.

Returning to the particle response time, using the dynamic viscosity of air at 460K makes for a conservative estimate of $t_o = 8.25 \mu\text{s}$. This particle response time yields Stokes numbers of $Stk_\infty = 0.014$ and $Stk_j = 0.275$. Based on these estimates of Stokes number it is clear that very little error is associated with the tracing of the particles for the bulk flow which is the focus of the work. However, it is also evident that the error in tracing the smaller scale fluid motion is significant and greater than 1%. It is worth noting however that this flow time scale equates to flow fluctuations on the order of 30 kHz, which the sampling frequency of 5 kHz is unable to resolve. This analysis demonstrates that the acquired data is adequate for its intended purpose of assessing time averaged pre-flame mixing.

CHAPTER 3. NITROGEN OXIDE SENSITIVITIES OF RICH PREMIXED REACTING JETS WITH LOW MOMENTUM FLUX

This chapter discusses the data obtained in the investigations detailed in Section 2.2.1. The discussion focuses on the sensitivity of flame lift-off distance to ϕ_{XF} , J , and ϕ_{jet} . Subsequently, the sensitivity of NOx emissions of these rich premixed methane/air jets to ϕ_{XF} , J , ϕ_{jet} , and LO is also assessed.

3.1 Liftoff Analysis of Rich Premixed Methane Jets

For all conditions reported in this chapter, the flame initiates on the leeward side of the jet. The observed RJICF flames present with a highly lifted windward branch to the point that they are deemed as lee-stabilized flames (defined in Section 1.3.2), or as fully lifted flames. This behavior is shown by the representative flame images in Figure 15.

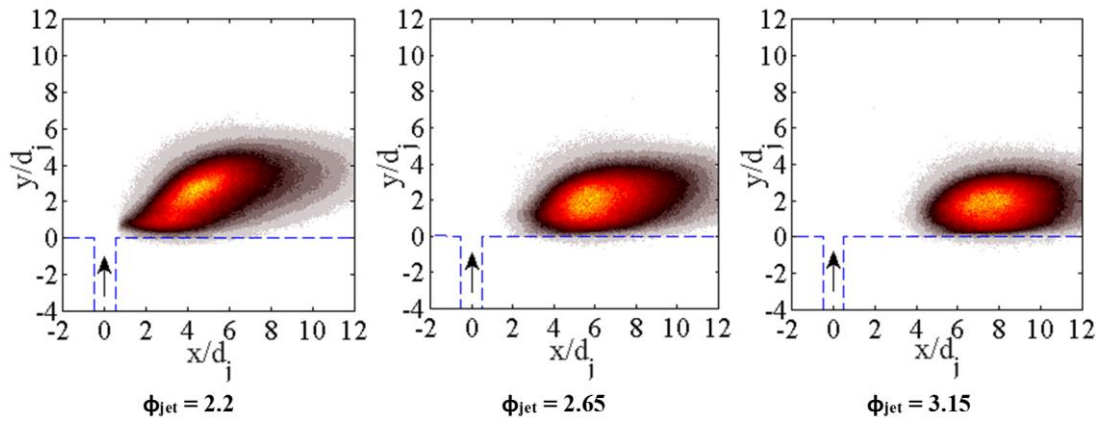


Figure 15 – Characteristic time averaged flame images. Images from test cases with constant crossflow conditions of $\phi_{XF} = 0.6$.

Figure 16 summarizes the results for LO as a function ϕ_{jet} , at a constant target exhaust temperature of 1956K. Also indicated on the figure are contours of constant crossflow

conditions (in the form of ϕ_{XF}), and J . First, Figure 16 indicates a clear sensitivity of LO to cross flow temperature; i.e., increasing ϕ_{XF} results in a reduction of LO , as expected. At constant crossflow conditions (constant ϕ_{XF} contour), LO increases with increasing ϕ_{jet} . Kolb *et al* [33] similarly demonstrated that flame lift-off height is a strong function of the crossflow temperature, jet temperature and jet equivalence ratio. For the data reported here, the trend between LO and ϕ_{jet} corresponds to a slight increase in LO with a reduction in J , due to the interdependent nature of J and ϕ_{jet} (described in Section 2.2). This appears as a departure from the Kolb *et al* [33], who demonstrated increases in lift-off with increases in J , over a range of J values from 6 – 210. However, Kolb *et al* [33] did not show significant change in liftoff for values of $J \leq 20$. In Chapter 4, RJICF with higher values of J will be addressed. The observed J sensitivity presented here may be due to jet stability effects [16] associated with low J jets, or simply a dominant ϕ_{jet} sensitivity. The impact of these relationships on NOx production is discussed further in Section 3.2.

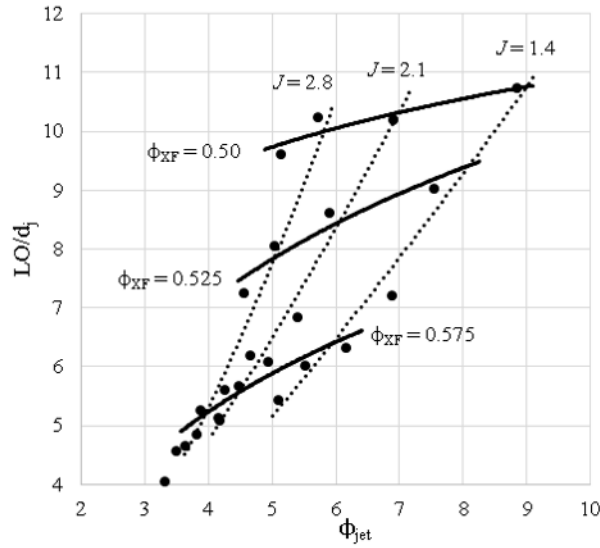


Figure 16 – Dependence of lift-off distance at constant exhaust temperature of 1956K upon the jet equivalence ratio. Contours of constant crossflow equivalence ratio (solid) and momentum flux ratio (dotted) are indicated.

3.2 Emissions of Rich Premixed Methane Jets

Figure 17 plots representative results for the NO_x production by the RJICF as a function of ϕ_{jet} , at $\phi_{XF} = 0.525$. Also indicated on the figure are contours of constant rise in system equivalence ratio due to the jet ($\Delta\phi$), J , and normalized flame liftoff, LO/d_j . $\Delta\phi$ is used as a measurable surrogate for ΔT in this discussion. It is highly correlated to ΔT or the secondary fuel mass flow rate in a linear fashion for this range of conditions. Immediately apparent from Figure 17 is a clear monotonic relationship between ΔNO_x and $\Delta\phi$ at a given ϕ_{XF} . Thus, as ΔT increases so does RJICF NO_x production, which is congruent with the primary sensitivity of RJICF NO_x production identified by Roa *et al* [39].

One of the questions highlighted in the introduction concerns the factors that influence NO_x production at a given ΔT , as the majority of available data has ΔT varying

with other parameters, such as J . Insight into this question is possible by following a fixed $\Delta\phi$ line. At constant values of $\Delta\phi$, the figure shows that the lower J and richer jets produce less NOx than their less rich and higher J counterparts.

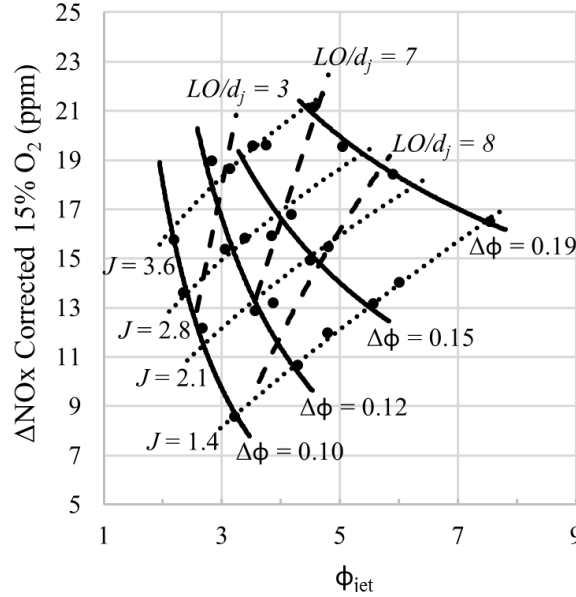


Figure 17 – Dependence of reacting jet NOx contribution at constant crossflow conditions of $\phi_{XF} = 0.525$ upon the jet equivalence ratio. Contours of constant temperature rise (solid), momentum flux ratio (dotted), and lift-off distance (dashed) are indicated.

Figure 18 plots the same parameters, except at $\phi_{XF} = 0.625$. The increase in ϕ_{XF} implies a hotter crossflow, which also reduces LO , as shown. Again, the figure shows a rise in ΔNOx as the fuel flow rate into the jet increases, quantified by $\Delta\phi$ for a given J value. For a given $\Delta\phi$ value, it is clearly evident by the contours of differing momentum flux ratio that the richer, lower J jets are producing less NOx than their less rich, higher J counterparts, as also demonstrated in Figure 17.

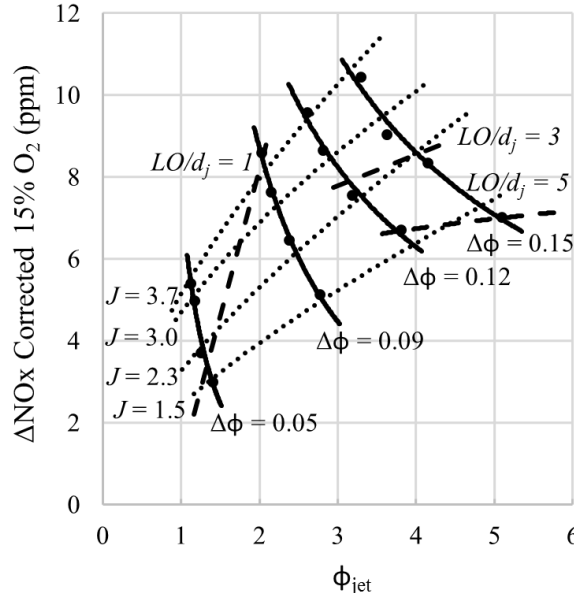


Figure 18 – Dependence of reacting jet NOx contribution at constant crossflow conditions of $\phi_{XF} = 0.625$ upon the jet equivalence ratio. Contours of constant temperature rise (solid), momentum flux ratio (dotted), and lift-off distance (dashed) are indicated.

Referring to the contours of constant LO/d_j presented in Figure 17 and Figure 18, the sensitivity of lifting to crossflow temperature and ϕ_{jet} is again evident. The values of LO associated with the lower crossflow temperature case (Figure 17) are significantly higher for similar values of ϕ_{jet} than for the high crossflow temperature case (Figure 18). Also as previously discussed in Section 3.1, at constant crossflow conditions and ΔT , LO increases with increasing ϕ_{jet} and decreasing J . In addition, Figure 17 and Figure 18 also show an increase in LO as J decreases with constant ϕ_{jet} . As this increase in LO at constant ϕ_{jet} involves a reduction in $\Delta\phi$, changes in heat release, in combination with the aforementioned jet stability effects, is a potential driver of the observed J sensitivities presented here.

Figure 17 and Figure 18 show contours of constant LO cutting across lines of constant $\Delta\phi$. For constant $\Delta\phi$, ΔNOx decreases with increasing LO . This is associated with

an increase in ϕ_{jet} which has already been shown to correspond to a reduction of ΔNO_x at constant $\Delta\phi$. For constant ϕ_{jet} , ΔNO_x decreases with increasing LO as well. This is associated with a decrease with $\Delta\phi$, which has been shown to correlate with NO_x production. While flame lifting certainly has an impact on NO_x formation, as Kolb *et al* [33] has similarly demonstrated for a lean premixed jet, LO is itself sensitive to parameters such as ϕ_{jet} , J , and crossflow temperature that directly impact NO_x contribution of the reacting jet.

It is important to note the extent by which ΔNO_x varies along a contour of constant $\Delta\phi$. Variations in ΔNO_x ranging from 1.5x up to 3x are found in Figure 17 and Figure 18. This variation is considerable. Furthermore, when compared to the change in ΔNO_x across $\Delta\phi$, at either constant J or ϕ_{jet} , it is clear that it is on the same order of magnitude.

The high equivalence ratio of these jets introduces considerations not touched upon in Chapter 1. First, while it was discussed in Section 1.3 that the stoichiometry at which combustion occurs in a RJICF is critical, due to the strong temperature sensitivity of thermal NO_x production rates, the impact of this stoichiometry on other sources of NO_x was not touched upon. Other mechanisms of NO_x production besides thermal NO_x were omitted from the context laid out in Section 1.1 due to their relative insignificance at DLN combustor operating conditions. However, for rich premixed flames, NO_x production within the flame (prompt NO_x) via the Fenimore mechanism can be significant and is sensitive to equivalence ratio. For this prompt contribution, the rate at which the cyano compounds (e.g. CN and HCN) react to produce NO versus N_2 is dependent on equivalence ratio [6]. Second, for rich premixed burning of the fuel jet, the excess fuel that is not oxidized will be in the form of diluted synthesis gas, H_2/CO , that can subsequently burn

either as a non-premixed flame or, if it premixes with the crossflow prior to combustion, as a premixed flame. The stoichiometry of this H_2/CO combustion will have as significant an impact on product temperature, and therefore NO_x production, as the initial methane combustion.

3.3 Summary of Chapter Findings

The work presented in this chapter investigates the emissions characteristics and flame behavior of rich premixed methane/air jets into a high temperature vitiated crossflow. The results address, in part, the research questions outlined in Section 1.4 and also raise additional concerns.

As anticipated, reacting jet NO_x production has been shown to be monotonically increasing with increasing $\Delta\phi$ at constant crossflow conditions. The data presented in this chapter did however demonstrate that NO_x production could vary significantly for reacting jets of similar $\Delta\phi$. This finding directly addresses the second central research question of this thesis, whether any NO_x sensitivities are of the same order as the dependence on ΔT . As to what those key driving parameters are: both ϕ_{jet} and LO were indicated as potential governing parameters. These parameters in conjunction with JICF mixing rates are likely to heavily impact NO_x production due to their influence over the stoichiometry achieved during the pre-flame mixing region. However, due to their interdependent nature both with each other and other RJICF parameters such as J , it was not possible to isolate the impact of either on NO_x production.

Chapter 4 further investigates the sensitivities highlighted here and applies the discussion to a much broader parameter space with regards to ϕ_{jet} and J . Great effort is made towards

isolating the impact of each parameter. Chapter 4 also focuses more directly on how these parameters of interest impact the equivalence ratio of combustion as well as address the concerns raised in Chapter 3 with regards to combustion at highly rich equivalence ratios: namely prompt NO_x contributions and combustion of product synthesis gas.

CHAPTER 4. NITROGEN OXIDE SENSITIVITIES OF PREMIXED REACTING JETS

This chapter presents the results for lift-off distance and NOx production in reacting jets with the parameter space described in Section 2.2.2. The results are organized by first discussing the observed regimes of flame stabilization / lifting behavior, followed by the NOx emissions. In each instance, the data associated with the pipe exit geometry and $J \leq 20$ is used as a reference set to explore the impact of the various RJICF parameters. All data is denoted via the scheme presented in Table 3. Circular points are used for the pipe exit geometry data, triangles for the nozzle exit geometry data, hollow circles are used to denote pipe geometry points with $J = 40$, and x's are used for the forced lifting points via methane doping. In addition all points have a color corresponding to their crossflow condition, with blue for $\phi_{XF} = 0.45$ and red for $\phi_{XF} = 0.50$.

Table 3 – Symbol legend for CHAPTER 4 figures

●	Data from pipe exit geometry
▲	Data from nozzle exit geometry
○	Data from pipe exit geometry with $J = 40$
×	Data from methane doped pipe exit geometry
	$\phi_{XF} = 0.45$
	$\phi_{XF} = 0.50$

Finally, two pipe geometry data points and one nozzle geometry data point oscillated in LO value between lee-stabilized and “lean lifted” flame stabilization. These points are not plotted because of their intermittent behavior.

4.1 Lifting Behavior of Premixed Ethane Jets

As noted in Section 1.3.2, flame lifting has significant influences on pre-flame mixing. As such, while the primary focus of this paper is on NO_x emissions, it is appropriate to first describe *LO* characteristics, as it will subsequently be used as a scaling parameter. All flames considered here were either stabilized on the leeward side of the jet (with lifting of the windward side), or fully lifted. Figure 19 shows measured flame *LO* values as a function of reduced ϕ_{jet} for those jets with $J \leq 20$ ($J = 40$ points are lifted for all ϕ_{jet} values and will be considered further starting in Section 4.2.3).⁵ The results are indicated as described in Table 3. A secondary axis for ϕ_{jet} is also included for reference. Values of LO/d_j of less than 3 are considered lee-stabilized based on similar behavior presented in the flame probability maps, and values greater than 3 are considered fully lifted.

⁵ Reduced $\phi_{jet} \equiv 2\phi_{jet}/(1 + \phi_{jet})$. It was selected to assist in plotting data with such a large range for ϕ_{jet} .

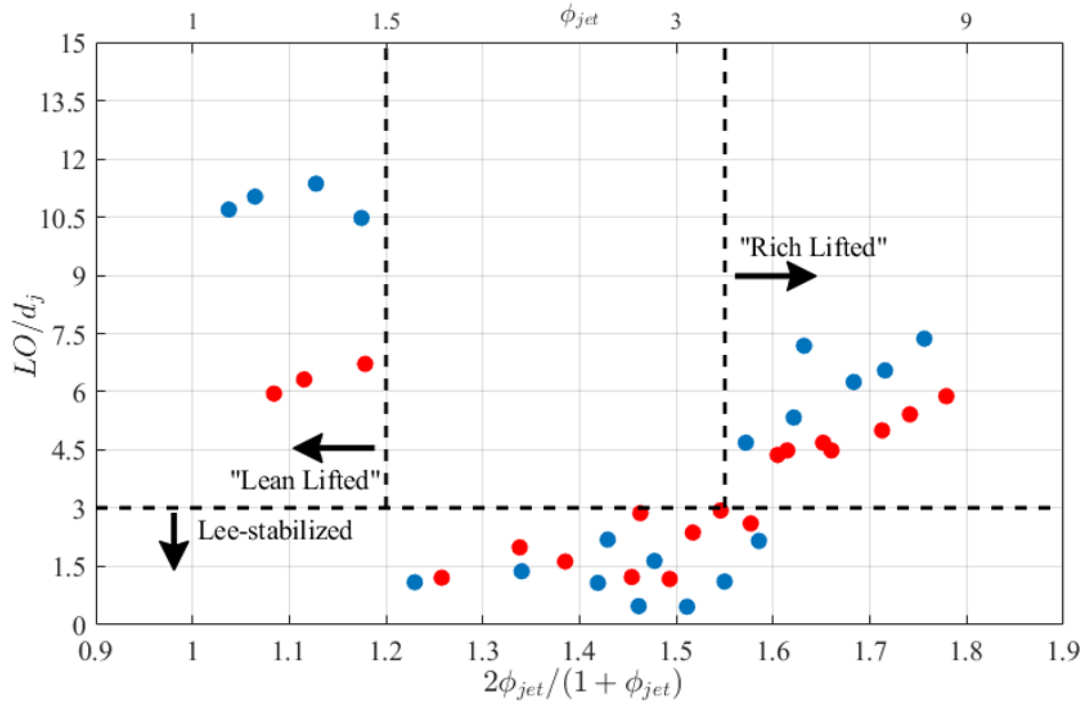


Figure 19 – Lift-off distance for jets with $J \leq 20$ as a function of reduced equivalence ratio for pipe exit geometry at constant crossflow conditions of $\phi_{XF} = 0.45$ and $\phi_{XF} = 0.50$.

Immediately apparent in Figure 19 is the presence of a region of jet equivalence ratios where the flame exhibits lee-stabilized behavior. In addition two branches of fully lifted behavior exist, one with values of ϕ_{jet} lower (more fuel lean) than the central region of lee-stabilization and one with higher (more fuel rich) values of ϕ_{jet} . These branches will be referred to as “lean lifted” and “rich lifted” respectively. It is important to note that, as shown in Figure 19, the transition to “lean lifted” is much more abrupt with respect to jet stoichiometry than the transition to “rich lifted.”

Note the impact of crossflow temperature on LO . Specifically, increases in temperature (due to increases in ϕ_{XF}) reduce LO of the fully lifted branches, as expected. Little change is observed in the transitions between fully lifted and lee-stabilized behavior.

No significant variation in LO due to J (for $J \leq 20$) was observed, with ϕ_{jet} and ϕ_{XF} emerging as the governing parameters of LO . Both Kolb *et al* [33] and the results presented in Section 3.1 also observed a strong dependence of flame lift-off height (or distance) on crossflow temperature. The dependency on ϕ_{jet} is in agreement with the results presented in Section 3.1. Kolb *et al* [33] did observe an increase lift-off height as J was increased. However, Kolb *et al* [33] observed this behavior across J values ranging from 6 – 210, but showed little change in lift-off for J values of 20 and below.

4.2 NOx Emissions Behavior in Premixed Ethane Jets

4.2.1 Raw NOx Emissions of Premixed Jets

Figure 20 plots the NOx production from the RJICF (ΔNO_x) as a function of ΔT . ΔNO_x is calculated by subtracting a baseline crossflow NOx level (Section 2.3.1) from the measured reacting jet emissions. The data are indicated as per Table 3, with the uncertainty in the ΔNO_x measurement displayed with error bars. Immediately apparent from Figure 20 is the monotonic, nearly linear, overall relationship between NOx production and ΔT . Also evident is the variation in NOx at a given ΔT . Depending on ΔT , this variation can be on the order of 2x. The relationship with ΔT is congruent with literature [36, 38, 39] and the results presented in Section 3.2 are in agreement with both this relationship and the potential variation at constant ΔT .

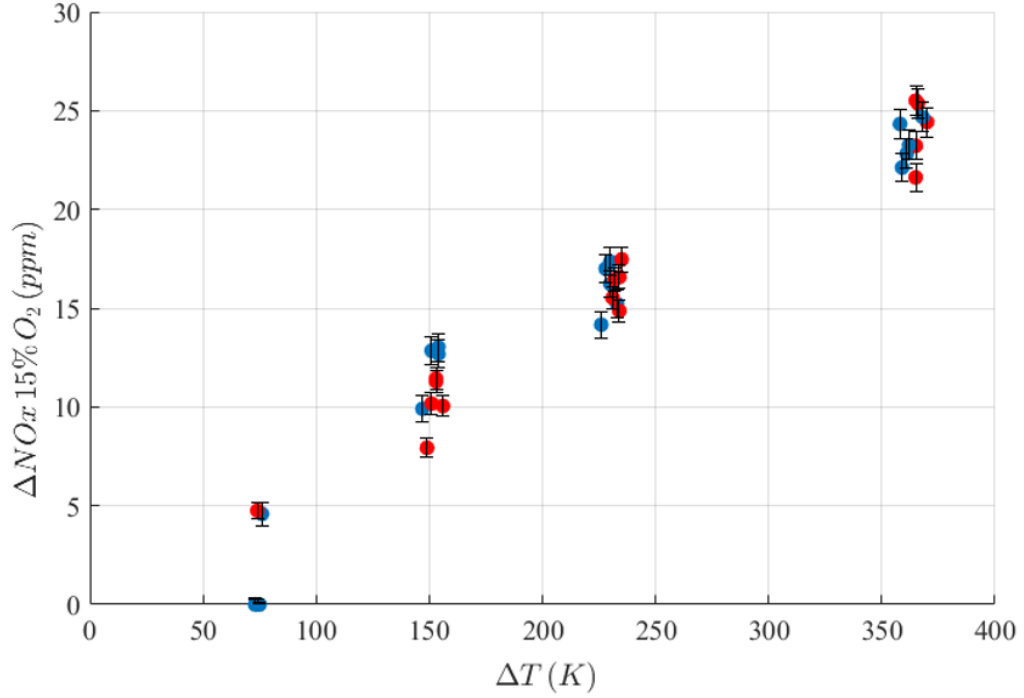


Figure 20 – RJICF NOx production as a function of ΔT at constant crossflow conditions of $\phi_{XF} = 0.45$ and $\phi_{XF} = 0.50$.

It is useful to normalize the impact of varying ΔT on NOx, to better facilitate analysis of other NOx drivers. To this end, an effective fuel mass flow in the jet (\dot{m}_{ef}) was chosen, and is defined as:

$$\dot{m}_{ef} = \dot{m}_{C_2H_6} + \frac{LHV_{CH_4}}{LHV_{C_2H_6}} \dot{m}_{CH_4} \quad (17)$$

where \dot{m} and LHV are the mass flowrates in the jet and lower heating value, respectively. Values for both ethane and methane are used and are denoted by their respective chemical formulas in the subscript. This normalization parameter was chosen for three reasons: first, fuel mass flow rate is more accurately measureable than ΔT itself and is commonly used as a normalization parameter (e.g. to calculate Emission Index [36, 37]); second, weighting

\dot{m}_{CH_4} by the ratio of the lower heating values accounts for the difference in heat release per kg of the two fuel species; third, it is nearly linear with ΔT values, as shown by adiabatic flame temperature calculations.

4.2.2 Sensitivity of Emissions to Jet Equivalence Ratio

Results presented in Section 3.2 identified both ϕ_{jet} and LO as influencing RJICF NOx emissions, but their effects were strongly coupled. To look into the effects of these parameters further, the fully developed velocity profile data is used as a reference. Trends discussed in this section are the same for the top hat velocity profile (exit velocity profile effects are discussed in detail in Section 4.2.4). Figure 21 plots ΔNOx normalized by \dot{m}_{ef} as a function of reduced ϕ_{jet} for RJICF and $J \leq 20$. The data is indicated per Table 3.

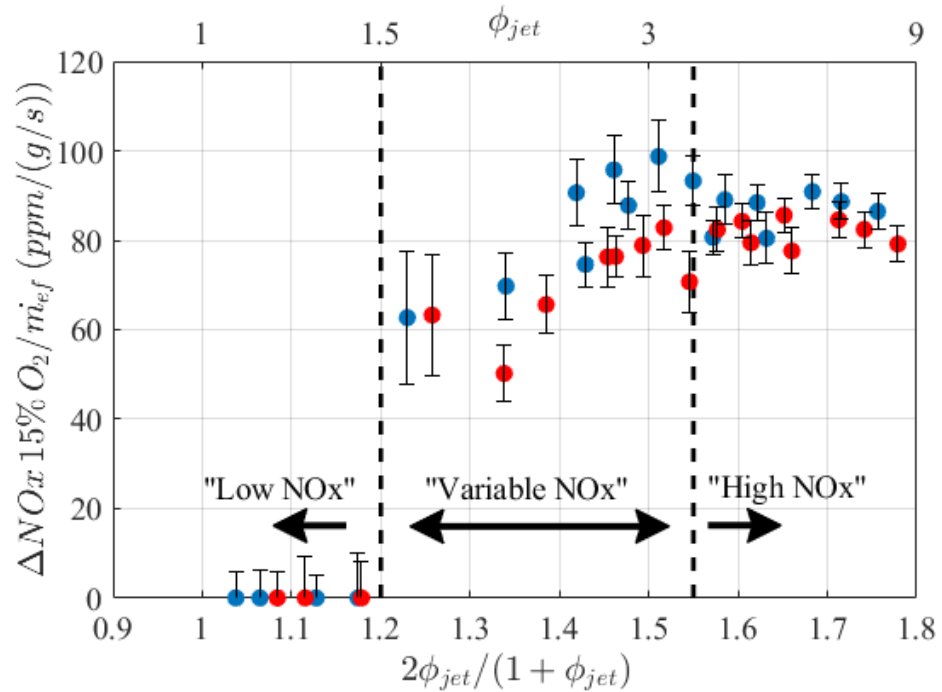


Figure 21 – Normalized NOx production as a function of reduced equivalence ratio for reacting jets with a pipe jet geometry and $J \leq 20$ at constant crossflow conditions of $\phi_{XF} = 0.45$ and $\phi_{XF} = 0.50$.

Figure 21 reveals three regions. At reduced equivalence ratios below 1.2, a region of negligible NOx production exists,⁶ labeled “low NOx”, regardless of ϕ_{jet} value. In this region, the flames are all lifted. At reduced jet equivalence ratios between 1.2 and approximately 1.5, labeled “variable NOx”, the flames are lee-stabilized and the NOx generated monotonically increases with ϕ_{jet} . In other words, for these lee-stabilized flames, the NOx production is dependent on ϕ_{jet} . Above the reduced ϕ_{jet} value of ~ 1.55 , labeled “high NOx”, the normalized NOx contribution for this region is relatively invariant with changes in ϕ_{jet} . This sensitivity, or lack thereof, of normalized NOx production on ϕ_{jet} is associated with distinct flame stabilization behaviors. The ϕ_{jet} dependent region is associated with lee-stabilized flames, and the ϕ_{jet} invariant regions are associated with fully-lifted flames, either “lean lifted” or “rich lifted”.

4.2.3 Sensitivity of Emissions to Flame Lift-Off Distance

Consider further the impact of LO on NOx emissions, by examining normalized ΔNOx values as a function of LO . These data for RJICF with a pipe exit geometry and $J \leq 20$ are presented in Figure 22. The different flame lifting regimes and stoichiometries are also noted.

⁶ The emissions measurements for these cases were within the error of the associated base NOx measurement. They are plotted as having a normalized ΔNOx value of 0 with the positive portion of their error bars.

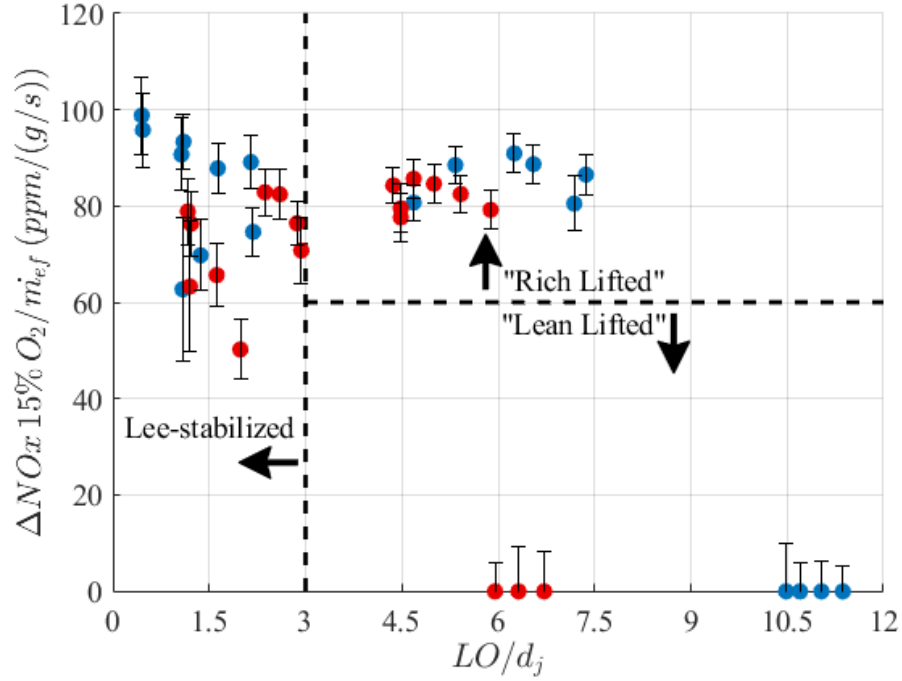


Figure 22 – Normalized NOx production as a function of LO for reacting jets with a pipe jet geometry and $J \leq 20$ at constant crossflow conditions of $\phi_{XF} = 0.45$ and $\phi_{XF} = 0.50$.

Figure 22 makes it immediately apparent that, while lifting has a significant impact on NOx production, NOx emissions are not linearly correlated to LO . Rather, the results fall into the three groups, using the lee-stabilized, “rich lifted”, and “lean lifted” identifiers. The negligible NOx solution is clearly associated with reacting jets exhibiting the “lean lifted” behavior discussed in Section 4.1, and high NOx is associated with both lee-stabilized and “rich lifted” reacting jets (also discussed in Section 4.1). The lee-stabilized jets show significant variation in NOx; as shown in the prior section, these NO variations are associated with variations in ϕ_{jet} . The “rich lifted” jets display the reverse, a range of LO values with invariant NOx production.

It is important to note the interdependencies of ϕ_{jet} and LO when interpreting these data. All variations in LO observed in Figure 22 are accompanied by changes in ϕ_{jet} , as

shown in Figure 19. We next consider the methane doped and $J = 40$ results, which allow for variations in LO that are independent or much less sensitive to ϕ_{jet} . In all repeated cases, ϕ_{jet} and J are identical to the corresponding pure ethane case. The impact of the methane doping and high momentum flux is primarily the same: to induce fully-lifted behavior in the intermediate ϕ_{jet} range that is associated with lee-stabilized flames in the pure ethane, $J \leq 20$ cases.⁷ The methane doping had the additional effect of increasing LO in “rich lifted” reacting jets. For reference, Figure 38 plots these measured flame LO results in Appendix A.2.

The normalized emissions of the pipe geometry data (shown in Figure 21) with the addition of methane doping and $J = 40$ data added is shown in Figure 23.

⁷ Note also that the high J cases show that there is a J impact on LO . These observations are consistent with Kolb *et al* [33] who noted lifting in flames with J values on the order of 60 and above, and a J sensitivity of LO for these higher J values.

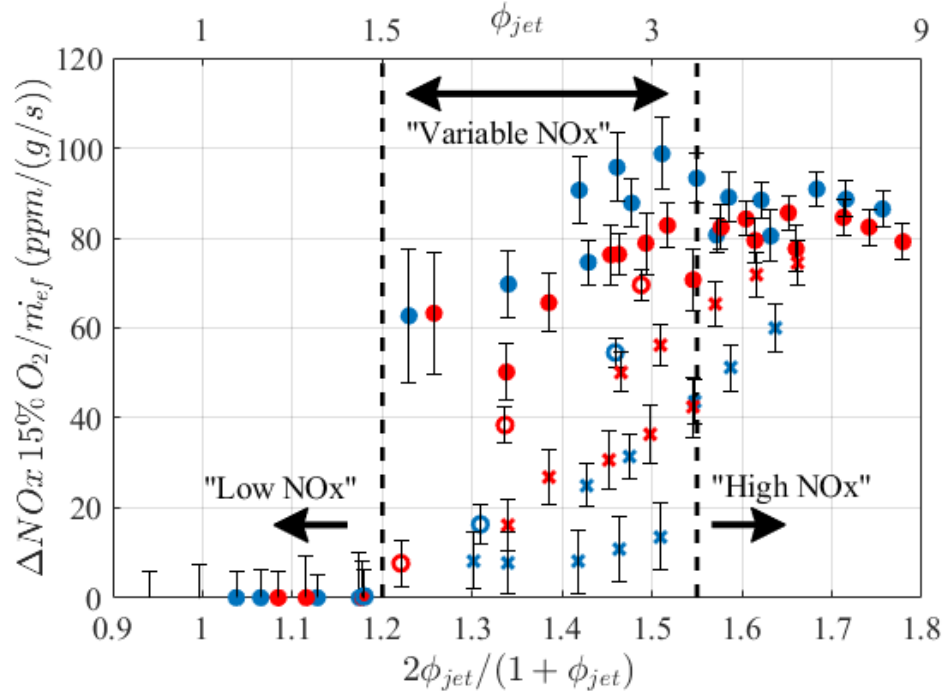


Figure 23 – Normalized NOx production as a function of reduced equivalence ratio for reacting jets (including high J and methane doped) with a pipe jet geometry at constant crossflow conditions of $\phi_{XF} = 0.45$ and $\phi_{XF} = 0.50$.

Every $J = 40$ and methane doped point at similar ϕ_{jet} , compared to $J \leq 20$ data, has a significantly higher LO . The key takeaway from Figure 23 is that in every instance, this increase in LO is associated with significant NOx reduction, as expected based upon pre-flame mixing considerations. To more explicitly explore how the increase in LO impacts NOx production, Figure 24 compares data point pairs between the doped and undoped cases for otherwise identical conditions. Specifically, it plots the change in NOx production due to the doping of the jet fuel with methane as a percentage of the corresponding undoped normalized emission. This metric is plotted as a function of the corresponding change in LO due to the methane doping. In addition a least squares fit line with a forced intercept of unity is included. This fit will be utilized in Section 4.2.4.

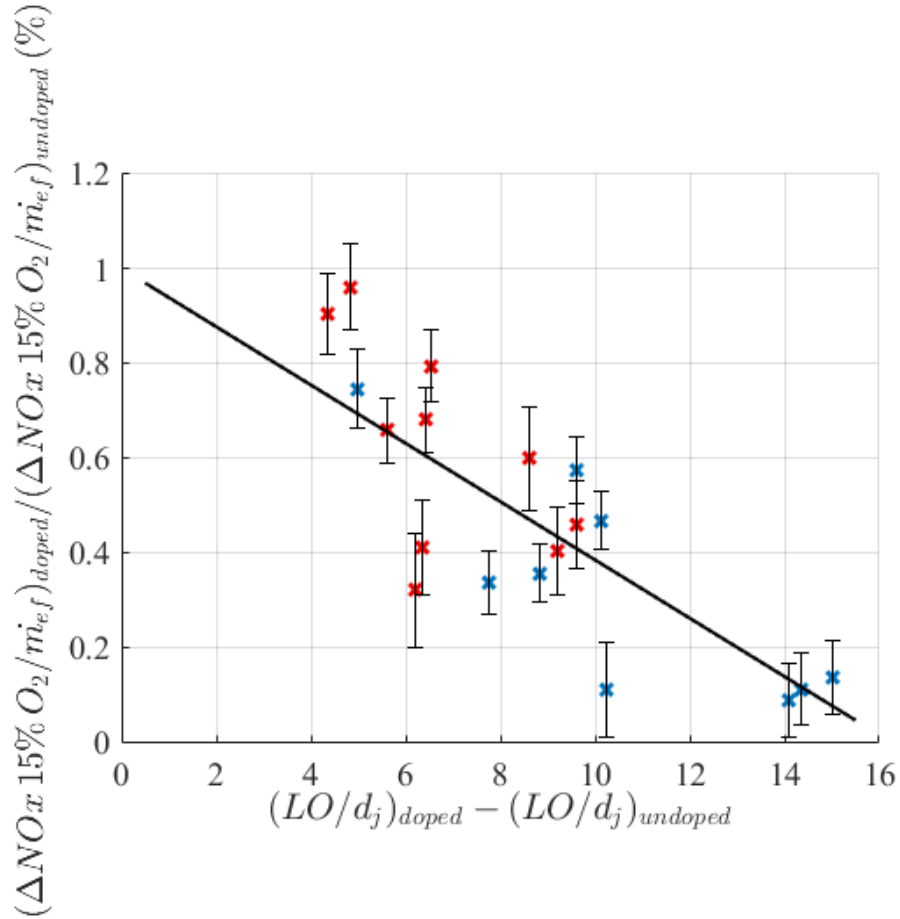


Figure 24 – Fraction of NOx production from ethane/methane/air reacting jets compared to ethane/air reacting jets (all with pipe exit geometry) as a function of the associated change in LO . For each point all other test parameters remain constant between the two different compositions.

Figure 24 shows a reduction in NOx with increased LO , and quantifies the effect of lifting on the NOx production of RJICF. In general, larger increases in LO are associated with larger reductions in NOx. Note that significant fractional reductions in NOx production are possible by lifting the flame, all other conditions being equal. While not unexpected, this result clearly shows the importance of engineering designs that enhance flame lifting for NOx minimization from RJICF. It is important to note that CO levels of the exhaust were monitored during the experiment. CO levels did not rise significantly for the doped data, indicating the reduction in NOx is not due to partial oxidation of the fuel.

4.2.4 Impact of Exit Velocity Profile on Emissions

This section considers the impact of jet exit velocity profiles on NO_x production. More fundamentally, these velocity profiles influence *LO* and shear layer growth rates and, consequently, pre-flame mixing rates. For example, several studies [20, 22] have observed more rapid nearfield mixing of the jet with crossflow for nozzle geometries compared to pipe geometries. This increase in mixing rates can be tied back to the sensitivity of the SLV growth rate to jet exit shear layer thickness. The disparity in SLV growth for the different exit velocity profiles can be inferred qualitatively from Figure 25, which shows Mie scattering images from identical rich lifted cases. The images were obtained as described in Section 2.3.4.

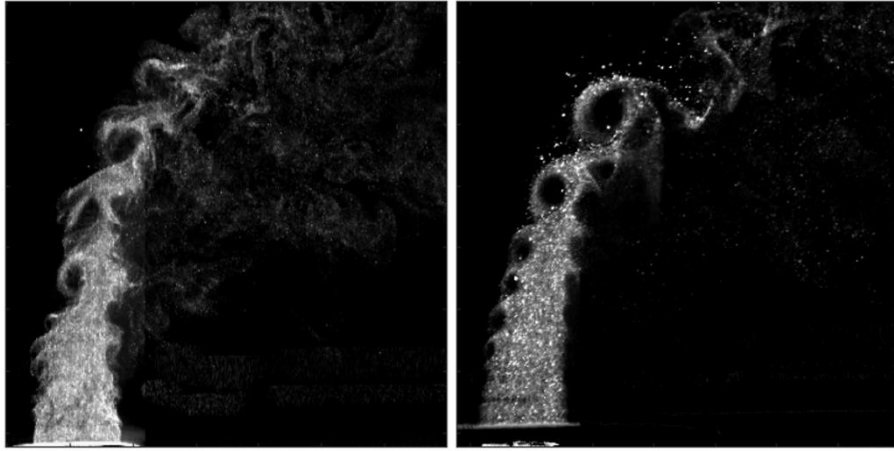


Figure 25 – Mie scattering images of reacting jets in crossflow with a pipe (left) and nozzle (right) exit velocity profiles. Both jets have identical composition, $\phi_{jet} = 4.73$, and $J = 15$.

Because the velocity profile influences both *LO* and SLV growth rates, care must be taken in elucidating the relative effects. There is a slight reduction in *LO* value for the top hat exit velocity profile relative to the fully developed profile for cases where the flame is

lifted. In addition, the nozzle geometry jets transition from “lean lifted” to lee-stabilized at lower values of ϕ_{jet} than the jets with pipe injection geometry. These results are illustrated in Figure 39 in Appendix A.2.

Consider next the SLV growth rate impact of the two jet geometries. Figure 26 plots the ratio of NOx production from the nozzle jet profile to that from the pipe case. In order to exclude the *LO* impact noted above, the following procedure was used for comparison of data points. Data associated with “lean lifted” flames are not plotted as the NOx production remains negligible in the “lean lifted” cases for the nozzle geometry. Also excluded are the transitional ϕ_{jet} points where one geometry is lifted and the other attached. For the remaining points that are to be discussed next, the nozzle geometry has a lower *LO* relative to the pipe geometry that is on the order of a single jet diameter, as shown in Figure 39. The data for the subset just described are adjusted using the linear fit in Figure 24 back to constant *LO* values, which changes the raw ratios by about 5% to account for the slight difference in *LO* values between the two geometries.

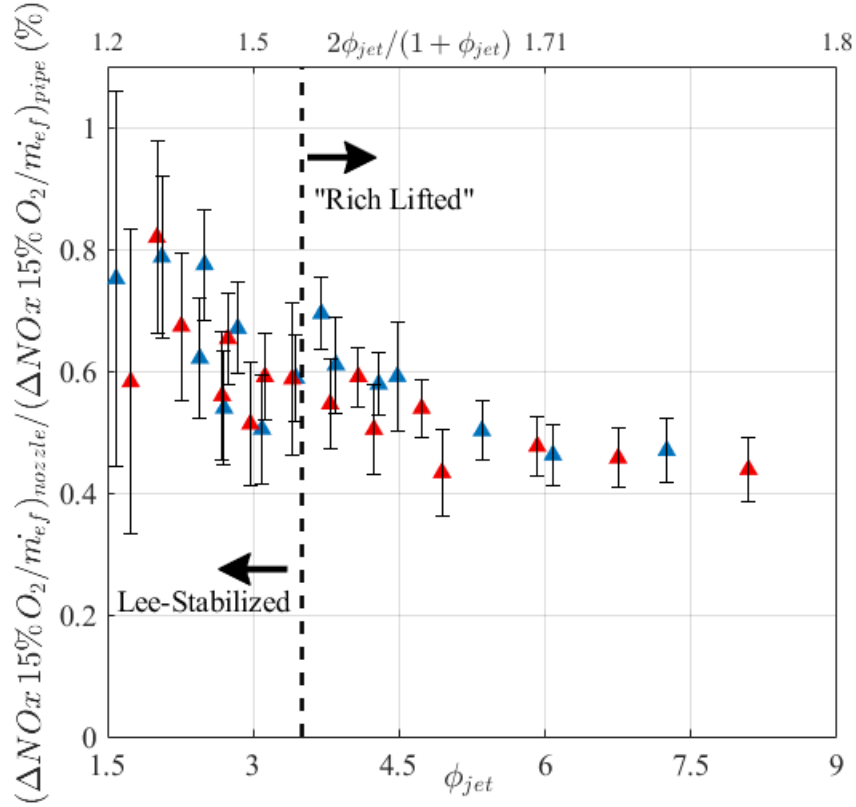


Figure 26 – Fraction of NOx production from reacting jets with nozzle geometry compared to reacting jets with pipe geometry as a function of the associated change in ϕ_{jet} .

Figure 26 shows that the NO production from the nozzle geometry is about 20-55% lower than that corresponding to the pipe geometry. The magnitude of this reduction is dependent on ϕ_{jet} (which is accompanied by variations in LO) with larger reductions in NOx for richer jet stoichiometry. This effect does level off at very rich equivalence ratios ($\phi_{jet} > 4.5$) with NO levels asymptoting to approximately 45% of those found for the pipe geometry. This demonstrates that, at low LO , the magnitude of the impact of a change in exit velocity profile is more significant with higher ϕ_{jet} . As LO increases to fully lifted values the impact is constant and invariant with both LO and ϕ_{jet} . As with the methane doped cases, no accompanying rise in CO with the reduction in NOx was observed.

These results are consistent with the hypothesis that the increase in shear layer growth with the nozzle geometry increases pre-flame mixing rates, and drives down NOx production; e.g., the NO reduction effect increases as ϕ_{jet} and LO increase. However, the fact that a reduction is observed even for attached flames, where the pre-flame mixing is reduced, suggests that post-flame mixing effects are also present. Since the downstream CVP structures that would influence post-flame mixing are themselves ultimately due to the re-orientation of SLVs, it is reasonable to expect a coupled influence of pre- and post-flame mixing effects. Further work is needed to develop approaches to decouple pre- and post-flame mixing and to quantify their relative impacts on NOx.

4.3 Equivalence Ratio of Combustion Considerations

Overall, the data presented in this chapter are consistent with the hypothesis that within constant ΔT NOx emissions are controlled by the stoichiometry at which combustion actually occurs, which will be referred to as ϕ_{Flame} . The objective of this section is to explore this hypothesis.

ϕ_{Flame} is influenced by ϕ_{jet} , as well as pre-flame mixing of the jet and crossflow, captured in this investigation by nozzle geometry and LO . Consider the impact of LO and ϕ_{jet} on ϕ_{Flame} . For a fixed crossflow condition, ϕ_{jet} serves as the initial condition for the evolving stoichiometry of the reactants. In turn, LO controls the spatial duration over which pre-flame mixing occurs. The spatial duration can be transformed into a temporal one by utilizing the jet exit flow velocity, $\tau_{pre-flame} = LO/u_j$. The rate of mixing during this time is a function of the flowfield, which in turn is a function of the instability of the SLVs (most strongly influenced by exit velocity profile in this data).

The three branches of NOx emissions shown in Figure 21 are readily interpretable with this approach. As a reminder, the three branches are: negligible NOx production associated with “lean-lifted” flames, ϕ_{jet} dependent NOx production in lee-stabilized flames, and high NOx production in “rich-lifted” flames that is invariant with LO and ϕ_{jet} .

For the negligible NOx case, the low NOx production suggests a lean ϕ_{Flame} value and therefore low flame temperatures. This interpretation is supported by the lower ϕ_{jet} values and large LO values associated with the low NOx production cases, indicating a well-mixed jet and crossflow. It would also account for the lack of sensitivity to either LO or ϕ_{jet} . As long as the resulting value of ϕ_{Flame} due to the variation of these parameters is below the threshold of significant NO production, the reacting jet NOx emission would remain negligible. In the lee-stabilized regime of increasing NOx with increasing ϕ_{jet} , this correlation would indicate that ϕ_{Flame} is varying with ϕ_{jet} . Due to the much more limited variation of LO in this region, it stands to reason that ϕ_{Flame} and ϕ_{jet} are much more closely coupled. The “rich-lifted” data exhibits near constant NOx levels. This would suggest a more constant value of ϕ_{Flame} , and a decoupling of its value from ϕ_{jet} . Due to the elevated emissions levels, the value of ϕ_{Flame} would most likely be near stoichiometric combustion and its high flame temperatures. The lack of sensitivity of NOx to LO or ϕ_{jet} in this region is due to the variation of these parameters in combination with the fluid mechanic mixing rate to achieve roughly constant ϕ_{Flame} . Near stoichiometric ϕ_{Flame} would also have a high flame speed to assist with stabilization, and would also be the non-premixed limit as ϕ_{jet} increases towards pure fuel.

The reduction in NOx associated with increased LO or increased fluid mechanic mixing rate (exit velocity profile) at fixed conditions shown in Figure 24 and Figure 26 can

also be re-interpreted from the perspective of ϕ_{Flame} . In both cases, ϕ_{Flame} is driven to leaner values by the increase in duration or rate (or both) of the pre-flame mixing region at fixed ϕ_{jet} . This is consistent with the hypothesis that a reduction in ϕ_{Flame} leads to a reduction in NOx as plotted in Figure 24 and Figure 26.

These pre-flame mixing ideas can be further explored through the use of a simple mixing model. Consider the RJICF pre-flame mixing as a parcel of fluid at an initial stoichiometry (ϕ_{jet}) that entrains and/or exchanges mass with the crossflow reservoir at a lower equivalence ratio (ϕ_{XF}). The spatial rate of change of the equivalence ratio of that parcel of fluid would be proportional to a mixing rate and the difference between the equivalence ratio of the parcel and the crossflow with which it is mixing; i.e:

$$d\phi/dr = -1/\ell_m (\phi - \phi_{XF}) \quad (18)$$

where r is the distance from the jet exit, and ℓ_m is a mixing length scale. Solving this equation with $\phi = \phi_{jet}$ as an initial condition and $\phi = \phi_{Flame}$ at LO yields the following:

$$\phi_{Flame} = (\phi_{jet} - \phi_{XF})e^{-LO/\ell_m} + \phi_{XF} \quad (19)$$

This relationship can be also be recast as the following relationship between LO and ϕ_{jet} :

$$LO/d_j = \ell_m/d_j \ln(\phi_{jet} - \phi_{XF}) - \ell_m/d_j \ln(\phi_{Flame} - \phi_{XF}) \quad (20)$$

The above discussion hypothesized that constant normalized NOx (such as in the “rich lifted” regime) corresponds to a constant value of ϕ_{Flame} . If ϕ_{Flame} is constant for a

given set of data (i.e., independent of LO and ϕ_{jet}), Equation 20 predicts a linear relationship between LO/d_j and $\ln(\phi_{jet} - \phi_{XF})$, with a slope and y-axis intercept of ℓ_m/d_j and $\ell_m/d_j \ln(\phi_{Flame} - \phi_{XF})$, respectively.

Motivated by Equation 20, Figure 27 plots LO as a function of $\ln(\phi_{jet} - \phi_{XF})$ for three subsets of data with a linear fit shown for each subset. The first set (Case 1) is the “rich lifted” points associated with the pipe exit geometry (solid fit line). The second set (Case 2) is the “rich lifted” points associated with the nozzle exit geometry (dash-dot fit line). Both of these sets have normalized NOx levels that are invariant with ϕ_{jet} and LO ; thus, we anticipate a linear trend and a lower slope of the nozzle data than the pipe data due to the faster mixing rates. The third subset (Case 3) is selected from the methane doped pipe exit geometry data based on self-similar NOx values (dotted fit line). Due to being fully lifted RJICF with a pipe exit geometry, a linear relationship with a similar slope to Case 1 but a significant shifted intercept (due to a different ϕ_{Flame} value) is anticipated. These three data sets correspond to circular, triangular, and x data points, respectively.

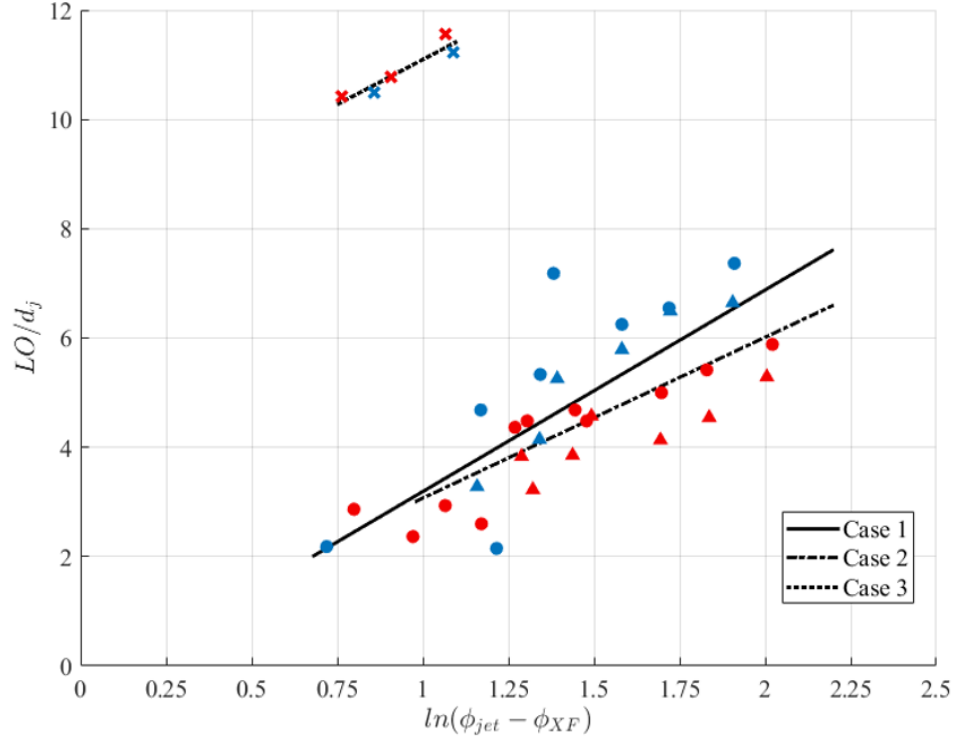


Figure 27 – Plot of selected RJICF data using analytical form suggested by Eq. 20.

Figure 27 bears out the anticipated results outlined above and helps visualize the impact of exit velocity profile and forced liftoff. Case 3 does indeed show a similar slope, which supports similar mixing rates in the two sets of pipe geometry lifted reacting jets. The significantly increased y-intercept of Case 3 compared to Case 1 results in a significantly leaner value for ϕ_{Flame} when calculated. This reduction in ϕ_{Flame} due to increased LO is in agreement with the lower normalized NOx levels measured for these test points. With regards to the exit velocity profile, Case 2 does indeed exhibit a lower slope compared to Case 1, corresponding to a smaller spatial mixing length scale and therefore faster spatial mixing rate compared to the pipe data. This is in agreement with literature [20, 22]. In addition the shift in y-intercept (with the change in ℓ_m accounted for), results in a small reduction in ϕ_{Flame} . If the preferred ϕ_{Flame} is near values associated

with peak flame temperatures (as hypothesized) this would account for reduction in NOx levels. However, if the preferred ϕ_{Flame} was significantly richer than this peak, NOx levels should increase. Although, increased post flame mixing could compensate for this to a degree. It is also important to note that when considering the confidence intervals of the respective slopes there is significant overlap. At this point, therefore, it is still not possible to pinpoint the relative impact of exit velocity profile on pre-flame and post-flame RJICF mixing.

4.4 Summary of Chapter Findings

The work presented in this chapter investigates the sensitivities of RJICF NOx production of premixed mixtures of ethane and air as well as ethane, methane, and air. The jets were injected in a vitiated crossflow at various temperatures and were characterized by a broad parameter space with regards to J and ϕ_{jet} .

The data further reinforces the findings from CHAPTER 3 that significant NOx variation is possible at constant ΔT . As in CHAPTER 3, this finding addresses the second central research question of this thesis, whether other parameters could influence NOx on the same order of ΔT . Between the data presented in these two chapters it is clear that it can.

The data also directly addressed the first research question regarding the governing parameters of NOx production in a RJICF. The data established three regimes of flame stabilization behavior largely dependent on ϕ_{jet} : a range of lee-stabilization, a fully lifted regime at higher ϕ_{jet} values, and a fully lifted regime at lower ϕ_{jet} values. NOx emissions normalized by a ΔT surrogate were shown to collapse into one of three behaviors. One of

these solutions was associated with negligible NOx production and was comprised of the data that exhibited the fully lifted behavior at values of ϕ_{jet} below the range of lee-stabilization. The second behavior was associated with lee-stabilized flames and exhibited a dependence on ϕ_{jet} . The final solution was associated with high NOx production and comprised of the very rich fully lifted jets. In both the first and final solutions the NOx level was not sensitive to either the LO or ϕ_{jet} . Forced flame lifting via the use of an ethane/methane mixture in place of pure ethane at constant ϕ_{jet} demonstrated that significant reduction in NOx could be achieved with an increase in LO . The exit velocity profile was varied by using either pipe or nozzle jet injection hardware to induce variation in SLV growth rates and thereby JICF mixing rates. The nozzle geometry demonstrated a reduction in LO and NOx compared to the pipe geometries in cases where the flame stabilization behavior did not change.

With regards to the third central research questions regarding the governing physics, this chapter discussed the hypothesis that ϕ_{jet} , LO , and mixing rates control the local equivalence ratio of the combustor mixture, ϕ_{Flame} , and that ϕ_{Flame} is a governing first order parameter for NOx production in RJICF. It was further hypothesized that the flow configuration had a range of ϕ_{Flame} values at which flames could be lee-stabilized and a roughly constant ϕ_{Flame} value at which it became fully “rich lifted”. This hypothesis was further explored via a mixing model that proposes ϕ_{Flame} as function of ϕ_{jet} , LO , and mixing rates. This model was in agreement with the sensitivities observed in the data, providing additional support for the hypothesized relationships.

Several questions remain. First, while the data is consistent with the idea that ϕ_{Flame} controls NOx emissions, there are also indications that post-flame mixing has an influence.



This was suggested by the results in Figure 26 for the lee-stabilized results. Given that pre-flame and post-flame mixing are inherently coupled, more work is needed to clarify their relative roles. CHAPTER 5 will present work aimed at validating these hypotheses around ϕ_{Flame} . In particular CHAPTER 5 determines actual mixture fraction values of the flame and relate these findings to NO production rates based on ϕ_{Flame} effects. These production rates are compared to the measured NOx emissions and correlated to the governing parameters identified in this chapter.

CHAPTER 5. IMPACT OF PREFLAME MIXING ON EQUIVALENCE RATIO OF COMBUSTION

The overall objective of this chapter is to evaluate the extent to which NO_x emissions can be correlated with averaged pre-flame mixing levels. As such, these results are organized into three parts. The first qualitatively discusses the instantaneous mixture fraction fields to assess any evident differences between RJICF with different parameters and then how these differences manifest in the time averaged mixture fraction field. The interaction between the expected mixture fraction field and flame position is also discussed. The second part examines the time averaged pre-flame mixing rates of these flows. The third part compares NO production rates calculated based on the presented data with NO_x emissions measurements previously presented in CHAPTER 4.

In each instance, the data associated with the nozzle exit geometry and $J \leq 20$ is used as a reference point to explore the impact of the various RJICF parameters. For the sake of consistency, the data is denoted via the scheme presented in Table 4 throughout all subsequent figures. Circular points are used for the pipe exit geometry data, triangles for the nozzle exit geometry data, hollow points are used to denote data with $J = 40$, and x's and +'s are used for the forced lifting points via methane doping for pipe and nozzle geometries. In addition all points have a color corresponding to their crossflow condition, with blue for $\phi_{XF} = 0.45$ and red for $\phi_{XF} = 0.50$.

Table 4 – Symbol legend for CHAPTER 5 figures.

▲	Data from nozzle exit geometry
△	Data from nozzle exit geometry with $J = 40$
+	Data from doped nozzle exit geometry
●	Data from pipe exit geometry
*	Data from doped pipe exit geometry
	$\phi_{XF} = 0.45$
	$\phi_{XF} = 0.50$

As a final note, the data presented herein is a subset of the parameter space described in Section 2.2.2. The data presented is that which was of sufficient quality to be successfully processed by the method described in Section 2.4.2. Some data points were unusable due to overabundance of reflections and/or poor seeding densities.

5.1 Mixture Fraction Fields and Flame Position of Premixed Jets

This section presents illustrative results for mixture fraction fields and flame position statistics. Figure 28 shows three consecutive instantaneous mixture fraction fields for three jet conditions. The time sequence is shown from left to right in the figure. The various jet conditions presented have the following parameters from top to bottom: $J = 8$ with nozzle geometry, $J = 15$ with nozzle geometry, and $J = 15$ with pipe geometry. For clarity, these images do not have near flame values discarded. However, in these instances the flame is located in a position that does not impact the following discussion of the figure. Evident in Figure 28 is the well-formed shear layer vortices in the nozzle geometry cases, especially in comparison to the pipe case. The higher J cases present with observably higher jet penetration transversely into the crossflow. While it is difficult to see a difference in trajectory between the nozzle and pipe geometries in these cases, it is apparent that the jet

fluid maintains more coherency than in the nozzle case which appears to more effectively disperse the jet fluid.

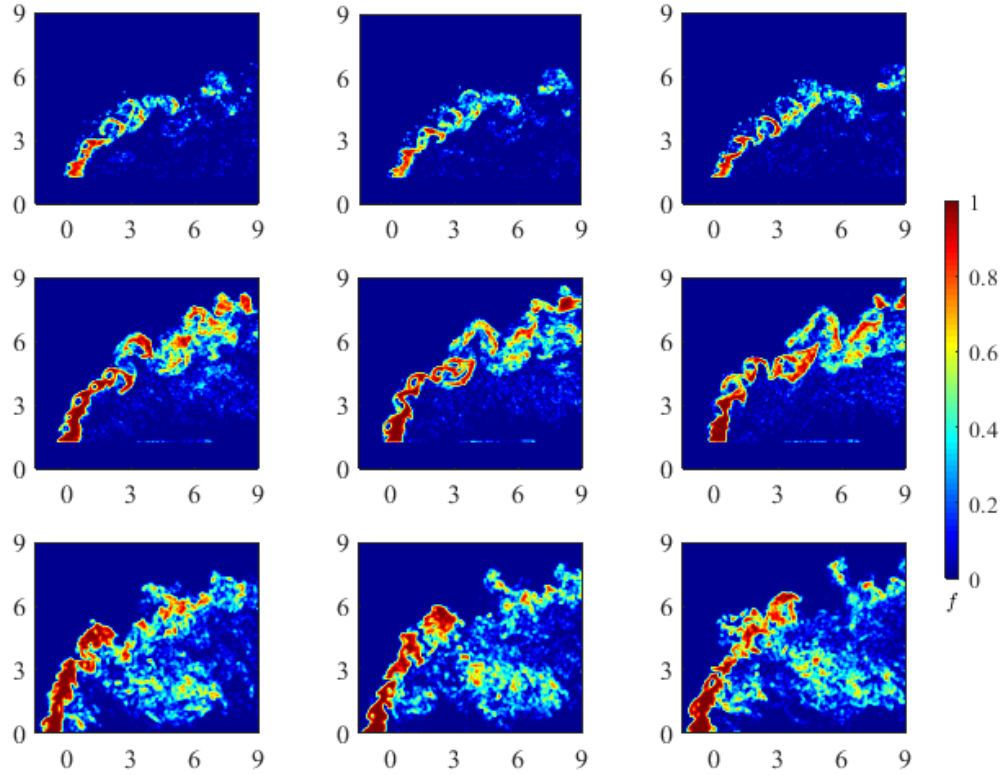


Figure 28 – Sequence of three successive instantaneous mixture fraction fields (left to right) for three reacting jets (top to bottom). The jets have the following parameters: $J = 8$ with nozzle geometry (top), $J = 15$ with nozzle geometry (middle), and $J = 15$ with pipe geometry (bottom). Axis are coordinates normalize by d_j .

Figure 29 shows the averaged mixture fraction fields for the three RJICF whose instantaneous images were presented above. As discussed the values are conditioned based on flame position and points with less than 100 samples are discarded (area shown in grey on image).⁸ Also plotted are mean concentration centerline trajectories. The jet trajectory

⁸ The flame associated with the field shown in the right pane of Figure 29 was highly lifted and not-steady in position, resulting in all locations with > 100 samples.

was determined using a power law fit of the loci of maximum f values in a manner similar to Gevorkyan *et al.* [20]. In the time-averaged fields the higher transverse jet penetration with increased J is clearly evident, as is an increase in the length of the jet core. Comparing the left and right panes of Figure 29, corresponding to the nozzle and pipe geometries, it is observable that the jet fluid persists in higher mixture fractions further along the jet trajectory, indicating reduced pre-flame mixing in comparison to the nozzle exit geometry.

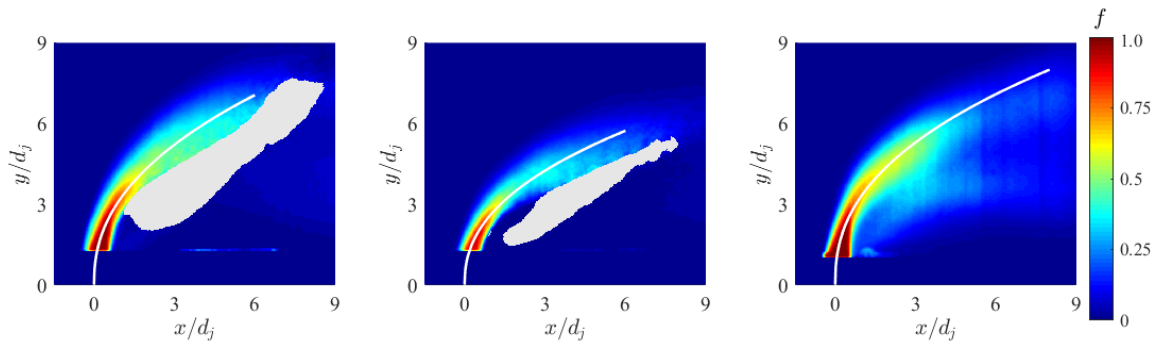


Figure 29 – Time average mixture fraction fields for three reacting jets. The jets have the following parameters: $J = 15$ with nozzle geometry (left), $J = 8$ with nozzle geometry (middle), and $J = 15$ with pipe geometry (right).

The discussion in Section 4.1 identified three regimes of flame behavior that were associated with different NO_x emissions behaviors. Figure 30 shows expected mixture fraction fields for a characteristic data point for each of the three flame behaviors: “lean lifted”, lee-stabilized, and “rich lifted.” Overlaid onto the mixture fractions maps is the stoichiometric mixture fraction contour shown in white and an instantaneous flame edge in magenta. The J value for all three jets are identical. These images provide significant insight into the flame stabilization behavior of each of these flames.

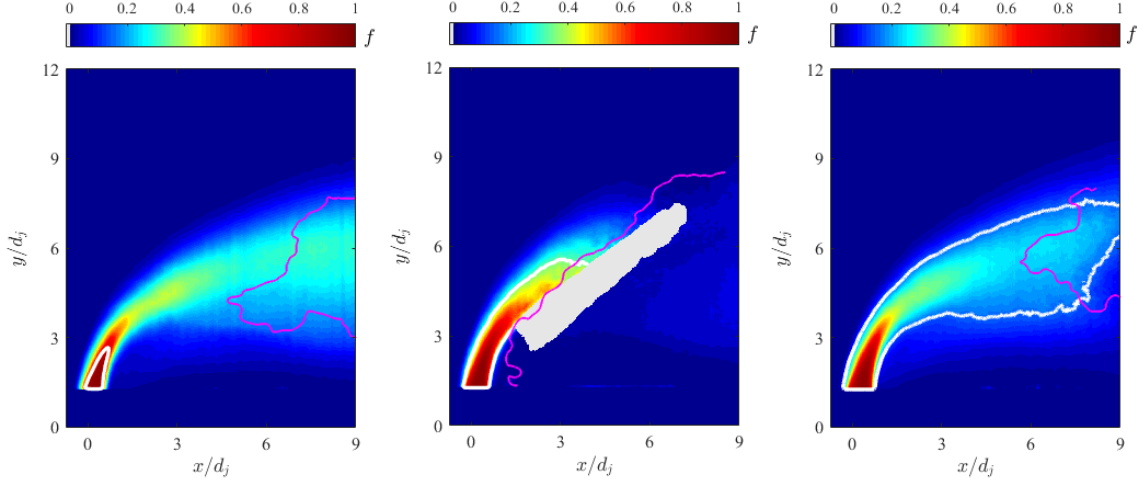


Figure 30 – Instantaneous flame position superimposed onto expected mixture fraction fields for a “lean lifted” (left), lee-stabilized (center), and “rich lifted” (right) flame.

For the “lean lifted” case, in the left pane of Figure 30, the flame sits well away from the stoichiometric contour and roughly centered on the scalar centerline. The lee-stabilized case, in the center pane of Figure 30, displays a lean flamebase situated in the lee of the RJICF that serves as an anchor for a flame angling into and across the jet trajectory. This is most likely a premixed flame propagating into the jet fluid reactants that is anchored by the lean flamebase in the wake of the jet. This is congruent with the findings of Schulz and Noiray [30] who identified that attached RJICF flames initiate in regions corresponding to the most reactive mixture fraction, which is very lean in this configuration due to the temperature discrepancy between the jet and crossflow. Finally, the “rich lifted” case, in the right pane of Figure 30, shows that the flamebase/front configuration has been shifted downstream. The presence of a stabilizing flame base is still interpreted, as is a front propagating into the reactant steam. However, the richness of the jet has forced the flame to situate itself further downstream in order that the propagating flame meets a flammable

mixture. These observations support the hypothesis presented in CHAPTER 4 with regards to the different flame behaviors.

In addition, Figure 30 clearly indicates that the flame spans a wide range of mixture fractions and thus equivalence ratios of combustion, ϕ_{Flame} . This variation will induce a large variation in the adiabatic flame temperature along the flame edge and consequently significant variation in NOx production rates in the post-flame region directly behind the edge. This highlights the need to utilize an estimated NO production rate, to assess the consequence of ϕ_{Flame} , in order to properly weight the variation in flame temperature (T_{Flame}) and local availability of oxygen and nitrogen.

5.2 Pre-flame Mixing Length Scales of Premixed Jets

As noted in Section 4.3 and evident from the images in Figure 29 and Figure 30, the pre-flame mixing rates, expressed through the decay of the centerline concentration, are themselves functions of J , exit velocity profile, and flame position [20, 22, 34]. In this section, we define and characterize representative mixing lengths enabling us to reduce the spatial mixing fields.

From the concentration jet trajectories, the evolution of the centerline concentration can be extracted. Figure 31 plots three examples of the decay of the centerline mixture fraction as a function of distance along the trajectory (s_c). The three cases correspond to those presented in Figure 28 and Figure 29. Also plotted are reference power law decay rates for centerline decay rates from literature[19-21]. The scalar potential core is clearly evident in Figure 31, persisting to approximately $s_c/d_j = 2.0 - 2.5$; indicating a relationship between the potential core length and J , congruent with Gevorkyan *et al* [20]. In addition,

the decay of the mixture fraction field is also clearly apparent, as is a disparity between the rate of decay for the nozzle and pipe cases. From these results, two distinct length scales are evident, associated with the potential core length (ℓ_{core}) and the decay length scale (ℓ_{decay}). The two length scales are defined as the s_c/d_j value require to reach mixture fractions of 0.975 and 0.6 respectively.⁹

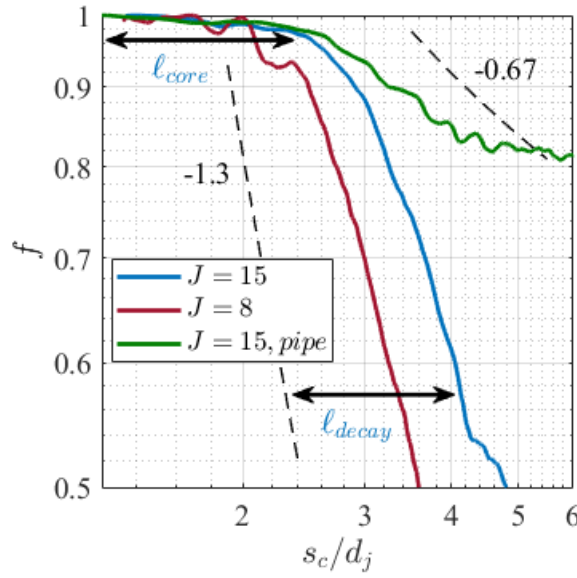


Figure 31 – Mixture fraction values as a function of distance along jet scalar trajectory for three reacting jets: $J = 15$ with nozzle geometry (blue), $J = 8$ with nozzle geometry (red), and $J = 15$ with pipe geometry (green).

Figure 32 plots ℓ_{core} and ℓ_{decay} as a function of J , with the data indicated per Table 4. For ℓ_{core} , a strong correlation between the potential core length and J is again apparent. This is agreement with Gevorkyan *et al* [20], who presented similar results. This agreement with literature helps alleviate concerns associated with particle overlap as discussed in Section 2.4.2. The dependence of ℓ_{core} on J is in large part due to the impact of the jet exit

⁹ The 0.6 threshold was selected based on the limit of the centerline concentration decay for the pipe cases along the fitted trajectory, which is finite in length.

velocity (which J is directly related to since the crossflow velocity is held constant) on how long the jet potential core persists. Gevorkyan *et al* [20] also showed that the decay rates post core had little correlation to J and could be more varied. This trend is also evident in Figure 32 when examining ℓ_{decay} .

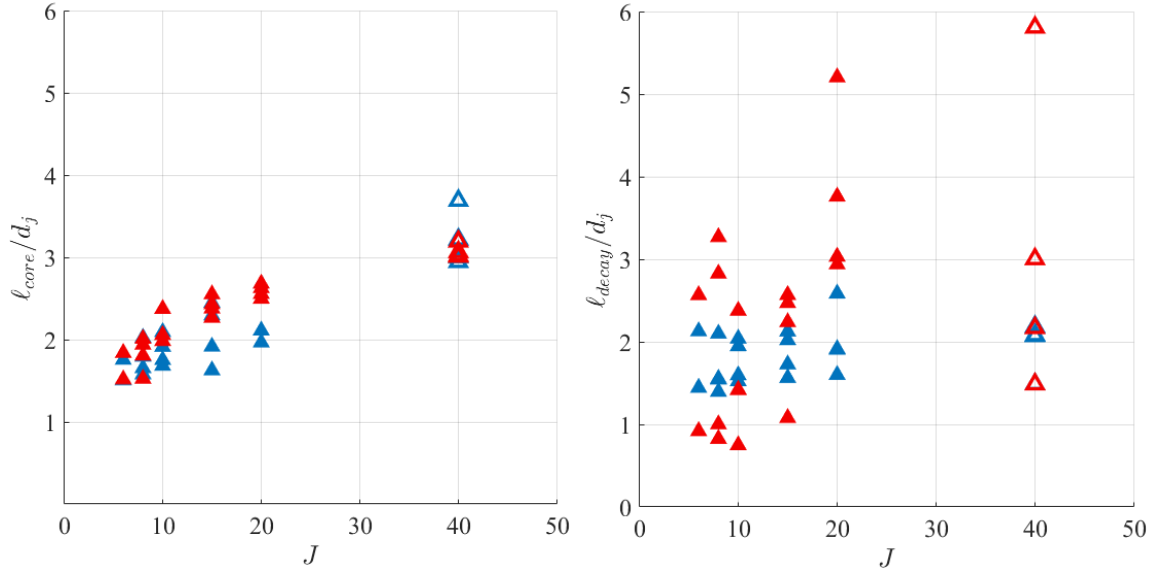


Figure 32 – Potential core (left) and decay rate (right) length scales as a function of J for reacting jets with nozzle geometries at constant crossflow conditions of $\phi_{XF} = 0.45$ and $\phi_{XF} = 0.50$.

Considering the impact of flame position next, it was noted in Section 1.3.2 that Nair *et al* [34] observed a suppression of SLV growth in RJICF cases where the flame was in close proximity to the jet exit. As a result, a dependency of ℓ_{core} or ℓ_{decay} on whether a flame was lee-stabilized or fully lifted would be expected. However, no significant correlation was observed. The previously noted trends remained dominant. This result is unexpected as Nair *et al* [34] observed the suppression of SLV growth in RJICFs with the flame in close proximity of the jet exit. However a significant difference between that work and the data presented here is that Nair *et al* [34] analyzed jets that were primarily fully

attached as opposed to lee-stabilized. In fact, Nair *et al* [34] notes a reduction in the strength of the suppression when the windward edge begins to lift. This finding sparks the need for further work to identify what the impact of a lee-stabilized flame is on the JICF vorticity field.

Finally the impact of exit velocity profile is considered. In this instance, $\ell_m \equiv \ell_{core} + \ell_{decay}$ will be used as a metric to assess the disparity in pre-flame mixing rates between the different exit velocity profiles. Figure 33 plots the mixing length scales for both nozzle and pipe exit geometry test cases as a function of J (similar to Figure 32).

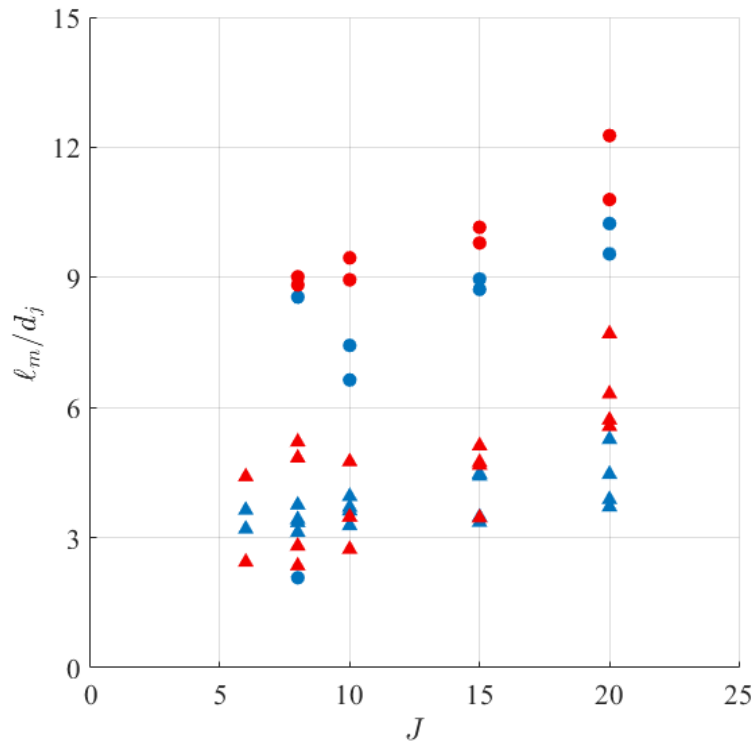


Figure 33 - Pre-flame mixing length scales as a function of J for reacting jets with both nozzle and pipe exit geometries at constant crossflow conditions of $\phi_{XF} = 0.45$ and $\phi_{XF} = 0.50$.

The pipe data has significantly higher ℓ_m values than those associated with the nozzle geometry, on the order of 2x. This finding is congruent with the observation of New *et al*

[22], reviewed in the Introduction, that higher SLV growth rates can be found in jets with nozzle geometries compared to the fully developed pipe. This further supports importance of SLV growth rates in pre-flame mixing.

5.3 Comparison of NO Production Rates to NOx Emissions for Premixed Jets

This section assess whether time-averaged pre-flame mixing considerations can accurately capture NOx emissions levels in RJICF. This is assessed via NO production rates calculated from time-averaged mixture fraction fields and equilibrium considerations as described in Section 2.4.3. The calculated NO production rates are compared to measured NOx emissions taken under identical test conditions. The NOx emissions data and its parametric sensitivities were discussed in CHAPTER 4. This section begins its analysis by focusing on two key functional parameters for ϕ_{Flame} hypothesized in Section 4.3: pre-flame mixing duration and rate. Pre-flame mixing duration is investigated via the comparison of the undoped and doped data point pairs that generate variations in LO at fixed jet parameters as described in Section 2.2.2. Pre-flame mixing rate is investigated via comparison of the nozzle and pipe exit geometries as Section 5.2 confirmed the disparity in mixing rates between these cases. Finally a complete comparison of the nozzle data set with the measured NOx emissions is presented.

5.3.1 Impact of Forced Liftoff on NO Production Rates for Premixed Jets

The results presented in Section 4.2.3 indicated a strong correlation between NOx reduction and LO in cases where ϕ_{jet} was constant, mainly through forcing increased LO via the doping of the ethane fuel with methane at constant ϕ_{jet} . Figure 34 shows the change in NOx against the change in $d[NO]/dt$ due to the fuel stream doping. The change is

indicated as percentage of the undoped value. Data with both with nozzle and pipe geometries are plotted, denoted as per Table 4, with the uncertainty indicated by error bars.¹⁰

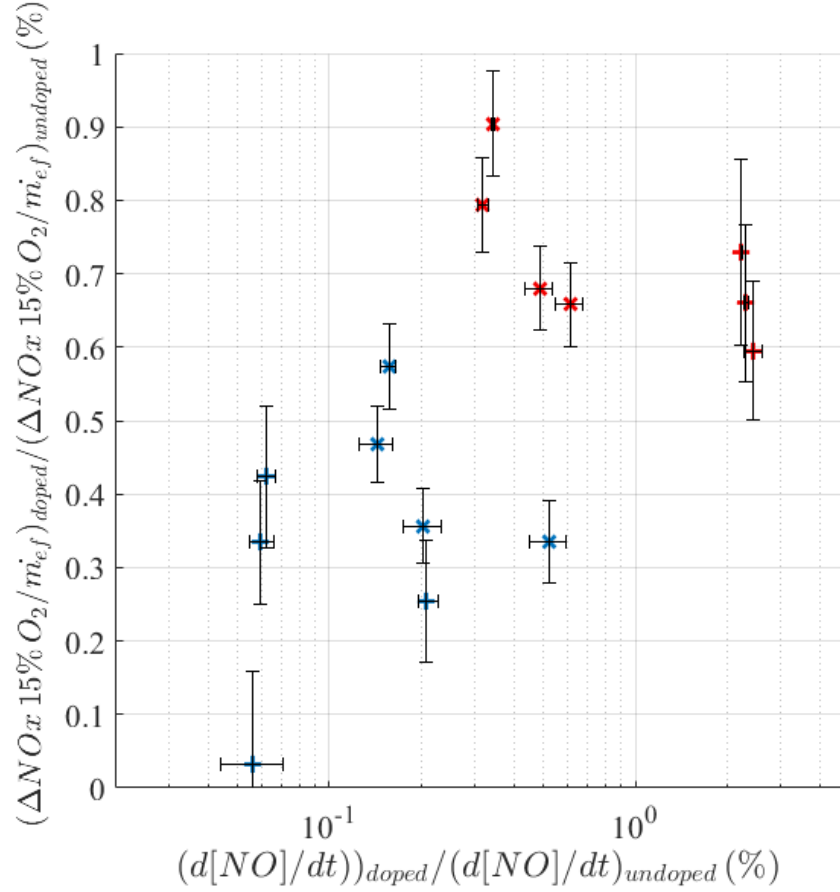


Figure 34 - Change in NOx with change in thermal NO production rates for doped data pairs for reacting jets with nozzle and pipe geometries at constant crossflow conditions of $\phi_{XF} = 0.45$ and $\phi_{XF} = 0.50$.

The discussion presented in Section 5.2 indicated a lack of significant variation in mixing length scale with LO . Therefore, it is anticipated that the major driver for the NOx reduction associated with forced liftoff is due to the manipulation of ϕ_{Flame} . For the majority

¹⁰ The contributions to the uncertainty in NO production rate are the variance of mixture fraction at a given location determined by the mixture fraction variance field and the variance in flame location.

of data, Figure 34 indicates reductions in NO_x corresponding to reductions in $d[NO]/dt$ for the majority of the data as expected. However, several test points experienced an increase in NO production rate but were still observed with a significant NO_x reduction. These observations indicate other significant factors at play. While the near field mixing data (Section 5.2) indicates that flame position does not have a large impact on SLV growth rate in these lee-stabilized and fully lifted premixed RJICF, the data presented in Figure 34 shows that the far field mixing in the form of the CVP might be impacted due to NO_x reduction despite elevated NO production rates. It also suggests that post-flame dilution rates are an equal order parameter of significance compared to ϕ_{Flame} . This spurs another need for further work: to characterize the impact of parameter variation on the far field mixing rate, potentially in the form of CVP strength and size.

As for why certain points experienced a rise in NO production rates with increased LO: these points correspond to data that was lee-stabilized near the rich end of the stabilization range. It is likely that they transitioned into a “rich lifted” modality when doped and not a “lean lifted” one. This would create a situation with similar T_{Flame} but increased [O].

5.3.2 *Impact of Exit Velocity Profile on NO Production Rates of Premixed Jets*

Consider now the impact of varying jet exit velocity profile. Section 4.2.4 indicated a reduction in NO_x data with the nozzle exit velocity profile compared to the pipe. Due to the nature of the relationship, it was however unclear whether the higher SLV growth found in JICF with nozzle geometries compared to pipe geometries, as observed by New *et al* [22], generated a reduction ϕ_{Flame} or an enhancement of post-flame dilution rates (or both).

Figure 35 plots the change in NOx emissions due to the change in exit velocity profile to a fully developed profile as a percentage of the corresponding normalized emission from the top hat profile case. This change is plotted as a function of the percentage change in $d[NO]/dt$ due to the change in exit velocity profile. A dashed line indicating a 1:1 correlation is also shown for reference.

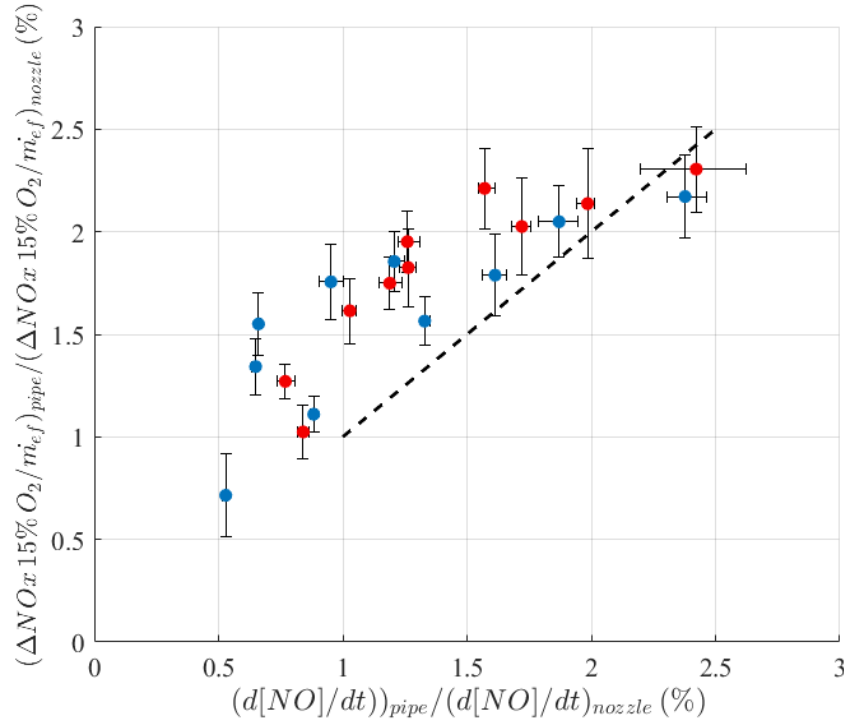


Figure 35 – Fraction of NOx production from reacting jets with pipe geometry compared to reacting jets with nozzle geometry as a function of the associated percentage change in NO production rate.

From the data in Figure 35 it is apparent that the pipe geometry results in higher NOx emissions compared to the nozzle cases. In addition this increase in NOx correlates with increases in NO production rates, supporting the hypothesis that the increased SLV growth rates, and reduced mixing length scales, induce a reduction in ϕ_{Flame} . However, several cases experience little increase in production rate or even a decrease in production rates but still observe and increase in NOx emissions. This suggests that the nozzle geometry is

indeed inducing high post-flame dilution rates and that ϕ_{Flame} reduction only accounts for a portion of the observed NOx reduction.

5.3.3 *Correlation of NOx Emissions to NO Production Rates for Premixed Jets*

The key hypothesis that this chapter seeks to test is whether NOx emissions are dominated by average pre-flame mixing rates. To this end, Figure 36 plots the NOx emissions of reacting jets for the investigated parameter space utilizing the nozzle geometry as a function of an effective NO production rate based on Equation 16. The NOx emissions are normalized by the effective fuel mass flowrate of the jet (\dot{m}_{ef}) as in CHAPTER 4, and the NO production rate is an average rate across all locations of all instantaneous flame edges for a given data point. The data is indicated per Table 4. In addition the associated uncertainty in the NOx measurement and the uncertainty in the NO production rate are indicated with error bars.

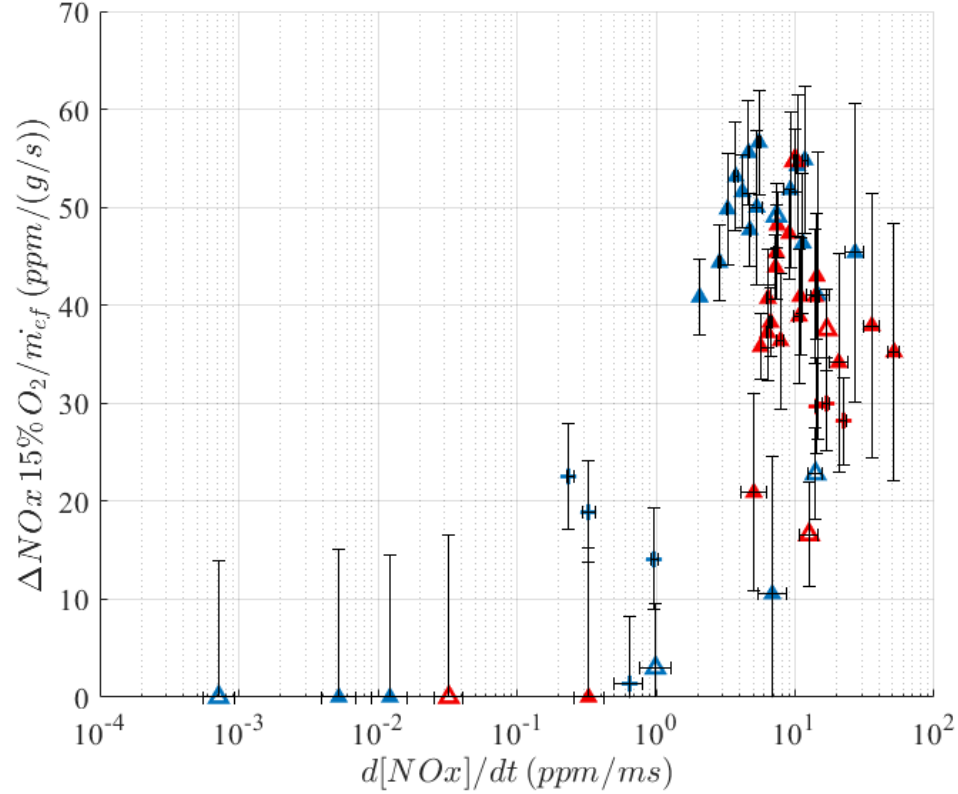


Figure 36 – Normalized RJICF NOx production as a function of estimated thermal NO production rates for all nozzle geometry data at constant crossflow conditions of $\phi_{XF} = 0.45$ and $\phi_{XF} = 0.50$.

Several key observations can be made from Figure 36. First, there is a clear relationship between the reacting jet NOx emissions and the thermal NO production rate, strongly supporting the hypothesis that the initial temperature determined by ϕ_{Flame} is a key driver of NOx production. Second, there appears to be a threshold below which NOx becomes negligible. It is possible that this cutoff is due to the sensitivity of the gas analyzer and that given a more precise means of measuring the emissions, the trend would remain monotonic. Finally, when focusing on the unforced cases (undoped and $J \leq 20$) the production rates tend to cluster either below the threshold for detected emissions or at high production rates of roughly equal value that is associated with the whole range of high NOx emissions data. This indicates that time averaged ϕ_{Flame} considerations are capable of

distinguishing whether a low or high NO_x situation will result from the RJICF, but is not sufficient to accurately predict the NO_x emissions in cases where these levels are high.

Several potential sources exist for the lack of correlation between the calculated NO production rates and the NO_x emissions within the high NO_x region of the parameter space. First, the underlying assumptions in f calculations might be overly restrictive. Second, reactant mass fluxes / consumption rates most likely vary across the flame edge. This would impact how different portions of the flame contribute to the averaged NO production rate. Third, is that instantaneous variation is significant and intermittency in NO production rates can be significant. Finally, as identified in Sections 5.3.1 and 5.3.2 it is likely that the sensitivity to post-flame dilution rate remains significant in comparison to the sensitivity to ϕ_{Flame} . In summary, while time averaged ϕ_{Flame} considerations are certainly a key parameter in RJICF production other effects (most likely post-flame dilution rates, or internal intermittency of NO production) are significant as well.

5.4 Summary of Chapter Findings

The work presented in this chapter investigates the relationship between RJICF NO_x emissions and thermal NO production rates based off of equilibrium flame temperatures and atomic oxygen concentrations. The aim was to establish whether time averaged flame conditions were the primary governing parameter over thermal NO_x production in these reacting jets in support of the hypothesis presented in Section 4.3, and to address the third key research question of the thesis. The jets consisted of premixed mixtures of ethane and air as well as ethane, methane, and air. The jets were injected in a vitiated crossflow at

various temperatures and were characterized by a broad parameter space with regards to J and ϕ_{jet} .

In addressing the underlying physical phenomena governing NOx production, the data established NO production rate, and by extension ϕ_{Flame} , as a first order governing parameter for RJICF NOx emissions. The sensitivity of the production rates on flame stabilization behavior and exit velocity profile was investigated. NO production rates were shown to rise rapidly as T_{Flame} increased due to jet stoichiometry or flame position, and then decline for flames in rich regions of the flow due to the shortage of atomic oxygen. ϕ_{Flame} was previously hypothesized to be reduced with increased liftoff at fixed ϕ_{jet} , leading to reduced production rates. While this was shown to be predominately true, cases existed where this actually increased production rates most likely due to an increase in [O]. Similarly, NOx production rates were shown to predominately increase with a transition in exit velocity profile from top hat to fully developed boundary layers, but cases where production rates decreased were observed despite still resulting in increased NOx emissions. This indicates other factors at work in the change of exit velocity profile.

All of the observations discussed indicate that other factors, most likely post-flame dilution rates, intermittency of NO product rates, or variable local consumptions rates, have significant impacts on NOx in addition relation ϕ_{Flame} . Further work is needed to investigate the impact and sensitivities of post-flame dilution rates in order to validate these hypotheses. In particular it is necessary to determine how post-flame dilution rates are impacted by exit velocity profile, flame position and J . A more thorough discussion of needed work is presented in Section 6.2.

CHAPTER 6. CONCLUSIONS AND RECOMMENDATIONS

The work presented in this thesis was motivated by the challenge of achieving low nitrogen oxide emissions in high temperature combustion devices that are required to operate over a wide range of load conditions. Specifically, this work seeks to further the understanding of pollutant formation in the complex reacting flow field created by a reacting jet in a vitiated crossflow. The interest is driven by its potential as a means to reduce NO_x at high temperature via axial staging. The primary objectives of this study were to identify the governing parameters of NO_x production in the RJICF flow field and to ascertain if any of these sensitivities are as significant as those previously identified in literature, namely ΔT . In pursuit of these objectives the NO_x emissions of a wide parameter space of premixed ethane/air, methane/air, and ethane/methane/air jets were experimentally characterized. In addition, high speed optical diagnostics were utilized to determine flame position and stabilization behavior as well as the time averaged pre-flame mixture fraction field. This final chapter summarizes the key contributions of the presented work, and provides recommendations for future work in RJICF emissions characterization.

6.1 Summary of Findings

The first major contribution of this work is to confirm the dominant role that ΔT has in RJICF NO_x production. This sensitivity had been previously identified in literature and is strongly supported by the data reported in this thesis. A clear correlation between ΔNO_x and ΔT (or $\Delta \phi$) was observed, with NO_x emissions monotonically increasing with increasing ΔT .

Expanding upon what had been previously identified in the literature, the data presented in this work also establishes that NOx production in a RJICF varies significantly at constant ΔT or similar parameter (e.g. jet fuel mass flow or $\Delta\phi$). Emissions measurements in premixed reacting jets indicated that NOx production from a RJICF varies as much as 3x at constant ΔT . This finding serves as the second major contribution of this work, and validates the need for investigation into the governing parameters and coupled physical processes involved.

The third major contribution of this work is a systematic characterization of the key sensitivities of NOx production over a wide parameter space of premixed reacting jets. The envelope of investigation included both rich and lean jet equivalence ratios as well as different regimes of jet stability behavior: globally or convectively unstable. Great attention was paid to isolating each potential driver of NOx production. When ϕ_{jet} and LO were interdependent, the reacting jets grouped themselves into three regions of flame stabilization and NOx emissions behavior. The central region, in terms of ϕ_{jet} , was occupied by lee-stabilized flames. Jets with equivalence ratios that were more fuel lean (“lean lifted”) and that were more fuel rich (“rich lifted”) than those associated with lee-stabilized flames were fully lifted. The emissions of fully lifted flames were largely invariant with ϕ_{jet} or LO , but were grouped as either producing negligible or high levels of NOx emissions. Negligible NOx production was associated with “lean lifted” flames, and high NOx production was found in the “rich lifted” cases. The lee-stabilized flames produced intermediate NOx emissions and exhibited a dependency on ϕ_{jet} that plateaued at NOx levels similar to those of the “rich lifted” flames. When LO was increased at constant ϕ_{jet} , either as a consequence of data with high momentum flux ratio or via the doping of the jet

fuel mixture with methane to retard ignition kinetics, NO_x production was shown to decrease in every instance. Finally, the impact on shear layer growth rate/near-field mixing rates was examined via the selection of exit velocity profile. Data was acquired for a fully developed jet exit boundary layer and a top hat jet exit velocity profile. The more rapid near-field mixing associated with the top hat exit profile [20, 22] was shown to produce less NO_x than the fully developed boundary layer.

The final major contribution of this work is to establish the equivalence ratio of combustion, ϕ_{Flame} , as a 1st order parameter driving NO_x production in RJICF. Based on the interdependencies observed between jet parameters, it was hypothesized that ϕ_{jet} , LO , and near-field mixing rates were functional parameters of ϕ_{Flame} , and that ϕ_{Flame} strongly correlated with NO_x production in RJICF. This hypothesis was tested by calculating NO production rates based on the impact that ϕ_{Flame} would have on flame temperature and equilibrium [O]. The local combustion conditions were determined by the overlay of instantaneous flame edges onto a time averaged mixture fraction field. The mixture fraction field was experimentally determined using Mie scattering images of ceramic particles seeded into the jet fluid stream. The investigation corroborated ϕ_{Flame} as a significant factor in RJICF NO_x production. However, in the region where ϕ_{Flame} indicated high NO production (and where the data showed high NO_x levels), there existed a significant variation in NO_x levels at near constant $d[NO]/dt$. Post-flame dilution/mixing rates, ϕ_{Flame} intermittency, and variable reactant consumption rates along the flame are all potential causes for the observed variation in NO_x.

The work indicates an avenue for NO_x mitigation in the form of fully lifted reacting jets with rapid pre-flame and post-flame mixing rates, and perhaps more significantly

underscores the necessity of this approach in achieving any kind of NO_x benefit from the implementation of axial staging via a RJICF. The prospect of achieving the described flow field is challenging and raises additional questions that need to be investigated.

6.2 Recommendations for Future Work

The work presented in this thesis provides a solid foundation for the understanding of NO_x production in a premixed RJICF and also provides direction on the most advantageous approach to utilizing a RJICF for NO_x mitigation. The realization of this from an engineering perspective is very challenging as it asks combustor designers to stabilize a lean lifted flame in a high pressure and high temperature environment. Achieving such a difficult task will require even greater understanding of the governing physical processes and how they interact. To this end two separate avenues of investigation would prove very beneficial to the pursuit of this goal.

6.2.1 Investigation of Jet Parameter Impact on Post-Flame Mixing Rates

As mentioned in Section 6.1, a key finding of the work presented in this thesis is that post-flame dilution rates might have an impact on NO_x production on the same order as ϕ_{Flame} . A central hypothesis is that the post-flame mixing is controlled by the CVP which in turn is impacted by the SLV growth rate; with the SLV growth rate a function of several parameters such as exit velocity profile, J , and flame position.

A follow-on investigation similar to that conducted to examine the local mixture fraction of combustion could be conducted with the aim of evaluating the impact of the varying jet parameters on the CVP strength and correlating that change with the measured

NO_x emissions. To be more specific, repeat the test parameter space described in Section 2.2.2 with the primary measurement being stereo-PIV of one or more transverse planes downstream of the jet exit where the CVP would be situated. Due to the CVP existing as a time averaged feature the PIV could be conducted at rates from 1 Hz up to 10 kHz based on equipment availability and still achieve the measurement objectives. Flame imaging would still remain a valuable measurement to verify similar flame position and stabilization in reference to the emissions measurements. Such an investigation would not only provide insight into RJICF NO_x formation, but also on the fundamental impact of flame position on major JICF vortical structures in premixed RJICF.

6.2.2 Investigation of Flame Stabilization Physics

The necessity to lift the flame in order to enable NO_x reduction is a key finding from the work presented here. The work also identified some of the governing parameters (i.e. jet stoichiometry, near-field mixing rates, and crossflow temperature) that influenced flame lifting for the conditions and geometries that were investigated as part of the presented work. It is very clear, from those same investigations, that flame stabilization is multi-factorial and that changes in conditions such as heat flux through the test section floor, or elevated pressure could significantly alter lifting behaviour. A more comprehensive examination on the governing physics in flame stabilization of premixed reacting jets would provide valuable understanding needed to engineer the “lean lifted” flame essential for NO_x mitigation.

This work could be started with the experimental facility in its current state. A much finer parameter sweep of jet parameters and crossflow conditions with the sole objective

of investigating lifting behaviour could be undertaken and yield valuable results. Eventually however, modifications would have to be made to provide more control over factors such as wall heat flux, physical geometry, crossflow boundary layer thickness, and pressure. The implementation of high-speed laser diagnostics would be critical; especially in the form of coupled PLIF and PIV measurements to investigate the role of flow strain rates in the stabilization of the flame within the JICF flow field. Comparisons between CH₂O and OH PLIF could also provide valuable insight into stabilization mechanics. Considering the highly three-dimensional and asymmetric nature of the flow field tomographic measurements would also be of high value where possible.

Consideration of the significant impact that elevated pressure would have on flame lift off would have to be made. Practical axial staging systems will be operating in elevated pressure environments ranging from 15 – 25 atm with Reynolds numbers significantly higher than those associated with the presented work. Pressures of this magnitude would significantly accelerate kinetics, thereby reducing autoignition delays as well as impacting flame speeds. The change in these parameters will fundamentally alter how the flame stabilizes compared to the atmospheric condition. The increase in Reynolds number will alter crossflow/jet turbulent mixing as well, which will also impact flame stabilization location.

In light of the significance of pressure effects on flame stabilization it would be prudent to investigate the lifting behaviour of RJICF at elevated pressure. Such an approach will determine how the governing jet parameters and physical processes of flame stabilization identified in this and any follow-on work change under high pressure conditions.

In addition to examining the pressure dependence of flame stabilization, it would also be valuable to validate the use of alternate fuels as surrogates for methane at high pressure. Ethane for example has a significantly lower autoignition delay compared to methane. This property could be useful in simulating some of the effect of methane under pressure. If this approach could be validated for ethane or other highly kinetic hydrocarbons it would greatly enable the scalability of proposed atmospheric investigations to high pressure conditions.

Given the challenge represented in testing at elevated pressure and applying the level of diagnostic investigation discussed (both separately and especially in tandem), this is an area that is primed for the use of simulations. Large eddy simulations (LES) grounded in the data from the initial parameter sweep could provide greater control of relevant parameters without facility modifications, and enable investigation of the complex interacting physics without the need for extensive diagnostics.

In reality a combination of the two approaches will be required to further the understanding of this complex problem that has been proven as essential to successful implementation of NO_x mitigation strategies utilizing a reacting jet in crossflow.

APPENDIX A. SUPPLEMENTAL FIGURES

This appendix provides supplemental figures for various Chapters of this thesis.

Each chapter that requires supplemental figures has its own Section in this Chapter.

A.1 Supplemental Figures for CHAPTER 2

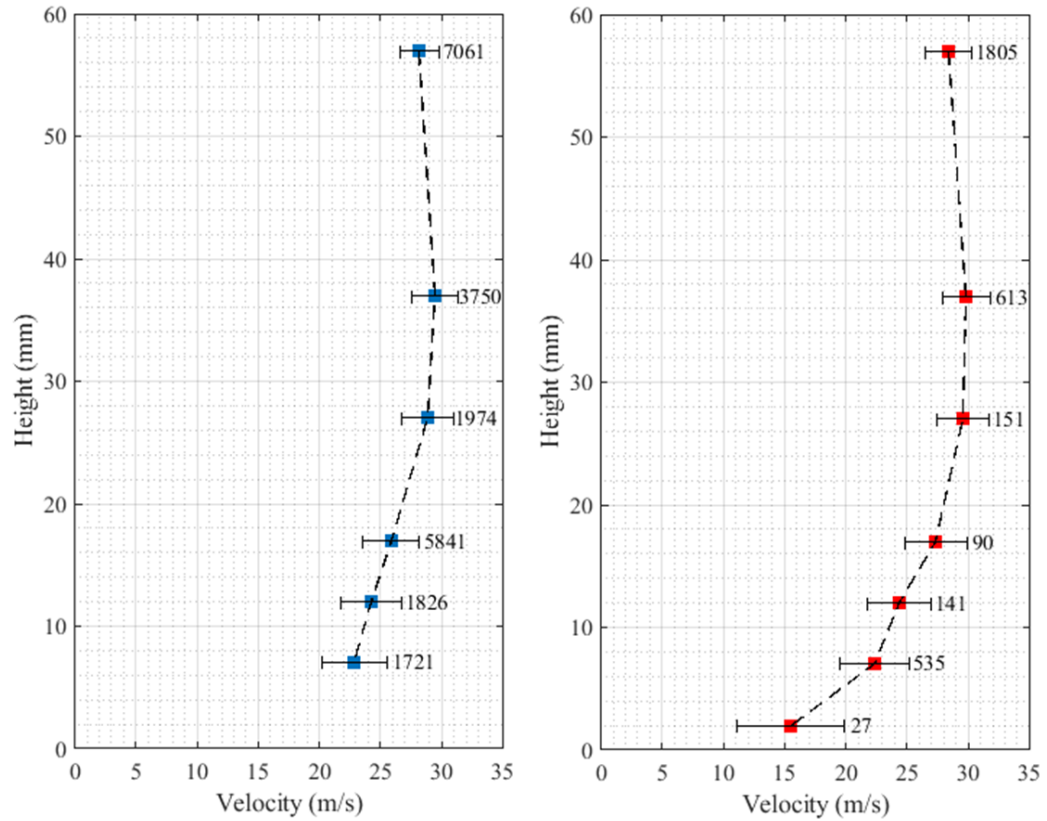


Figure 37 – Velocity profiles for vitiated crossflow with $\phi_{XF} = 0.45$ (left) and $\phi_{XF} = 0.50$ (right). Error bars indicate 99% confidence intervals and data counts for each point are displayed to the right of the error bars.

A.2 Supplemental Figures for CHAPTER 4

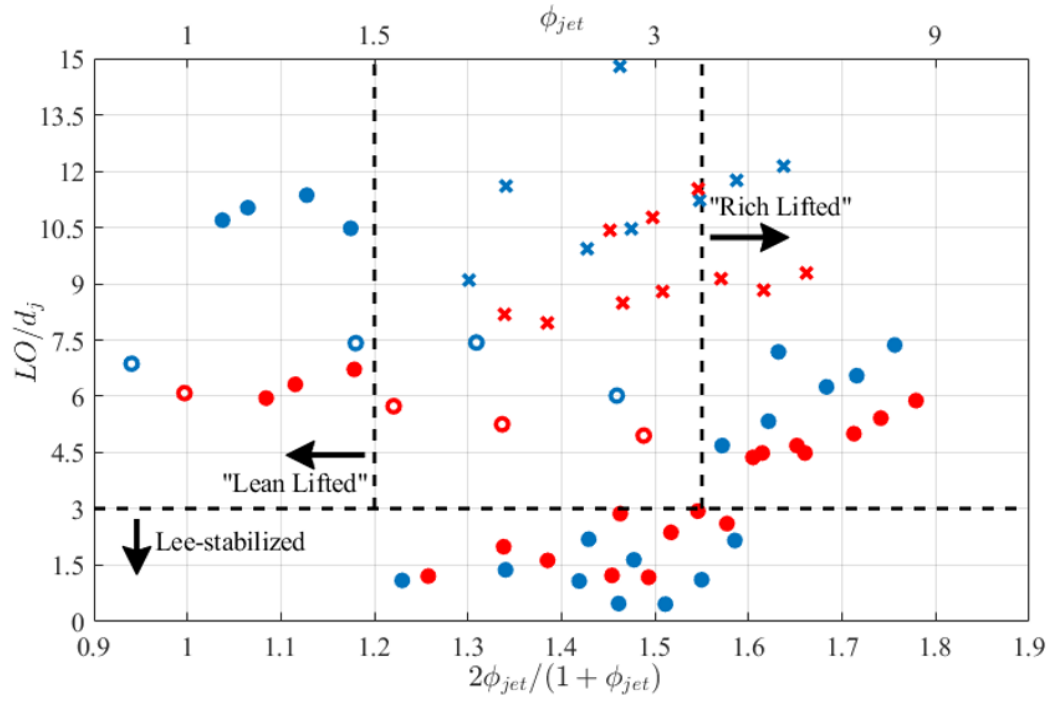


Figure 38 – Lift-off distance for all jets with pipe exit geometry (including $J = 40$ and methane doped) as a function of reduced equivalence ratio at constant crossflow conditions of $\phi_{XF} = 0.45$ and $\phi_{XF} = 0.50$.

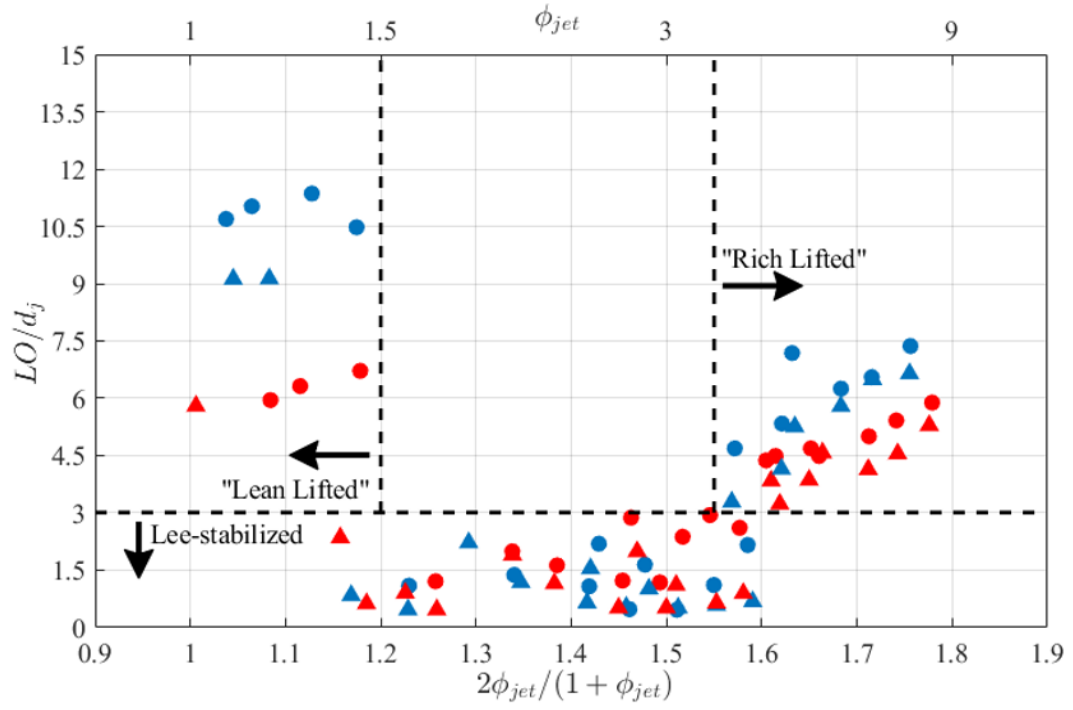


Figure 39 – Lift-off distance for jets with $J \leq 20$ as a function of reduced equivalence ratio for both pipe and nozzle jet geometries at constant crossflow conditions of $\phi_{XF} = 0.45$ and $\phi_{XF} = 0.50$.

REFERENCES

- [1] <https://www.eia.gov>. *Electricity Explained: Electricity in the United States*.
- [2] T. Lieuwen, M. Chang, and A. Amato, "Stationary gas turbine combustion: Technology needs and policy considerations," *Combustion and Flame*, vol. 160, no. 8, pp. 1311-1314, 2013.
- [3] M. Klein, "Overview of Worldwide Ground-Based Regulatory Framework," in *Gas Turbine Emissions*, T. C. Lieuwen and V. Yang, Eds. (Cambridge Aerospace Series, Cambridge: Cambridge University Press, 2013, pp. 95-120.
- [4] A. M. Dean and J. W. Bozelli, "Combustion Chemistry of Nitrogen," in *Gas-Phase Combustion Chemistry*, W. C. Gardiner, Ed. New York: Springer-Verlag, 2000, pp. 125-341.
- [5] P. Gokulakrishnan and M. S. Klassen, "NO_x and CO Formation and Control," in *Gas Turbine Emissions*, T. C. Lieuwen and V. Yang, Eds. Cambridge: Cambridge University Press, 2013, pp. 175 - 208.
- [6] C. T. Bowman, "Control of combustion-generated nitrogen oxide emissions: technology driven by regulation," *Symposium (International) on Combustion*, vol. 24, no. 1, pp. 859-878, 1992.
- [7] R. K. Hanson and S. Salimian, "Survey of Rate Constants in the N/H/O System," in *Combustion Chemistry*, W. C. Gardiner, Ed. New York, NY: Springer New York, 1984, pp. 361-421.
- [8] R. M. Kelso, T. T. Lim, and A. E. Perry, "An experimental study of round jets in cross-flow," *Journal of Fluid Mechanics*, vol. 306, pp. 111-144, 1996.
- [9] S. M. Martin, W. R. Laster, and J. E. P. Bilbao, "Axial stage combustion system with exhaust gas recirculation," 2017.
- [10] P. J. Stuttaford, P. Economo, S. Jorgensen, D. Gauthier, and T. Hui, "Axially staged gas turbine combustor with interstage premixer," 2017.
- [11] A. Amato, J. Seitzman, and T. Lieuwen, "Emissions from oxyfueled or high-exhaust gas recirculation turbines," in *Gas Turbine Emissions*, T. C. Lieuwen and V. Yang, Eds. Cambridge: Cambridge University Press, 2013, pp. 209-234.
- [12] E. Goh *et al.*, "Prediction of minimum achievable NO_x levels for fuel-staged combustors," *Combustion and Flame*, vol. 200, pp. 276-285, 2019/02/01/ 2019.

- [13] D. Ahrens, M. Kolb, C. Hirsch, and T. Sattelmayer, "NO_x Formation in a Reacting Premixed Jet in Hot Cross Flow," in *Turbo Expo*, Düsseldorf, Germany, 2014, no. 45691, p. 26139, Volume 4B: Combustion, Fuels and Emissions: ASME.
- [14] E. Goh, M. Sirignano, V. Nair, B. Emerson, T. Lieuwen, and J. Seitzman, "Modeling of Minimum NO_x in Staged-Combustion Architectures at Elevated Temperatures," in *Turbo Expo*, Charlotte, NC, USA, 2017, no. 50848, p. 63787, Volume 4A: Combustion, Fuels and Emissions: ASME.
- [15] R. G. McKinney and J. B. Hoke, "Aero Gas Turbine Combustion: Metrics, Constraints, and Systems Interactions," in *Gas Turbine Emissions*, T. C. Lieuwen and V. Yang, Eds. (Cambridge Aerospace Series, Cambridge: Cambridge University Press, 2013, pp. 3-23.
- [16] A. R. Karagozian, "Transverse jets and their control," *Progress in Energy and Combustion Science*, vol. 36, no. 5, pp. 531-553, 2010.
- [17] T. F. Fric and A. Roshko, "Vortical structure in the wake of a transverse jet," *Journal of Fluid Mechanics*, vol. 279, pp. 1-47, 1994.
- [18] T. H. New, T. T. Lim, and S. C. Luo, "Elliptic jets in cross-flow," *Journal of Fluid Mechanics*, vol. 494, pp. 119-140, 2003.
- [19] S. H. Smith and M. G. Mungal, "Mixing, structure and scaling of the jet in crossflow," *Journal of Fluid Mechanics*, vol. 357, pp. 83-122, 1998.
- [20] L. Gevorkyan, T. Shoji, D. R. Getsinger, O. I. Smith, and A. R. Karagozian, "Transverse jet mixing characteristics," *Journal of Fluid Mechanics*, vol. 790, pp. 237-274, 2016.
- [21] L. K. Su and M. G. Mungal, "Simultaneous measurements of scalar and velocity field evolution in turbulent crossflowing jets," *Journal of Fluid Mechanics*, vol. 513, pp. 1-45, 2004.
- [22] T. H. New, T. T. Lim, and S. C. Luo, "Effects of jet velocity profiles on a round jet in cross-flow," *Experiments in Fluids*, journal article vol. 40, no. 6, pp. 859-875, June 01 2006.
- [23] A. M. Steinberg, R. Sadanandan, C. Dem, P. Kutne, and W. Meier, "Structure and stabilization of hydrogen jet flames in cross-flows," presented at the Proceedings of the Combustion Institute, 2013.
- [24] J. A. Wagner, S. W. Grib, J. W. Dayton, M. W. Renfro, and B. M. Cetegen, "Flame stabilization analysis of a premixed reacting jet in vitiated crossflow," *Proceedings of the Combustion Institute*, vol. 36, no. 3, pp. 3763-3771, 2017/01/01/ 2017.

- [25] J. A. Wagner, S. W. Grib, M. W. Renfro, and B. M. Cetegen, "Flowfield measurements and flame stabilization of a premixed reacting jet in vitiated crossflow," *Combustion and Flame*, vol. 162, no. 10, pp. 3711-3727, 2015.
- [26] J. A. Wagner, M. W. Renfro, and B. M. Cetegen, "Premixed jet flame behavior in a hot vitiated crossflow of lean combustion products," *Combustion and Flame*, vol. 176, pp. 521-533, 2017.
- [27] D. Schmitt, M. Kolb, J. Weinzierl, C. Hirsch, and T. Sattelmayer, "Ignition and Flame Stabilization of a Premixed Jet in Hot Cross Flow," in *Turbo Expo*, San Antonio, Texas, USA, 2013, no. 55102, p. 94763, Volume 1A: Combustion, Fuels and Emissions: ASME.
- [28] E. F. Hasselbrink and M. G. Mungal, "Transverse jets and jet flames. Part 2. Velocity and OH field imaging," *Journal of Fluid Mechanics*, vol. 443, pp. 27-68, 2001.
- [29] D. Han and M. G. Mungal, "Simultaneous measurements of velocity and CH distribution. Part II: deflected jet flames," *Combustion and Flame*, vol. 133, no. 1, pp. 1-17, 2003/04/01/ 2003.
- [30] O. Schulz and N. Noiray, "Large Eddy Simulation of a Premixed Flame in Hot Vitiated Crossflow With Analytically Reduced Chemistry," *Journal of Engineering for Gas Turbines and Power*, vol. 141, no. 3, pp. 1-7, 2018.
- [31] R. Sullivan, B. Wilde, D. R. Noble, J. M. Seitzman, and T. C. Lieuwen, "Time-averaged characteristics of a reacting fuel jet in vitiated cross-flow," *Combustion and Flame*, vol. 161, no. 7, pp. 1792-1803, 2014.
- [32] T. Gautam, "Lift-off Heights and Visible Lengths of Vertical Turbulent Jet Diffusion Flames in Still Air," *Combustion Science and Technology*, vol. 41, no. 1-2, pp. 17-29, 1984/09/20 1984.
- [33] M. Kolb, D. Ahrens, C. Hirsch, and T. Sattelmayer, "A Model for Predicting the Lift-Off Height of Premixed Jets in Vitiated Cross Flow," *Journal of Engineering for Gas Turbines and Power*, vol. 138, no. 8, pp. 1-9, 2016.
- [34] V. Nair, B. Wilde, B. Emerson, and T. Lieuwen, "Shear Layer Dynamics in a Reacting Jet in Crossflow," *Proceedings of the Combustion Institute*, vol. 37, no. 4, pp. 5173-5180, 2019/01/01/ 2019.
- [35] V. Nair *et al.*, "Counter rotating vortex pair structure in a reacting jet in crossflow," *Proceedings of the Combustion Institute*, vol. 37, no. 2, pp. 1489-1496, 2019/01/01/ 2019.
- [36] R. V. Bandaru and S. R. Turns, "Turbulent jet flames in a crossflow: effects of some jet, crossflow, and pilot-flame parameters on emissions," *Combustion and Flame*, vol. 121, no. 1, pp. 137-151, 2000/04/01/ 2000.

- [37] K. H. Lyle, L. K. Tseng, J. P. Gore, and N. M. Laurendeau, "A study of pollutant emission characteristics of partially premixed turbulent jet flames," *Combustion and Flame*, vol. 116, no. 4, pp. 627-639, 1999/03/01/ 1999.
- [38] C. Prathap *et al.*, "Analysis of NOX Formation in an Axially Staged Combustion System at Elevated Pressure Conditions," *Journal of Engineering for Gas Turbines and Power*, vol. 134, no. 3, pp. 1-8, 2012.
- [39] M. Roa, W. G. Lamont, S. E. Meyer, P. Szedlacsek, and R. P. Lucht, "Emission Measurements and OH-PLIF of Reacting Hydrogen Jets in Vitiated Crossflow for Stationary Gas Turbines," in *Turbo Expo*, Copenhagen, Denmark, 2012, no. 44687, p. 68711, Volume 2: Combustion, Fuels and Emissions, Parts A and B: ASME.
- [40] D. Ahrens, M. Kolb, C. Hirsch, and T. Sattelmayer, "Influence of Preflame and Postflame Mixing on NOx Formation in a Reacting Premixed Jet in Hot Cross Flow," *Journal of Engineering for Gas Turbines and Power*, vol. 138, no. 8, pp. 1-10, 2016.
- [41] B. R. Wilde, "Dynamics of Variable Density Ratio Reacting Jets in Unsteady, Vitiated Crossflow," School of Aerospace Engineering, Georgia Institute of Technology, 2014.
- [42] Y. A. C. Cengel, John M., *Fluid Mechanics Fundamentals and Applications*. New York: McGrawHill, 2006.
- [43] R. T. M'Closkey, J. M. King, L. Cortelezzi, and A. R. Karagozian, "The actively controlled jet in crossflow," *Journal of Fluid Mechanics*, vol. 452, pp. 325-335, 2002.
- [44] S. Megerian, J. Davitian, L. S. De B. Alves, and A. R. Karagozian, "Transverse-jet shear-layer instabilities. Part 1. Experimental studies," *Journal of Fluid Mechanics*, vol. 593, pp. 93-129, 2007.
- [45] S. R. Shapiro, J. King, R. T. M'Closkey, and A. R. Karagozian, "Optimization of Controlled Jets in Crossflow," *AIAA Journal*, vol. 44, no. 6, pp. 1292-1298, 2006/06/01 2006.
- [46] J. Davitian, "Exploration and Controlled Excitation of Transverse Jet Shear Layer Instabilities," Aerospace Engineering, University of California, Los Angeles, 2008.
- [47] K. He, J. Sun, and X. Tang, "Guided image filtering," *IEEE transactions on pattern analysis and machine intelligence*, vol. 35, no. 6, pp. 1397-1409, 2013.
- [48] N. Otsu, "A threshold selection method from gray-level histograms," *IEEE transactions on systems, man, and cybernetics*, vol. 9, no. 1, pp. 62-66, 1979.

- [49] M. Pernpeintner, M. Lauer, C. Hirsch, and T. Sattelmayer, "A Method to Obtain Planar Mixture Fraction Statistics in Turbulent Flows Seeded With Tracer Particles," no. 54624, pp. 1341-1350, 2011.
- [50] J. C. Sautet and D. Stepowski, "Single-shot laser Mie scattering measurements of the scalar profiles in the near field of turbulent jets with variable densities," *Experiments in Fluids*, journal article vol. 16, no. 6, pp. 353-367, May 01 1994.
- [51] M. Raffel, C. Willert, S. Wereley, and J. Kompenhans, *Particle Image Velicometry: A Practical Guide*. New York: Springer, 2007.
- [52] B. J. McKeon *et al.*, "Velocity, Vorticity, and Mach Number: Particle Based Techniques," in *Handbook of Experimental Fluid Mechanics*, C. Tropea, A. Yarin, and J. F. Foss, Eds. Berlin: Springer, 2007.